Title

Understanding the Impact of Duchenne Muscular Dystrophy Disease Severity on Human Skeletal Muscle Progenitor Cell Delivery

Author

Saleh, Kholoud K.

Publication Date

2022

Peer reviewed|Thesis/dissertation

UNIVERSITY OF CALIFORNIA

Los Angeles

Understanding the Impact of Duchenne Muscular Dystrophy Disease Severity on Human Skeletal Muscle Progenitor Cell Delivery

A dissertation submitted in partial satisfaction

of the requirements for the degree Doctor of Philosophy

in Molecular, Cellular and Integrative Physiology

by

Kholoud Khedr Saleh

2022

ABSTRACT OF THE DISSERTATION

Understanding the Impact of Duchenne Muscular Dystrophy Disease Severity on Human Skeletal Muscle Progenitor Cell Delivery

by

Kholoud Khedr Saleh

Doctor of Philosophy in Molecular, Cellular and Integrative Physiology

University of California, Los Angeles, 2022

Professor April Dawn Pyle, Chair

Duchenne muscular dystrophy (DMD) is caused by an out-of-frame mutation in the DMD gene that results in the absence of a functional dystrophin protein, leading to a devastating progressive lethal muscle-wasting disease. Muscle stem cell-based therapy is a promising avenue for improving muscle regeneration. However, despite the efforts to deliver the optimal cell population to dystrophic muscles, little is understood on the role endothelial cells play during systemic delivery. Recent single cell RNA sequencing (scRNA-seq) advances has permitted the unraveling of cellular composition and phenotypes in multiple mouse tissues, including skeletal muscle. Here we describe the development of an optimized protocol for systemic delivery of skeletal muscle progenitor cells (SMPCs) which showed limited ability to escape the endothelial barrier in dystrophic and severely dystrophic muscle. To further understand the role of the microenvironment as a barrier to systemic cell delivery to skeletal muscle we explored skeletal

muscle-resident cell populations in healthy, dystrophic and severely dystrophic mouse models utilizing scRNA-seq. We found an increased frequency of activated fibroblasts, activated fibro-adipogenic progenitor cells and proinflammatory macrophages in dystrophic and severely dystrophic gastrocnemius muscles. Moreover, employing a computational intercellular interaction method, we show an upregulation of extracellular matrix and platelet aggregation genes on endothelial cells in dystrophic and severely dystrophic muscles. We further show an increased risk of clotting especially in the severely dystrophic environment. This work extends our understanding of the severe nature of DMD, which should be taken into account when considering stem cell-based systemic delivery platforms.

The dissertation of Kholoud Khedr Saleh is approved.

Melissa J. Spencer

Rachelle Hope Crosbie

M. Luisa Iruela-Arispe

April Dawn Pyle, Committee Chair

University of California, Los Angeles

2022

DEDICATION

To my daughters Tala and Elia, you brighten my day, every day.

To my husband who I leaned on for support.

To my mentors who inspire me to be a better scientist.

TABLE OF CONTENTS

LIST OF FIGURES

LIST OF TABLES

ACKNOWLEDGMENTS

I would like to thank all those who supported me throughout my journey to become a better researcher and scientist. First and foremost, I want to acknowledge and thank my graduate studies advisor Dr. April Pyle, who shined like the brightest star as a mentor to me. Her passion for science was contagious, not only did she teach me how to think creatively and diligently, but she also taught me how to love and be excited about my research. Dr. April Pyle provided me with constant advice and support but allowed enough space for independence; something hard to achieve except if you are April Pyle. I would like to thank her for her attentiveness and for truly caring, about my science, my personal development, and my family's well-being. I aspire to be as great of a mentor and scientist as she is, so I would like to thank her for setting the example. I would like to also extend my appreciation to my committee members Dr. Melissa J. Spencer, Dr. Rachelle Crosbie, and Dr. Luisa Iruela-Arispe for their indispensable advice and support throughout this journey. I am extremely fortunate to have had creative, dedicated, and knowledgeable strong women scientists as my committee members, they had shaped me profoundly and I am forever grateful to them.

Additionally, I would like to acknowledge the help and support provided by the Pyle laboratory members. I must start by thanking Courtney Young for being the best example and girl power inspiration to join the Pyle Laboratory. I would like to acknowledge Haibin Xi, whose expertise, patience, and mentorship in the lab was crucial for my growth as a scientist. I owe him a lot of my bench knowledge and discipline, but mostly I owe to him my understanding of bioinformatics analysis for scRNA sequencing data. Peggie Chien and Matthew A. Romero not only have given invaluable support, advice, and help with experiments, but they also kept my sanity in check when I needed it, and for that I am deeply thankful. I would like to especially thank my two undergraduate trainees: Corey Switzler and Emily Skuratovsky, not only for their contribution to the long hours of sectioning, imaging, and counting, but also for helping shape my skills as a mentor. I would like to acknowledge all the help and support provided by all the Pyle Laboratory members that I had the privilege to work with: Lily Gane, Devin

Gibbs and Anne Roe, and former members Michael Hicks, Shahab Younesi, Karen Gonzalez, and Katrina Paras. The long hours in the lab were enjoyable, fun, and impactful because of all of them. Although not directly influencing this work, I would like to extend my gratitude to my previous research mentors: Dr. Hamda Al-Naemi and Dr. Reza Ardehali, and my QNRF mentors: Dr. Aisha Al-Obaidly and Dr. Ayman Bassil, who have set me into scientific research path.

Outside of Academia, I would like to express my deepest gratitude and appreciation to my husband, Salama Altalla, and my two daughters Tala and Elia Altalla. I am grateful for their unconditional love, continuous support, and patience. I owe my small family keeping me grounded, focused, and desire to become a better scientist, researcher, wife, mother, and individual. Moreover, I am thankful to my parents, Khedr Saleh and Huda Abdulmajeed for their love, support, and encouragement to pursue my passion in science. Furthermore, I would like to extend my gratitude to my friends and second family: Lara Biden and Martha Rimniceanu for their support, love, and the amazing memories we have made together. To all my friends in Los Angeles: Zahra Kamil, Arunima Bera, Atheer Althobaiti, Afnan Althobaiti, and Reem Khoja; and to all my friends in Qatar: Faiha Alqahtani, Rand Elshorafa, Ruqiya Alhitmi and Amal Abdulmajeed, you kept me going and you inspired me. I am extremely grateful and lucky to have been surrounded by the greatest supportive people, and even luckier to call them my friends.

Chapter 2 is adapted from a version of a paper in preparation. *An Optimized Protocol for Intra-Arterial Cell Delivery Procedure Reveals the Impact of Disease Severity on Systemic Delivery*. Authors: Kholoud K. Saleh, Corey Switzler, Lily Gane and April D. Pyle. Author contributions are as follows: K.K.S and A.P designed the study and wrote manuscript. K.K.S performed IA surgeries with assistance from C.S. K.K.S and C.S collected and sectioned muscles, stained and imaged muscle cross-sections. C.S and L.G quantified the data. A.P provided guidance and feedback on data.

Chapter 3 is adapted from a paper in revision in *iScience*. *Single Cell Sequencing Maps Cellular Diversity in Increasing Disease Severity in Dystrophic Mouse Models*. Authors: Kholoud K. Saleh, Haibin Xi, Corey Switzler, Emily Skuratovsky, Matthew A. Romero, Peggie Chien, Devin Gibbs, Lily Gane, Michael Hicks, Melissa J. Spencer and April D. Pyle**.** Author contributions are as follows: K.K.S and A.P designed the study and wrote the manuscript. K.K.S performed muscle digestions for scRNA-seq studies with assistance from C.S, P.C, and D.G. H.X and K.K.S performed the scRNA-seq study bioinformatics analysis. K.K.S, C.S, E.S and L.G performed staining, imaging, and quantification. K.K.S and E.S performed western blots with supervision and assistance from M.R. M.H contributed to generation of the different mouse models and mouse colony management. M.S provided mdxDBA2 mice and provided feedback on the data and paper.

Chapter 4 is partly adapted from a version of a paper in preparation. *Nanoparticles Systemically Bio-distribute and Release Payload at the Site of Regenerating Myofibers in Dystrophic Skeletal Muscle*. Authors: Michael R. Hicks, Xiangsheng Liu, Kholoud K. Saleh, Courtney S. Young, Ying Ji, Jinhong Jiang, Michael Emami, Ekaterina Mokanova, Melissa J. Spencer, Huan Meng, and April D. Pyle. Author contributions are as follows: M.R.H, H.M and A.D.P designed the study. M.R.H wrote the manuscript. X.L, Y.J and J.J formulated the MSNPs. M.R.H, X.L, K.K.S and C.S.Y performed *in vivo* studies, muscle collections, and IF staining. E.M performed WB analysis. K.K.S performed IA cell delivery with assistance from M.R.H. M.J.S, X.L, H.M and A.D.P reviewed and edited manuscript.

VITA

EDUCATION

2010-2014	Bachelor's Degree in Science, Biological Sciences; Qatar University, Qatar
2007-2010	Pre-Medical Program; Weill Cornell Medical College, Qatar

RESEARCH EXPERIENCE

April 2017-Present	Graduate Student Researcher (Advanced to Candidacy Dec. 2018); UCLA, USA (PI: Dr. April Dr. Pyle)
Nov. 2014-Dec. 2016	Visiting Scholar Researcher; UCLA, USA (PI: Dr. Reza Ardehali)
2013-2014	Undergraduate Research Assistant; Qatar University, Qatar (PI: Dr. Hamda Al-Naemi)
Summer 2013	Undergraduate Researcher; Cambridge University, England (PI: Dr. Mark Kotter)

FELLOWSHIPS & AWARDS

2020	Biomedical, Life Sciences and Health Sciences Research Award- UCLA David Geffen School of Medicine
2016-2022	Qatar Research Leadership Program (QRLP)- Qatar National Research Fund (QNRF) *Graduate Research Scholar Track*
2014-2016	Qatar Research Leadership Program (QRLP) *Management Track*- Qatar Foundation
2013-2014	Qatar Science Leadership Program *Undergraduate Track*- Qatar Foundation
2007	Education Excellence Day award; for outstanding achievement high school graduate. Awarded by his Highness Sheikh Tamim bin Hamad Al Thani, Emir of the State of Qatar and Chairman of the Supreme Education Council

PUBLICATIONS

Saleh K.K., Switzler C., Gane L., Pyle A.D. (2022) Development of Optimized Intra-arterial Cell Delivery Approach. *In preparation*

Saleh K.K., Xi H., Switzler C., Skuratovsky E., Romero M.A., Chien P., Gibbs D., Gane L., Hicks M.R., Spencer M.J., Pyle A.D. (2022) Single Cell Sequencing Map of Cellular Diversity as Disease Severity Increases in Dystrophic Mouse Models. iScience. *Under Review*

Hicks M.R., **Saleh K.K.**, Gibbs D., Yang M., Younesi S., Gane L., Guiterez V., Xi H., Pyle A.D. (2022) In Vivo Satellite Cell Niche Emergence from Human Pluripotent Stem Cells. Nature Cell Biology. *In Revision*

Skelton R.J., Brady B., Khoja S., Sahoo D., Engel J., Arasaratnam D., **Saleh K.K.**, Abilez OJ, Zhao P., Stanley E.G., Elefanty A.G., Kwon M., Elliott D.A., Ardehali R. (2016) CD13 and ROR2 Permit Isolation of Highly Enriched Cardiac Mesoderm from Differentiating Human Embryonic Stem Cells. Stem Cell Reports. DOI: 10.1016/J.Stemcr.2015.11.006

MENTORSHIP AND TEACHING

2018-2020	**Mentorship** Undergraduate Research Assistant Corey Switzler (Microbiology, Immunology and Molecular Genetics) Current Position: Research Assistant at Salk Institute for Biological Studies (USA, CA, San Diego)
2021-2022	**Mentorship** Undergraduate CIRM Bridges Fellow Emily Skuratovsky (California State University-Northridge, majoring in Cell and Molecular Biology)
April 2018-June 2018 April 2019-June 2019	**Teaching** UCLA Teaching Assistantship for LIFESCI 7C (Physiology and Human Biology)

SELECTED ORAL PRESENTATIONS

Saleh K. K. "The Severity of Muscular Dystrophy Impacts the Effectiveness of Human Skeletal Muscle Progenitor Cell Delivery to Muscles". Musculoskeletal Seminar Series. UCLA, Los Angeles. March 30th 2022

Saleh K. K. "The Severity of Muscular Dystrophy Impacts the Effectiveness of Human Skeletal Muscle Progenitor Cell Delivery to Muscles". Molecular, Cellular and Integrative Physiology Retreat. UCLA, Los Angeles. March 16th 2022

Saleh K. K. "Investigating migratory potential of skeletal muscle progenitor cells derived from human pluripotent stem cells". Working group of the Center for Duchenne Muscular Dystrophy. UCLA, Los Angeles. May 10th 2018

Saleh K. K. "Development of an *in vivo* systemic delivery strategy of CRISPR corrected iPSC-SMPC for DMD". Qatar Research Leadership Program Annual Gathering. Qatar Dec. 20th 2017

SELECTED POSTER PRESENTATIONS

Saleh K., Switzler C., Hicks M., Yang M., Pyle A. (2020, February). Investigating Extravasation Potential of Skeletal Muscle Progenitor Cells in DMD Mouse Models. Center for Duchenne Muscular Dystrophy Annual Retreat. UCLA, Los Angeles. February 18th 2020

Saleh K., Hicks M., Emami M., Young C., Liu X., Meng H., Spencer M., Pyle A. Development of Improved Systemic Delivery Approaches for Human Skeletal Muscle Progenitor Cells to Dystrophic Muscle. Molecular, Cellular and Integrative Physiology Interdepartmental PhD program Annual Retreat. Calamigos Ranch, Malibu. February 9th 2019

Saleh K., Hicks M., Emami M., Young C., Liu X., Meng H., Spencer M., Pyle A. (2018, June). Identification of Candidates Modulating Human Skeletal Muscle Progenitor Cell Migration. International Society for Stem Cell Research (ISSCR) Annual Meeting 2018. Melbourne, Australia. June 20th-23rd 2018

CHAPTER 1: Introduction

1.1 Skeletal muscle and muscle stem cells

Skeletal muscle is one of the most dynamic and regenerative tissues in the body that plays a vital role in movement and postural support. It constitutes about 40-45% of the human body and is composed multinucleated muscle fibers. The multinucleation of muscle fibers arises from the fusion of myoblasts. Muscle fibers are aligned in parallel to form muscle bundles, known as fasciculus, encompassed by extracellular matrix, which in turn bundle and align parallelly to form muscle tissue. The muscle tissue has a heterogeneous cellular makeup with multiple cell populations contributing to its architecture including endothelial cells, vascular smooth muscle cells, innervating neurons, stromal cells, fibro-adipogenic progenitor (FAP) cells, macrophages, and muscle stem cells (Figure 1-1). The remarkable ability of muscle tissue to regenerate is a well-orchestrated process with multiple cell types participating in the regenerative cascade, including the contribution of FAPs that proliferate upon muscle injury and send signals to muscle stem cells to activate, proliferate and differentiate[1]. Muscle stem cells, also called satellite cells (SCs), are uniquely situated in a niche between the basal lamina and the sarcolemma of muscle fibers and are considered quiescent, not mitotically active, marked by PAX7 expression[2–5]. Upon injury SCs activate, divide, and turn on MYF5 and MYOD, indicating their commitment to a myoblast fate[5–9]. A fraction of SCs divide

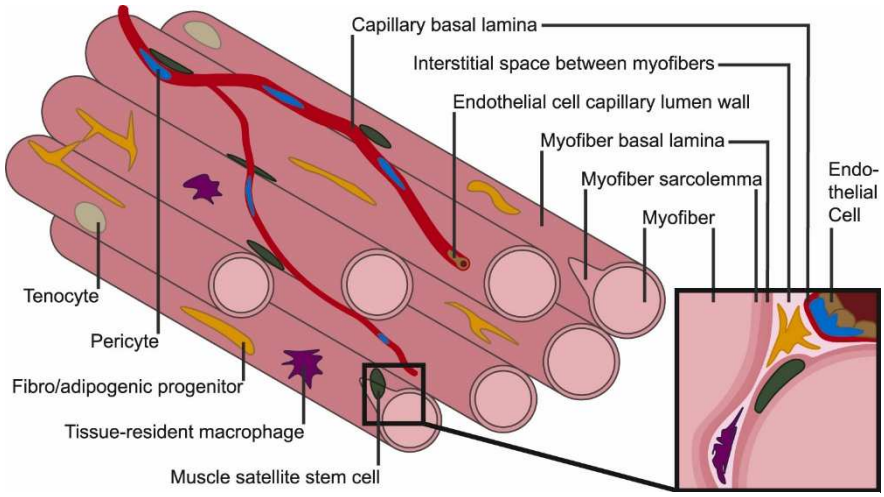

Adapted from [197]

Figure 1-1: Architecture of muscle tissue with heterogeneous cellular makeup. Skeletal muscle tissue contains different cell types including skeletal muscle fibers, tenocytes, endothelial cells, muscle stem cells and fibro-adipogenic progenitors.

asymmetrically during the regeneration process to self-renew and return to the quiescent state[9–13]. The transplantation of a single SC has been shown to produce copies of itself and generate more specialized progenitors, the gold-standard test for stem cell potential and self-renewal[14].

1.2 Single Cell RNA Sequencing to untangle cellular composition of skeletal muscle

RNA sequencing (RNA-seq) utilizes the use of next generation sequencing (NGS) to examine the quantity and average expression of genes in a biological sample. This technique has widened our understanding of the transcriptome of the total cellular content, which translates to protein expression. Allowing the gain of transcriptome dynamics and changes in different tissues and in different states such as in normal and diseased conditions. However, though a powerful tool, bulk RNA-sequencing does not depict the cellular gene expression diversity within the analyzed tissues. From there, new powerful technologies for investigating the gene expression profile at a single-cell level (scRNA-seq) has emerged. Since the first study of scRNA-seq has been published, multiple other scRNA-seq techniques has evolved including the Chromium single cell gene expression[15–19].

The Chromium single cell gene expression employs the use of microfluidic partitioning to isolate single cells into droplets that contain barcoded oligonucleotides along with reverse transcription reagents and oil. In each droplet, also called a Gel Bead in Emulsion (GEM), the single cell is lysed, the Gel Bead is dissolved, freeing the barcoded oligonucleotide reverse transcription reagents in the solution. The

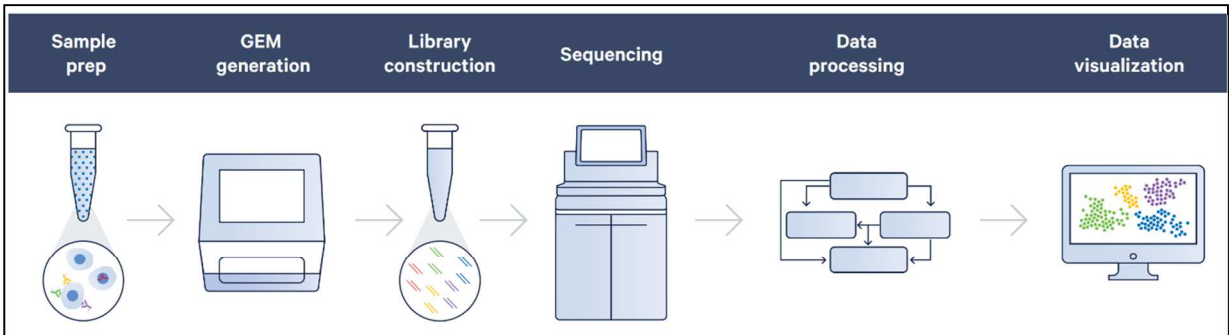

Figure 1-2: 10X Genomics Chromium single cell gene expression workflow. Single cell suspension is used to generate GEMs, which are used to prepare libraries with multiple readouts that can be traced back to the same single cell for sequencing. Sequencing is then carried out and data are processed with analysis tools such as Cell Ranger and Seurat. The sample can then be visualized.

reverse transcription of the polyadenylated mRNA then occurs. Thereafter, all cDNA from a single cell will have the same barcode, allowing to trace back the sequencing reads to their single cell of origin. The NGS is then carried followed by sequencing, and then the data are processed and analyzed.

The first study that laid the groundwork for the use of scRNA-seq technology to understand muscle-resident cell population heterogeneity, with a focus on SCs, was published in 2017[20]. Although only 21 SCs were analyzed, it was able to capture the SC transcriptomic heterogeneity within the uninjured mouse muscle. The characterization of cellular diversity of mouse skeletal muscle was then described by the release of the tabula Muris Consortium[21]. The group has described the main muscle-resident cell types including endothelial cells, mesenchymal cells, satellite cells along with immune cells such as B cells, T cells and macrophages. A more complete analysis of the healthy muscle identified ten muscle-resident cell types, which in addition to previously described was able to identify FAPs, neutrophils, glial cells, tenocytes (Scx^+ cells) and smooth muscle-mesenchymal cells ($lin^-VCAM^-ITGA7^+$)[22]. To further understand the cellular dynamics of regenerating muscle after acute injury, which as previously described is mainly achieved by the SCs and orchestrated by other muscle-resident cell populations, other groups has utilized scRNA-seq to generate an atlas of the regenerating skeletal muscle[23–25]. These studies collectively described a comprehensive scRNA-seq datasets where heterogenous muscle-resident populations arise, such as activated fibroblasts and committed SCs, during muscle regeneration. These studies provided insights into the complexity and diversity of muscle-resident cell populations in both healthy and regenerating muscle and further illustrated how the power of scRNA-seq technology can be harnessed to identify previously understudied populations. Limited studies have used scRNA-seq to study the muscle in pathological conditions, for instance in inflammatory muscle diseases such as Duchenne muscular dystrophy (DMD)[26]. In this dissertation the use of chromium single cell 3' expression profiling has been utilized to explore muscle cellular composition and to examine transcriptional changes within each muscle-resident cell population in healthy, wt-NSG, dystrophic, mdx-NSG, and severely dystrophic, mdxD2-NSG, mouse models (described in later section).

1.3 Duchenne muscular dystrophy and muscle stem cells

Duchenne muscular dystrophy (DMD) is an X-linked recessive, severe progressive muscle wasting disease affecting ~1-5000 male live births[27–29]. Both devastating and fatal, DMD patients are diagnosed typically before their fifth year of age, are wheelchair bound in their teens, and prematurely die in their mid-twenties. DMD is caused by a loss-of-function mutation in the *DMD* gene, the largest known gene in the human genome, that results in the absence of a functional dystrophin protein[30]. Dystrophin acts as a linker protein which connects the cytoskeleton of the muscle fiber to the extracellular matrix through the dystrophin glycoprotein complex (DGC)[31–35]. Dystrophin, moreover, helps anchors the DGC to the muscle sarcolemma. Without dystrophin, the DGC is mislocalized resulting in fragility and disruption of the sarcolemma. The muscle fibers go through progressive rounds of contraction-induced damage, and Ca^{2+} influx into the muscle fiber which results in cell death. In DMD, continuous cycles of contraction-induced damage elicit a constant need for regeneration that is mainly achieved by SCs. However, it has been suggested that there is impaired regeneration because either the SCs are rendered dysfunctional due to impaired polarity establishment or because of progressive exhaustion[36–38]. Eventually, lack of proper regeneration leads to muscle fiber necrosis and generation of excess fibrotic tissue[39].

Treatments for DMD are available to help manage symptoms and improve the quality of life of patients, such as the use of Corticosteroids (Prednisone or Deflazacort) to maintain muscle strength, and Morpholino antisense oligomer (Eteplirsen, Golodirsen, or Casimersen) to increase dystrophin production[40]. Currently, no cure exists for DMD, albeit multiple ongoing genetic interventions are in clinical trials including adeno-associated virus serotype 9 (AAV9) capsid delivery of microdystrophin- and minidystrophin-encoding genes to muscle tissues for targeted production of shortened versions of dystrophin (NCT03368742, NCT03362502, NCT03769116).

1.4 Mouse Models of Duchenne Muscular Dystrophy

The most common mouse model used to study DMD is the mdx mouse, which has a nonsense mutation in exon 23 in the X chromosome that arose spontaneously in a C57BL/10 colony [41,42]. Although this mouse model lacks dystrophin protein, mdx mice have elevated plasma levels of muscle creatine kinase (CK), and present histological muscle lesions like that of human disease, although adult mdx mice do not fully recapitulate the human disease in terms of pathogenic progression. The mdx mouse model lifespan is not significantly reduced, and regeneration of muscle fibers is not persistent. Mdx mice also lack extensive fibro-fatty replacement of muscle fibers thus the mdx model does not fully recapitulate human clinical disease progression[43–45].

Since the discovery of the mdx mouse, several other DMD-mouse models have been generated in different genetic backgrounds. One of which is the DBA/2-mdx (hereafter referred to as mdxD2) mouse strain. MdxD2 mice exhibit lower muscle weight, fewer muscle fibers and increased fibro-fatty deposition in comparison with the mdx strain[46]. Genetic modifiers on the DBA/2 genetic background, include osteopontin (Spp1), a synonymous variant in Annexin A6 (Anxa6) exon 1, and polymorphisms in the coding region of the latent TGF-β-binding protein 4 gene (Ltbp4), which generates a more severe muscular dystrophy [47–49] . Disease is exacerbated due to enhanced TGF-β signaling. Muscles of the mdxD2 model show increased inflammation, increased fibrosis and progressive weakness and atrophy, which better recapitulate the characteristics of human DMD [50–52].

In this work, the mdx SCID mouse model was crossed with the severely immunocompromised mouse model NSG to generate mdx-NSG model. Moreover, the mdxD2 mouse was crossed with NSG to generate mdxD2-NSG mouse model. Mutations in the NSG mouse model renders B cells, T cells and natural killer cells deficient. These DMD severely immunocompromised mouse models are ideal for stem cell engraftment studies and cell delivery assessment as they permit evaluation of stem cell engraftment without the potential for immune-rejection of human cells.

1.5 Cell-based therapies for Duchenne Muscular Dystrophy

Since the early 1990s cell-based therapies were proposed for DMD by transplantation of myoblasts, an activated mononucleated cell that arises from SCs and can differentiate and fuse to form multinucleated muscle fibers. The enthusiasm of restoring dystrophin in the mdx mouse model by intra-muscular (IM) myoblast transplantation, resulted in 4 clinical trials in humans, that ultimately all failed to restore sufficient dystrophin to provide functional benefit [53–59]. It is now the consensus that to have an effective long-term cell-based therapy, a transplanted cell needs to maintain its ability to self-renew, contribute to the regeneration of degenerating muscle, and reside in a niche. One of the main challenges that faced the myoblast transplantation is the lack of self-renewal ability of transplanted cells. Because of their regenerative capacity, the field has since focused on transplanting either skeletal muscle progenitor cells (SMPCs) or SCs [14,60–65]. SMPCs arise prenatally during myogenesis and express the myogenic transcription factor PAX7, SCs on the other hand contribute to muscle homeostasis and regeneration postnatally [66,67]. Though both SMPCs and SCs can contribute to muscle regeneration when transplanted intramuscularly in injured muscle, SCs are superior to SMPCs in repopulation of the stem cell niche and supporting long-term engraftment [61,68].

In mouse models, the transplantation of SCs from single intact muscle fiber, into an irradiation treated muscle, resulted in the transplanted SCs to return to quiescence and contribute to repopulation of muscle fibers [69]. Isolation of SCs from mouse skeletal muscles using cell surface markers, integrin-α7 and CD34 (and lineage depletion), utilizing fluorescence activated cell sorting (FACS) allowed the transplantation of a single SC into irradiated muscle which was capable of self-renewing itself by production of multiple copies of itself and generating muscle progenitors[14]. Moreover, skeletal muscle precursors, isolated by CXCR4 and □1-integrin expression, were able to regenerate, re-engraft the SC niche and improve contractile force of mdx muscle, previously cardiotoxin injured[70].

Therefore, SCs can be considered as a therapeutic target for restoring muscle function in DMD patients. The transplantation of human fetal SMPCs into cryodamaged mouse muscle resulted in the

generation of low number of human SCs on the isolated muscle fibers, which when transplanted into a second host mouse could form a human muscle fiber[65]. Additionally, the transplantation of human postnatal muscle myoblasts, isolated from healthy 13-month old muscle biopsies, has been shown to engraft and generate SCs residing in the periphery of muscle fibers and inside the basal lamina in irradiated mouse muscle[71]. It was not until recently that surface markers isolating adult human SCs and fetal SMPCs have been described. Adult human SCs were isolated from muscle tissue using the cell surface markers CD29 and CD56 and shown to achieve efficient engraftment and self-renewal ability after transplantation in irradiated mouse muscle[63]. Another group provided evidence that MCAM and CD82 mark human fetal SMPCs, while NCAM and CD82 mark adult SCs, which were shown to engraft and restore dystrophin in immune-deficient mouse model of DMD[72]. Despite the progress of human SMPCS and SCs engraftment in mouse models, the greatest challenge faced for human SCs to be used for meaningful therapeutic benefit is their inability to maintain their stemness *in vitro* when expanded. Moreover, transplanted SCs are typically only detected at or near the site of injection, suggesting their inability to migrate to multiple muscles.

1.6 Pluripotent stem cell derived skeletal muscle progenitor cells for DMD

Human pluripotent stem cells (hPSCs) provide a great tool for understanding human myogenesis, disease modeling, and generation of cells for cell-based therapies. hPSCs can self-renew indefinitely and be differentiated to any cell type in the body including the endoderm, ectoderm, and mesoderm germ layers. They could be derived from either the inner cell mass of a blastocyst, called human embryonic stem cells (hESCs), or by reprogramming somatic cells back into a pluripotent state, called human induced pluripotent stem cells (hiPSCs), using the Yamanaka transcription factors[73]. As such hPSCs provide a valuable tool for developing disease models in a dish and potentially cell-based therapies for DMD. For example, skin biopsies can be obtained from patients, fibroblasts reprogrammed to hiPSCs, then gene-corrected hiPSCs can be differentiated to SMPCs or SCs, and finally transplanted back into patients (Figure 1-1). However, up to date, myogenic differentiation protocols of hPSCs does not result in

the formation of SCs *in vitro.* Rather, the differentiation of hPSCs give rise to SMPCs (hPSC-SMPCs) at an embryonic- to -fetal transitional developmental stage and have a different transcriptional signature than that of postnatal SCs[74].

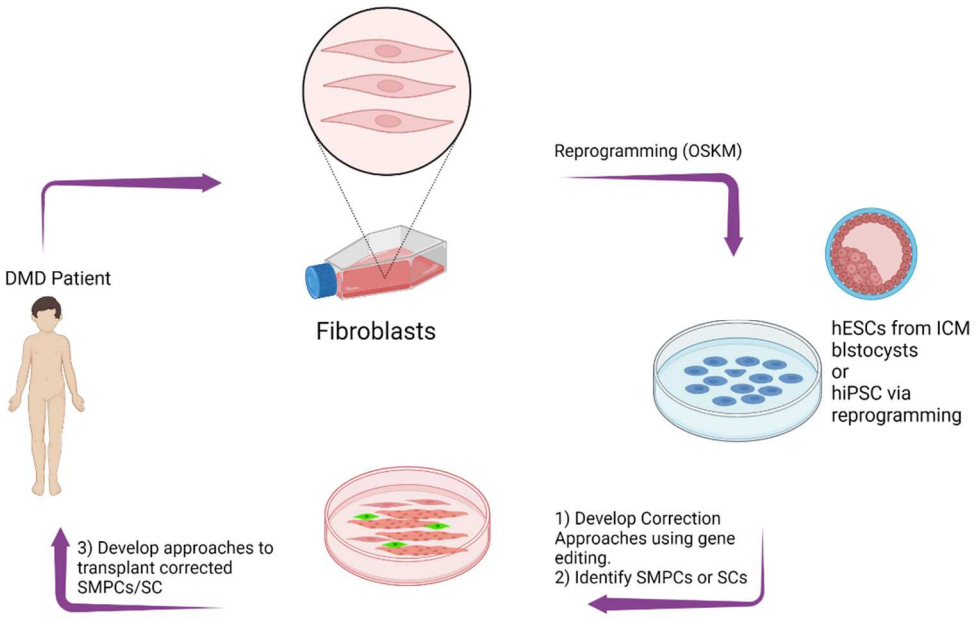

Figure 1-3: Schematic of workflow for developing cell-based therapies from hPSC Fibroblasts obtained from skin biopsies from DMD patients can be reprogrammed to hiPSCs, these cells can then be used to understand the pathology of the disease, develop correction approaches, and be differentiated into SMPCs or SCs for the ultimate goal to be transplanted back into the patient to restore dystrophin and provide functional benefit.

In 2007 the first use of hESCs to derive skeletal muscle progenitors was achieved by inducing hESCs to differentiate to mesenchymal precursors and further isolating CD73 and NCAM progenitor cells[75]. These hESC-derived skeletal progenitors generated myotubes *in vitro* and survived long-term in immunocompromised, SCID/Beige, mouse muscle. Following this first use of hESCs to generate skeletal muscle, others have used overexpression to produce a more homogeneous myogenic culture. For example, by the overexpression of MYOD, a master myogenic regulator, using adenovirus infection of differentiated hESCs and hiPSC from a DMD patient, pure myogenic progenitors were obtained and transplanted into a Rag/mdx mouse muscle. These MYOD-hESCs and MYOD-hiPSCs progenitors were

shown to regenerate the muscle and restore dystrophin[76]. Additionally, with viral overexpression of PAX7 (called iPAX7), the feasibility of generating SMPCs derived from hESCs and hiPSCs was demonstrated[77]. When transplanted into injured dystrophic mouse muscle, NSG-mdx^{4Cv}, iPAX7 hESC- and hiPSCs-derived myogenic progenitors were able to regenerate the muscle, provide functional improvement and restore dystrophin. Though promising, the previous studies relied on viral overexpression of myogenic markers which could be challenging to translate to the clinic and may not represent a true cell found in normal human development.

A major hurdle that is facing the stem cell-based therapy field is that the differentiation protocols of hPSCs to myogenic progenitors result in SMPCs (hPSC-SMPCs) at an embryonic- to -fetal transitional developmental stage and have a different transcriptional signature than that of postnatal SCs[74]. Currently, there are no directed differentiation protocols that result in the generation of SCs in culture, and it is still unknown how to mature SMPCs into SCs. However, in recent years, great advancement has been achieved in the directed differentiation of hPSCs to SMPCs without the need for viral overexpression of myogenic transcription factors[78–82]. The purification of SMPCs derived from directed differentiation of hPSC is a crucial step towards identifying the pristine engraftable cell that is capable of residing in the niche and regenerating muscle after injury. Recently, different surface markers have been described for the isolation of hPSC-SMPCs. hPSC-SMPC enriched for ERBB3 and NGFR have been shown to engraft robustly in mdx-NSG injured muscle, and equivalently to fetal SMPCs[64]. Other markers that have been used for the purification of hPSC-SMPCs are CD54, α9□1 and SDC2; and CD10 with the depletion of CD24[83,84]. All the previous hPSC-SMPCs enrichment strategies resulted in dystrophin restoration when engrafted into injured DMD mouse muscle. However, although engrafted hPSC-SMPCs contribute to the regeneration of the injured DMD muscle, SMPCs reside in the SC niche inefficiently (data not shown and Gabsang Lee Cell stem cell recent paepr). Moreover, most of these studies has focused on intramuscular (IM) transplantation of SMPCs which result in a local engraftment of the cells and will not be able to

restore dystrophin to all effected muscles). Furthermore, the effect of the dystrophic microenvironment on transplanted cells is not understood.

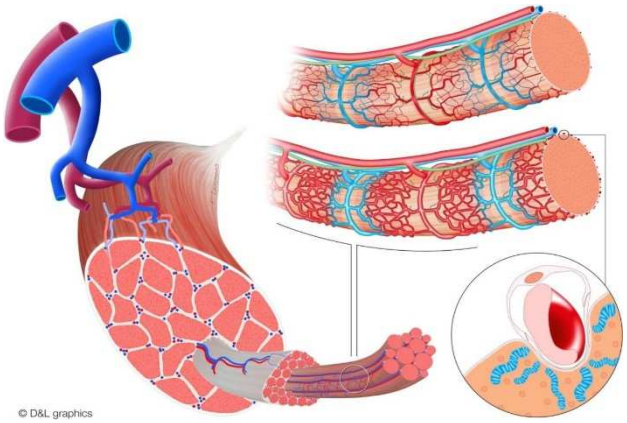

Figure 1-4: Schematic representation of muscle vasculature. Arterioles branch off from primary arteries down to terminal arteries. These then branch off to capillaries which in turn connect to postcapillary venules, venules and eventually join into a vein. Bottom right is magnification of a capillary embedded into the muscle. Adapted from [198].

1.7 Vasculature of the skeletal muscle and endothelial cells

To meet the metabolic demand required for muscle contraction, skeletal muscle is highly vascularized. Arteries which branch to arterioles, smaller-diameter blood vessels, feed the muscle tissue with blood traveling from the heart. The arterioles branch further to terminal arterioles, which in turn branch to an even smaller blood vessel unit called capillaries. Capillaries are the smallest blood vessels and the site where oxygen and nutrient exchange occurs. The capillary network then carries blood into postcapillary venules, then into venules which eventually join into veins (Figure 1-2). Skeletal muscle vasculature does not supply nutrients and oxygen only, but also plays a critical role in skeletal muscle regeneration[85]. SCs have been found to be closely associated with capillaries in adult skeletal muscle and help maintain their quiescence[86,87].

Endothelial cells (ECs) form a monolayer that lines the interior of blood vessels creating a barrier between circulating blood and tissues. ECs play key roles in vascular relaxation and constriction and extravasation of solutes and fluid, as well as regulation of leukocyte activation and extravasation, and platelet adhesion and aggregation [88]. ECs respond to environmental cues and can release different growth factors such vascular endothelial growth factor (VEGF) and insulin growth factor (IGF)-1 which are known to be mitogenic, providing evidence that they are crucial during myogenesis and regeneration[86,89]. Recent scRNA-seq studies revealed that ECs are incredibly heterogenous in healthy muscle with arterial,

venous, and capillary ECs having unique transcriptional profiles[90–92]. In DMD patients, ECs have been shown to be impaired, with evidence of vascular injury[93,94]. Moreover, the basal lamina of DMD muscle capillaries have been shown to have a thicker basal lamina, and a lumen that is larger than normal[95]. In the mdx mouse model, it has been reported that the vascular changes are age-dependent, with impaired angiogenesis, migration, and proliferation of ECs in *vitro* and *in vivo* in older mdx mice [96–98].

1.8 Systemic delivery of muscle progenitor cells for cell-based therapies

The route of delivery of SCs or SMPCs is a major hurdle for developing cell-based therapies for DMD. Previous reported studies have used primarily IM injections of myogenic cells which results in local cell engraftment at the injection site. Systemic delivery is advantageous since the cells can reach multiple muscles. While SCs were mainly used in direct IM transplantation studies, others have directed their efforts to find alternative sources of progenitor cells with myogenic capacity that can be used for systemic cell-based therapies. Human skeletal muscle-derived CD133 cells have been shown to have myogenic potential, regenerating the muscle and engrafting into the SC niche when transplanted in immunodeficient mouse muscle previously injured[99,100]. Moreover, the intramuscular and intra-arterial (IA) delivery of genetically corrected CD133 progenitors isolated from the blood and muscle of DMD patients resulted in recovery of muscle morphology, function, and dystrophin expression in *scid/mdx* mice[101]. Mesoangioblasts, blood vessel associated progenitor cells, were first described in the early 2000s and were also shown to have myogenic potential[102,103]. Mesoangioblasts were identified and characterized from mouse, dog, and human tissues[104]. They were transplanted through IM injection and systemically through IA route into sarcoglycan null mouse model confirming dystrophin restoration[105,106]. This lead to their delivery in a large animal model; the golden retriever dogs muscular dystrophy model, which resulted in recovery of dystrophin, normal muscle function and amelioration of dystrophy[107]. Showing promising results in pre-clinical settings, both muscle-derived CD133 progenitors and mesoangioblasts were moved to human patient studies, but have not been shown to be effective at

restoring dystrophin when delivered to DMD patients, although CD133 treated patients had an increased ratio of capillaries per muscle fiber [108,109].

hPSCs derived myogenic progenitors have been also suggested to home to skeletal muscle after their systemic delivery. For instance, iPAX7 cells delivered IA to immunodeficient mouse model of DMD was shown to restore dystrophin after 4 weeks of engraftment[110]. Genetically corrected hiPSCs derived mesoangioblasts were also shown to engraft and form muscle fibers when delivered to immunodeficient sgca-null mice, a model of limb girdle muscular dystrophy 2D[111,112]. This provides a proof-of-principal that hiPSCs can indeed be used for systemic cell-based therapies, however, the efficiency of cells homing to the dystrophic muscle is too low.

1.9 Nanoparticles for growth factor delivery to DMD muscle

Nanoparticles could be synthesized from polymer-based, lipid-based, nonpolymeric or nanocrystalline materials at a nano-scale[113]. Nanoparticles have been utilized in medicine to deliver small-molecules and drugs to targeted sites, especially in cancer biology, and several nanoparticle drugs have been approved and authorized for use by the United States food and drug administration[113,114]. Efforts for the delivery of nanoparticles for an efficient drug delivery for DMD, for exon skipping drugs for instance, have been demonstrated[115–117]. Although these studies show promising drug delivery to the mdx skeletal muscle as a proof-of-concept, the efficiency of delivery is still to be optimized for a functional benefit after systemic delivery for DMD.

Chemoattractant, such as stromal cell derived factor-1 (SDF-1), have been previously shown to be overexpressed in the dystrophic muscle, enhancing the homing of muscle progenitor cell delivery after IA transplantation[118]. The use of nanoparticles for the delivery of growth factors to dystrophic muscle to facilitate the homing of human SMPCs has not been shown to date. Therefore, nanoparticle biodistribution to multiple skeletal muscle in DMD mouse model, delivering growth factors, to enhance

human SMPCs homing after their systemic delivery offers a potential source of stem-cell based therapeutics.

1.10 Significance

DMD is a devastating disorder with limited treatment options. Stem-cell based therapeutics can offer a relevant promising and potentially lifelong cure for patients with DMD. However, a considerable challenge for the use of stem-cell based therapies for DMD is 1) lack of efficient targeting of multiple muscles, and 2) lack of understanding of the potential of DMD muscle to allow for stem-cell based systemic delivery.

The aim of this research was to develop an enhanced method for systemic delivery of human SMPCs to multiple muscles of DMD mouse models. We optimized an IA delivery approach to enhance human SMPCs delivery to multiple muscles. However, we found cells to be entrapped inside the blood vessels after their systemic delivery in dystrophic and severely dystrophic muscles. We, thereafter, utilized nanoparticles to package and deliver growth factors to dystrophic muscles to enhance the homing of human SMPCs, which ultimately were found to be efficient in delivering growth factors but did not enhance human SMPCs homing to muscle. We directed our efforts to explore and understand DMD muscle microenvironment employing scRNA-seq, especially in the context of the severity of DMD mouse models, and its potential impact on systemically delivered cells. This work is essential because it offers the groundwork for understanding the DMD muscle microenvironment as disease severity increases for potential stem-cell based therapeutics for DMD.

CHAPTER 2: An Optimized Protocol for Intra-Arterial Cell Delivery Procedure Reveals the Impact of Disease Severity on Systemic Delivery

Introduction

Duchenne muscular dystrophy (DMD) is caused by out-of-frame mutations in the *DMD* gene that result in the absence of a functional dystrophin protein, leading to a devastating progressive lethal muscle wasting disease [30]. Without dystrophin, muscle fibers go through continuous contraction-induced damage, causing repeating cycles of degeneration and regeneration. The regenerative capacity of skeletal muscle is mainly achieved through the differentiation of satellite cells (SCs) [119–121], a muscle stem cell population present between the basal lamina and sarcolemma of the muscle fibers [3]. In DMD, SCs become dysfunctional or exhaust due to continuous muscle damage, causing impaired muscle repair, and ultimately replacement by fat and fibrosis [122–125].

Human pluripotent stem cells (hPSCs) hold great promise in modeling diseases and generating cells and tissues for regenerative medicine. We and others have reported the generation of human skeletal muscle progenitor cells (SMPCs) derived from hPSCs [78,79,81]. hPSC-SMPCs generated *in vitro* have a similar developmental trajectory to embryonic-fetal SMPCs [74]. The current delivery strategy of SMPCs requires the direct injection of the cells into individual muscles, which is inefficient for clinical use since the intramuscularly injected cells lack migratory potential to other muscles [64,77]. Therefore, a more clinically relevant approach would be systemic delivery of SMPCs, to restore dystrophin across multiple muscles. Others have reported the delivery of different cell types systemically to DMD muscle including mesoangioblasts, DLL4 and PDGF-BB treated satellite cells, skeletal muscle-derived CD133+ cells, and induced *Pax3* embryonic stem cell derived cells among others [107,126–131]. Some of the studies report dystrophin restoration after systemic delivery in animal models, but when taken to the clinic, such as in case of mesoangioblasts or muscle-derived CD133+ enriched cells, the cells were not effective at restoring dystrophin when delivered to DMD patients [108,109].

An overlooked parameter in developing systemic cell therapeutics is the context of disease severity and the diseased microenvironment. Genetic modifiers that regulate disease severity in the mdx mouse model is affected by the genetic background. Once the mdx mouse model is crossed to the DBA/2 genetic background, creating the mdxD2 strain, the mice exhibit increased fat and fibrosis deposition, muscle weakness, reduced skeletal muscle function, and fewer central myonuclei indicating the increased severity of dystrophy phenotype [46,132]. Thus, the mdxD2 mouse model better recapitulates the human disease and is useful in evaluating therapies for DMD.

Here we describe a detailed protocol to deliver human SMPCs from fetal week 18 muscles to multiple hindlimb muscles in immunocompromised healthy, wt-NSG, dystrophic, mdx-NSG, and severely dystrophic, mdxD2-NSG, mouse models using intra-arterial (IA) delivery. This protocol has been optimized from other published protocols in two ways, restoring blood flow into the artery after cell injection, and delivering the cells using a pump to maintain constant flow rate during cell delivery[110,133]. We further investigated the detection and localization of SMPCs by quantifying the cells in at least 16 cross-sections taken across the length of the gastrocnemius muscles. We found overall that systemic delivery of SMPCs was inefficient in all models. However, significantly less human SMPCs were detected in wt-NSG gastrocnemius muscle cross-sections, compared to both mdx-NSG and mdxD2-NSG. Human SMPCs were found to be detected inside blood vessels distinctly in healthy, dystrophic and severely dystrophic muscles, with prominent clotting identified in mdxD2-NSG after IA systemic cell delivery. We propose that muscle microenvironment and the severity of muscular dystrophy to an extent impacts the systemic delivery of SMPCs.

Materials and Methods

Materials and Equipment

Table 2-1 Materials

REAGENT or RESOURCE	SOURCE	IDENTIFIER
Antibodies		
Anti Human CD45-PE	Thermo Fisher Scientific	Cat# 12-0459-42
Anti Human CD11b-PE	Biolegend	Cat# 301306
Anti-Human CD235a - PE	Thermo Fisher Scientific	Cat# 12-9987-82
Anti-Human PDGFRα-PE	BD Biosciences	Cat# 556002
Anti-Human CD73	BD Biosciences	Cat# 550257
Anti-Human CD31 (PECAM-1)-PE	Thermo Fisher Scientific	Cat# 12-0319-42
Dead Cell Stain Kit	Thermo Fisher Scientific	Cat# L34975
Anti-Mouse CD31 (MEC 13.3)	BD Biosciences	Cat# 553370
Anti-Mouse Laminin	Sigma-Aldrich	Cat# L9393
Lamin A/C Monoclonal Antibody (mab636)	Thermo Fisher Scientific	Cat# MA3-1000
Anti-Rat Alexa fluor 488	Fisher Scientific	Cat# A11006
Anti-Rabbit Alexa Fluor 647	Fisher Scientific	Cat# A21245
Anti-Mouse IgG2b Fluor 568	Fisher Scientific	Cat# A21144
Surgical tools		
Betadine Solution	Fisher Scientific	Cat# NC0158124
Betadine Surgical Scrub	Fisher Scientific	Cat# 19-027132
Sterile Standard Cotton Swab	Fisher Scientific	Cat# 22-029-488
Serrated Hemostat	Fisher Scientific	Cat#12-000-171
Straight Locking Hemostats	Fisher Scientific	Cat#16-100-115
Student Halsey Needle Holder	Fine Science Tools	Cat# 91201-13
Mini-Colibri Retractor	Fisher Scientific	Cat#NC1536246
Iris Scissors	Fisher Scientific	Cat#12-460-104
High Precision 45° Curved Tapered Very Fine Point Forceps	Fisher Scientific	Cat# 12-000-131
Dumont Straight Forceps - Micro-Blunted Tips	Fine Science Tools	Cat# 11253-20
Dumont Curved Forceps - Micro-Blunted Tips	Fine Science Tools	Cat# 11273-20

Dumont Angled Forceps - Micro-Blunted Tips	Fine Science Tools	Cat# 11253-29
Silk Suture, Size 6-0	Fisher Scientific	Cat#50-118-0809
Ethicon Vicryl Suture, absorbable, Size 5-0	Fisher Scientific	Cat#NC9335902
32 G femoral artery catheter-Mouse (Recathco)	Fisher Scientific	Cat#50-196-383
Butterfly Needles	SAI infusion technologies	Sku#BFL-24
Disposable Hypodermic Needles (30G) (Exel)	Fisher Scientific	Cat#14-841-03
High Temperature Cautery Kit	Fine Science Tools	Cat#18010-00
Biological samples		
Human muscle tissues of fetal week 17/18	University of California Los Angeles (UCLA) Center for AIDS Research (CFAR) Gene and Cellular Therapy Core and Advanced Bioscience Material	N/A
Chemicals, peptides, and recombinant proteins		
DMEM/F-12, HEPES medium	Thermo Fisher Scientific	Cat# 11330032
DPBS	Gibco	Cat#14190-136
Collagenase, Type 2 (Collagenase II)	Worthington-Biochem	Cat# LS004177
Dispase II	Thermo Fisher Scientific	Cat# 17105041
Amphotericin B	Thermo Fisher Scientific	Cat# 15290018
Fetal bovine serum (FBS)	Thermo Fisher Scientific	Cat# 16000044
SkGM-2 Skeletal Muscle Cell Growth Medium-2 BulletKit	Lonza	Cat# CC-3245
TrypLE Express	Thermo Fisher Scientific	Cat# 12605010
Human bFGF	Proteintech	Cat# HZ-1285
Hank's Buffered Salt Solution	Thermo Fisher Scientific	Cat# 14175095

DNase I	Sigma-Aldrich	Cat#D4513
Matrigel	Corning	Cat#354277
SkGM™-2 Skeletal Muscle Cell Growth Medium-2 BulletKit™	Lonza	Cat#CC-3245
AO/PI	Nexcelom	
Experimental models: Organisms/strains		
C57Bl/6-NSG (wt-NSG)	N/A	N/a
mdx-NSG	N/A	N/A
mdxD2-NSG	N/A	N/A
Software and algorithms		
Zen 2.6 (blue edition)	Carl Zeiss Microscopy	
IMARIS Version 9.6	OXFORD Instruments	http://www.bitplane.com/imaris/imaris
Prism 9.1.1	GraphPad	https://www.graphpad.com

Equipment

- Benchtop Centrifuge (Eppendorf 5810 R)
- Microcentrifuge (Eppendorf 5425 R)
- Columbus Instruments Animal Treadmill: Exer-3/6
- Carl Zeiss 305 Stemi Microscope (Stand K Lab)
- Kent Scientific GenieTouch Syringe Pump
- Isoflurane anesthesia system (Get the information for the animal room downstairs).

Alternatives

- BD FACS ARIA was used to sort SMPCs. However, any other sorter that allows the purification of SMPCs can be used.

- Kent Scientific Genie Touch Syringe Pump was used for the infusion of cells. However, any other pump that allows the infusion of about 100 µl solution volume in a 500 µl syringe can be used.

Media and Buffers

Prepare all necessary buffers for digestion the day of

5% FBS Buffer

Reagent	Final concentration	Amount
DMEM/F12	n/a	472 ml
Fetal Bovine Serum	5%	25 ml
Penicillin/Streptomycin	0.5%	2.5 ml
Amphotericin	0.1%	500 µl
Total	n/a	500 mL

[Store at 4˚C]

Wash Buffer

Reagent	Final concentration	Amount
DMEM/F12	n/a	447 ml
Fetal Bovine Serum	10%	50 ml
Penicillin/Streptomycin	0.5%	2.5 ml
Amphotericin	0.1%	500 µl
Total	n/a	500 mL

[Store at 4˚C]

Digestion Buffer

Reagent	Final concentration	Amount
5% FBS Buffer	n/a	25 ml
Collagenase II	2 mg/ml	50 mg
Dispase II	1 mg/ml	25 mg
DNase I	50 µg/ml	
Total	n/a	25 mL

[Prepare fresh, leave at room temperature]

Skeletal Muscle Cell Growth Medium-2 kit

Reagent	Final concentration	Amount
Basal Medium	n/a	440 ml
GA-1000		500 µl
rhEGF		500 µl
Dexamethasone		500 µl
FBS		50 ml
L-Glutamine		10 ml
Total	n/a	500 mL

[This media can be aliquoted and stored in -20˚C for up to 6 months, when thawed add human bFGF (20 µg/ml) and then it can be stored at 4˚C for up to a week]

Step-by-step method details

All digestion steps and surgeries were performed in Class II biosafety cabinet using standard sterile techniques. After their sorting skeletal muscle progenitor cells are incubated in a humidified 37˚ C incubator with 5% CO_2.

The following protocol describes:

1- Mechanical and enzymatic digestion of lower hindlimb skeletal muscle week 18.
   Buffers are to be prepared the day of the digestion ahead of time to allow smooth digestion process.
2- In this protocol we used FACS lineage depleted skeletal muscle progenitor cells (SMPCs), however, researchers can use their cell of interest. This protocol provides an optimized method for cell delivery. SKGM2 media needs to be prepared ahead of sorting because it will be used for cells collection from sorters. ARIA sorters were used for cell purification. A 6-well plate needs to be coated with Matrigel ahead of cell collection from sorters for cell seeding.
3- The IA cell delivery should be performed on the following day of cell collection.
   a- In this protocol IA cell delivery was performed on NOD scid IL2Rγ^{null} mdx mice housed in an immunocompromised core facility.
   b- The number of cells seeded the day before the surgery is the limiting factor on how many mice can receive cells. Typically, 800K-1M cells are IA delivered/mouse. Researchers need to plan accordingly.
   c- Cell dissociation needs to be performed ahead of start of surgery of each mouse, i.e. if IA cell delivery is to be performed on three mice, then cell dissociation should not be performed once, but three times ahead of the cell delivery of each mouse.

Institutional permissions

Human fetal muscle tissues were obtained from the University of California Los Angeles (UCLA) Center for AIDS Research (CFAR) Gene and Cellular Therapy Core and Advanced Bioscience Resources (ABR). Use of human tissues was institutional review board-approved by the UCLA Office of the Human

Research Protection Program (IRB #15-000959). All animal work was conducted under protocols approved by the UCLA Animal Research Committee (ARC) (ARC-2006-119). Animals used in this study were housed in an immunocompromised core facility.

Researchers are reminded that permissions for the use of human tissues and for the use of laboratory animals must be obtained from their institutions and must be performed in accordance with relevant institutional and national guidelines and regulations.

Animals

Animals used in this study were housed in UCLA Humanized Mouse Core, an immunocompromised core facility. C57BL/6 mice were crossed with NSG mice to generate C57-NSG mice (referred to as wt-NSG). mdx-NSG mice: mdx/C57BL/10 mice were crossed to NSG mice to generate mdx-NSG mice. mdxDBA2 mice were a generous gift from Dr. Melissa Spencer, UCLA, and were crossed to NSG mice to generate mdxD2-NSG mice. Pax7-Zsgreen mice were purchased from The Jackson Laboratory (#029549) and bred in house. Pups were genotyped using TransnetYX to ensure allele mutations. All animals used in this study were backcrossed to the original C57Bl/6 and mdxC57Bl/10 backgrounds for at least five generations.

Skeletal muscle progenitor cells preparation

Timing: 10-12 hours

1- Once the tissue is received, skeletal muscle is separated from bones and skin and placed in wash buffer (in petri dishes on ice), the muscle is cut into small pieces, no fine cutting at this point. Leave on ice for 10 minutes.

   Note: Leaving cut tissue in wash buffer will help with blood release from the muscle tissue.

2- Aspirate wash buffer carefully, wash the muscle tissue another time with wash buffer, and then aspirate.

Note: If using the vacuum to aspirate make sure that the cut muscle is moved to one side of the petri dish, and the vacuum at a low setting to avoid aspirating any muscle pieces.

3- Add digestion buffer, maximum 12 ml per petri dish, and mince muscle tissue finely with small scissors in the hood at room temperature.

Note: this step should take about 10-12 minutes of mincing. Finer cut muscle tissue will allow easier digestion and easier filtering at later steps.

4- Place petri dish with the finely minced muscle tissue into a 37˚C incubator on a shaker for 10 minutes

5- After 10 minutes of incubation, remove petri dishes from incubator and triturate the digestion buffer by pipetting up and down with 5ml serological pipette. Place the petri dish back in the incubator for another 10 minutes.

Note: at this step the clumps will be a little challenging to pass through the pipette, but it should relatively be viscous.

6- Take the sample out after 10 minutes triturate again, this time it should be easy to pass through the 5 ml serological pipette tip.

Note: pipette the digestion buffer with a 1 ml pipette, if the sample goes through (with minor resistance) then the digestion is done. If not, put the petri dishes back in the incubator for a maximum of another 7 minutes.

7- Once digestion is over, add about 10 ml of wash buffer to the petri dish, carefully transfer the solution to a 50 ml conical tube, top up with another 5 ml of wash buffer. Filter through a 100 μm into a second 50 ml conical tube.

Note: wash the filter with about 2-3 ml of wash buffer to maximize cell retention into the solution. For this step you may need a total of 2 or 3 filters per petri dish.

8- Filter the sample through a 70 micron filter.

9- Spin the cells at 2000 rpm for 4 minutes at 4˚C.

10- Aspirate the supernatant, by inverting the 50 ml tube over a biohazard liquid waste container and aspirating the remaining media at the edge.

11- The pellets are then resuspended in sorting buffer by adding around 5 ml per 50 ml conical tube. Filter the cells through a 40 µm cell strainer. Top up the cell suspension to 20 ml of sorting buffer.

12- Spin the cells at 2000 rpm for 4 minutes at 4˚C.

13- Resuspend the pellet in 5 ml of sorting buffer and count the cells.

Note: 20 µl of cell suspension is added to 20 µl of AOPI. The cells are then loaded on cellometer cell counting chambers and counted using Nexcelom cellometer K2.

14- Prepare and stain the sample for FACS. Make sure to take out about 500K cells for FACS unstained and FMO controls. Skeletal muscle progenitor cells to be sorted are incubated with the antibodies (CD73, CD31, CD235a, CD45, CD11b, and PDGFRα) for 30 minutes and then washed before their sorting with 5 ml of ice cold FACS buffer for main sample, and 1 ml for control samples.

   a. 3 µl of human Fcx block for 10 million cells.
   b. 1.5 µl/million cells for all antibodies.
   c. 0.5 µl/million cells for viability dye.

15- Sort for SMPCs by collecting live lineage depleted cell fraction.

Note: of three hours of sort about 5-6 million SMPCs can be collected.

16- Spin collected cells at 1500 rpm for 5 minutes at room temperature, count the cells and seed at 1M cells/well of a 6 well plate.

17- Incubate SMPCs overnight in a cell culture incubator at 5% CO_2 and 37˚C.

Cell dissociation preparation for intra-arterial delivery

Dissociate cells freshly before the surgery of each mouse. Eppendorf microcentriguge 5424 R should be turned on and set to 4 ˚C. Skeletal muscle progenitor cells should be transferred to animal room on ice.

Hank's Buffered Salt Solution (HBSS) and SkGM-2 need to be ready ahead of cell dissociation (less than 50 ml will be needed).

Timing: About 30 minutes

1- In a Class II biosafety cabinet aspirate media from three wells of a 6 well plate. Wash the wells with DPBS and aspirate.
2- Add 0.5 ml per well TrypLE express.
3- Incubate for about 6-7 minutes in 37 ˚C incubator.
4- Take the plate out of the incubator and pipette gently with a P1000 pipette (to dissociate all the cells).
5- Add 0.5 ml/well of SkGM-2 to neutralize the TrypLE.
6- Transfer the cells from each well into a separate 1.5 Eppendorf tube.
7- Spin at 1500 rpm for 5 minutes in microcentrifuge.
8- **Note**: meanwhile prepare an Eppendorf tube for counting, and Eppendorf tube with 1 ml of HBSS.
9- When the spin is over, aspirate the supernatant from the Eppendorf tubes, resuspend the pellets from the three tubes with 0.5 ml of HBSS, pipette up and down to homogenize the pellets. Add the 0.5 ml cell suspension from the three tubes into one Eppendorf tube and centrifuge at 1600 rpm for 4 minutes in the microcentrifuge at 4 ˚C.
10- **Note:** Add 20 µl of cell suspension to the counting Eppendorf tube and add 20 µl AO/PI. Count as the cells are spinning.
11- Once centrifuged, aspirate the supernatant, and resuspended the cells in 120 µl of HBSS.
12- Transfer the cells along with 1 ml of HBSS on ice to the animal surgery room.

Intra-arterial delivery surgery

Before cell delivery we included a 45-minute downhill exercise regimen similar to described [134] to induce muscle injury in the lower hindlimbs of mice before systemic skeletal muscle progenitor cell delivery.

Skeletal muscle progenitor cells will be delivered through the femoral artery of either the left or right leg

of the mouse. Cells are detected in the muscles of the hindlimb where cells are injected, but not in the contralateral hindlimb muscles. In this protocol cells were delivered to the right leg femoral artery, therefore, right hindlimb muscles were collected for analysis. During the surgery, the mouse needs to be kept on a heating pad. Make sure that all equipment used are sterilized by wiping with 70% ethanol. Surgical tools need to be autoclaved the day before the surgery. A hot bead sterilizer is to be used to sterilize the surgical tools between mice. With an experienced hand, the surgery may take between 45 minutes to one hour. Help is needed for cell dissociation; one researcher can dissociate the cells while the other researcher is performing the surgery. The surgery is done under the microscope in a biohazard BSL class II cabinet, to ensure the maintenance of sterility. It is important to prepare a cage with a heating pad under it to warm up the bedding for the recovering mouse after the surgery.

Prepare the microscope under the hood, the warming pad, syringe pump, gas anesthesia system, and the surgical space. Make sure that all surgical tools are available in the hood. Ensure that all equipment are sterilized.

After surgery, researchers should optimize the optimal euthanization time of the mice for cell detection for their research needs. In this protocol we euthanized the mice after 48 hours of cell delivery to confirm cell homing to the muscle. Muscles are frozen using isopentane cooled in liquid nitrogen.

Timing: 1-1.5 hours/mouse

In this step

1- Place the mouse under anesthesia with isoflurane. About 3% isoflurane v/v induction with 1.5-2% v/v maintenance. Always test the anesthesia of the mouse by a toe pinch.

Critical: For the gas anesthesia system make sure that the system is connected to oxygen gas cylinder, isoflurane is filled to indicated level, the anesthetic gas scavenging system is up to date and finally the anesthesia masks can tightly fit the mouse nose to minimize anesthesia gas escape.

2- Use eye lubricant to prevent eye damage during the procedure once the mouse is under. Remove hair from the incision site preferably with a hair removal cream by placing a small amount and removing it with cotton swab in 30 seconds. With cotton swabs dipped into PBS, clean the area multiple times to remove any residual hair removal cream to avoid skin irritation. Scrub the incision area by doing at least three rounds of ethanol and betadine scrub wiping of the incision area (**Figure 2-2A**).

3- Transfer the mouse onto the microscope stage, with a heating pad under it (with an autoclaved procedure underpad on top).

Note: Secure the mouse hands and feet by taping them down with skin tape. Secure the nose cone in place once the mouse is positioned for the surgeon to access the inguinal region of the leg (**Figure 2-2A**).

4- Make an incision of about 1-1.5 cm in the inguinal region of the hindlimb with iris scissors. This step will expose the inguinal fat tissue. Carefully dissect through the inguinal fat tissue with forceps. Place two retractors to keep the incision open (**Figure 2-2, C1)**.

5- The femoral bundle, consisting of the femoral nerve, artery and vein should be seen/located at this step. Carefully dissect through the fascia layer to be able to access the femoral bundle (**Figure 2-2B**).

Critical: Use fine tip forceps, like the curved tapered forceps, to dissect through the fascia layer. It is critical to be cautious of getting too close to the femoral bundle to avoid piercing the femoral artery or vein.

Note: After the removal of the fascia layer, the incision region will dry out with time. Use small amount of saline to moisturize the region while operating when needed.

6- Alternating between the curved fine forceps, Dumont straight, curved and angled forceps dissect away the femoral nerve, then the femoral artery from the femoral vein. Start with small strokes parallel to the femoral nerve, then small strokes separating the femoral artery from the femoral vein.

Critical: Proceed with caution and delicately at this step as this part of the surgery is the most important and most sensitive. Any damage made to the femoral artery or vein will result in excessive uncontrollable bleeding. Any damage to the femoral nerve will result in hindlimb paralysis.

7- Gently pass the curved fine forceps underneath the femoral artery to dissect away from muscle.

Critical: Use blunt fine forceps at this step to avoid piercing the femoral artery.

8- Pass two 6-0 size silk sutures, about 3.5 inches in length, underneath the femoral artery (**Figure 2-2, C2-4**).

Note: one suture will be used to occlude the femoral artery upstream of the injection site, and one suture will be used to secure the catheter once inserted into the femoral artery around the injection site.

9- Use a hemostat to pull the silk suture upstream of the injection site to stop blood flow to the area.

Note: ensure that the hemostat is secured in its position, gentle pulling is only required. After occluding the blood flow in the femoral artery, the following steps should proceed fast to prevent any muscle damage. Do not occlude the femoral artery if the other lab member responsible for cell dissociation has not arrived with the cells.

10- Using a 30 G needle make a small puncture in the femoral artery downstream of the blood occlusion site (**Figure 2-2, C5-6)**.

11- Gently insert the 32G catheter, connected to the butterfly needle, into the femoral artery. Using the second suture downstream of the injection site, secure the catheter in place by tying it around the catheter (**Figure 2-2, C7**).

Critical: the 32G catheter and butterfly needle need to be flushed with saline before insertion into the artery to avoid the introduction of any air bubbles into the mouse blood stream.

12- Resuspend the cells in about 120 µl of HBSS by pipetting four-five times and then transfer the cell suspension into a 0.33 × 12.7 mm insulin syringe. Attach the needle to the calibrated pump and connect the tube of the butterfly needle to the insulin syringe.

13- Start cell infusion at 50 µl/min.

Critical: make sure that the tubing is completely free of air at the time of cell delivery.

14- Prepare another insulin syringe with 50-100 µl of saline to flush the tubing after cell delivery. Attach to the pump and start saline infusion.

15- Untie the suture securing the catheter and slowly retrieve the catheter from the femoral artery.

16- With the cauterizer, seal the needle opening in the femoral artery (**Figure 2-2, C8**).

Critical: be cautious and gentle with the use of the cauterizer as too much heat may occlude the femoral artery shut or may result in excessive bleeding.

17- Remove the suture occluding the blood flow to the femoral artery, blood flow should be seen restored into the femoral artery.

18- Wait for 2 minutes to observe that there is no bleeding occurring.

19- Fill the incision site with saline, restore the inguinal fat tissue to its location as permitted, and suture the incision with 5-0 absorbable Vicryl suture.

20- Turn off isoflurane and flush the anesthesia system with oxygen. Leave the mouse on the heating pad to recover for at least 30 minutes. Administer carprofen 5 mg/kg of body weight.

Critical: it is extremely important to monitor the recovering mouse. Mice usually become active, roaming in a cage, within 15 minutes. In a successful surgery the mouse will be moving its legs with a limp, but not paralysis.

Note: Depending on the researchers decision on euthnization time, the mice need to keep receiving carprofen for (5mg/kg) for at least four days after surgery.

Immunofluorescence staining

Mouse muscles were frozen in isopentane cooled in liquid nitrogen. Frozen muscles were serially sectioned at 10 μm thick cryosections. A Hydrophobic barrier was drawn around sections, then washed with 0.1% Tween in PBS (PBST). The sections were then fixed with 4% PFA for 10 minutes. A permeabilization step, if necessary, followed with 0.3% Triton X-100 in PBS at room temperature for 10 minutes. Sections were then blocked with 0.25% Gelatin, 0.1% Tween, 3% bovine serum albumin (BSA) and 10% goat serum (GS) in distilled water for 60 minutes at room temperature. Sections were then incubated in humidified chambers with primary antibodies overnight at 4°C in 0.25% gelatin, 0.1% Tween, 3% BSA and 1% GS. Sections were next incubated for 60 minutes with fluorophore-conjugated secondary antibodies diluted in PBS and 1% goat serum. DAPI vecatshield mounting media was then used to counterstain nuclei, coverslips were applied and nail polish was used to seal the coverslips. Images were captured using a Zeiss Axio Observer.Z1 microscope equipped with an AxioCamMR3 camera.

Imaris Quantification

At least 16-18 cross-sectional areas along the depth of the gastrocnemius muscle were used for human cells (LaminA/C+ nuclei) quantification in each mouse (n=3 mdx-NSG and n=3 mdxD2-NSG) after IA cell delivery. Tile images (at 20X) of each cross-section were captured by Zeiss Axio Observer.Z1 microscope equipped with an AxioCamMR3 with Zen (2.6) blue edition. Zen files with Czi extension were converted and stitched in Imaris File Converter and Imaris Stitcher to an ims format. Images were then analyzed in Imaris software version 9.6 where each image included an endothelial cell marker (CD31-488), human cell marker (LaminA/C-568) and DAPI. Spots feature was used to quantify human cells on the 568 channel, surface feature was used to quantify blood vessels with areas > 100 μm^2 on the 488 channel, and then the object-object statistics was used to count the number of human cells inside specified blood vessels. Quantification is shown as mean+SD, student t-test was used to compare the means of cells detected inside large vessels between mdx-NSG and mdxD2-NSG.

Statistical analysis

Prism Graphpad was utilized for statistical analysis (https://www.graphpad.com). One Way ANOVA with Tukey's multiple comparisons test was used for all data unless otherwise specified. Graphs show mean±SD, unless otherwise specified.

Results

Optimized intra-arterial cell delivery protocol to lower hindlimb

We have recently shown that hPSC-SMPCs generated in vitro have a similar developmental trajectory to embryonic-fetal SMPCs and that FW 17-18 SMPCs engraft similarly to enriched hPSC-SMPCs if TGF□ inhibitor treatment is applied to the muscle[64,74]. To evaluate whether SMPCs derived from FW 18 muscle tissue could be delivered systemically to multiple lower hindlimb muscles, we developed an IA delivery approach where SMPCs are injected into the femoral artery of 8-11 week-old-mice (**Figure 2-1**). In intramuscular (IM) cell engraftment experiments, muscles are typically injured 24 hours before cell delivery using cardiotoxin, barium chloride, or cryoinjury, to induce muscle damage and assist in cell engraftment [14,64,68,77,128,135,136]. As this is not feasible for systemic delivery, we included a 45-minute downhill exercise regimen similar to described to induce muscle injury in the lower hindlimbs of mice before systemic SMPC delivery [134]. Approximately 800K-1M SMPC were delivered to male wt-NSG, mdx-NSG or mdxD2-NSG mice (**Figure 2-2**). Matthias et al., described a detailed method for IA cell delivery through the femoral artery with successful detection of human cells in the muscle[137]. However, in their protocol after cell delivery the femoral artery is ligated, which in our hands caused a prominent ischemia injury in the gastrocnemius muscle (**Figure 2-3B**). Femoral artery ligation has been demonstrated to cause ischemic gastrocnemius muscle injury with a decreased blood flow to the limb below the ligation site[138–140]. Gerli et al. described a protocol for IA cell delivery re-establishing blood flow in the femoral artery after cell delivery, thus preventing muscle ischemia. However, the cells are not delivered at a constant flow rate, but rather with direct injection of cells using a 30 G needle[111]. Our approach is optimized from other IA delivery strategies by combining both delivery of the cells at a constant flow rate of 50 µl/min of cell suspension using a catheter, and by restoring blood flow after cell delivery, to prevent muscle ischemic injury (**Figure 2-3C**)[111,137].

The severity of DMD mouse model impacts systemic human skeletal muscle progenitor cells delivery into lower hindlimb muscles

Despite our efforts to prevent muscle injury after optimization of IA systemic delivery procedure, severe injury was detected in the lower limb muscles in mdxD2-NSG mouse model, but not in wt-NSG or mdx-NSG. To further investigate this finding, we performed histological analysis using hematoxylin and eosin staining on gastrocnemius muscle cross-sections of wt-NSG, mdx-NSG and mdxD2-NSG after SMPCs IA delivery. We observed prominent clotting occurring in large blood vessels in mdxD2-NSG, but not in wt-NSG and mdx-NSG (Figure 2-4). These findings indicate a pronounced difference in SMPC IA cell delivery in severely dystrophic mouse model compared to healthy and dystrophic mouse models.

Human skeletal muscle progenitor cells do not home efficiently to gastrocnemius muscle in all mouse models

To evaluate SMPC localization after their IA systemic delivery and whether the cells home to the muscle, right gastrocnemius muscles of the injected hindlimb, cross-sections were analyzed from all mouse models. In a successful cell delivery procedure, the human cells are expected to be detected outside the blood vessels and homing to the muscle (**Figure 2-5A**). Using both Zen 2.6 and Imaris Cell Imaging software we quantified human LaminA/C cells, a human cell perinuclear marker, in at least 16 cross-sections taken across the length of the muscle. Interestingly, we found significantly more human cells detected in gastrocnemius muscles per total cross-sectional area quantified in mdx-NSG and mdxD2-NSG compared to wt-NSG (**Figure 2-5B**). Of the total counted cells, significantly higher number of SMPCs, about 40%, quantified in wt-NSG gastrocnemius muscle cross-sections were detected outside the blood vessels, while only about an average of 20% and 18% were detected outside blood vessels in mdx-NSG and mdxD2-NSG, respectively (**Figure 2-5C**). Nonetheless, a significant number of human SMPCs were quantified inside blood vessels with about 60%, 80% and 85% on average in wt-NSG, mdx-NSG and mdxD2-NSG gastrocnemius muscle cross-sections (not shown). These findings suggest that SMPCs do not home efficiently to the muscle in all the mouse models.

Significantly more human skeletal muscle progenitor cells are detected in large blood vessels in severely dystrophic gastrocnemius muscles

Because of the high frequency of detecting human SMPCs inside blood vessels, we then focused on evaluating the localization of SMPCs within blood vessels (**Figure 2-6A**). On average of the total SMPCs quantified in all gastrocnemius muscle cross-sections, 60%, 84% and 62% of cells were observed inside the smallest blood vessel unit, the capillaries, in wt-NSG, mdx-NSG and mdxD2-NSG, respectively (not shown). To verify that this finding was not influenced by cell size of human SMPCs, we IA delivered SCs to mdx-NSG mice (n=2). For easier detection of the mouse SCs after delivery, we used a Pax7-ZsGreen transgenic mouse model that express enhanced green fluorescent protein for SCs isolation. Because SCs are fewer in adult mouse muscle tissue, only about 50K Zsgreen+ SCs were delivered after their sort. The Zsgreen SCs were still detected inside capillaries in the mdx-NSG model, suggesting that the size of human SMPCs is not a major factor for their detection in capillaries (**Figure 2-5B**). This finding also suggests that human SMPC and mouse SCs are equally not equipped with the machinery that would enable them to home to the muscle. We next sought to determine the differences in cell localization in large blood vessels between wt-NSG, mdx-NSG and mdxD2-NSG gastrocnemius muscles. Using Imaris Cell Imaging software we measured the area of larger vessels (veins/venules and arteries/arterioles) with human cells inside them and found that in mdx-NSG gastrocnemius muscles an average of 74 blood vessels with cross-sectional areas greater than 100 μm^2 had SMPCs detected in them, compared to an average of 154 blood vessels in mdxD2-NSG (**Figure 2-6B**). SMPCs detected inside 100 μm^2 blood vessel or greater in wt-NSG was negligible. Taken together we found that human SMPCs engraft inefficiently to lower hindlimb healthy and dystrophic muscles and are mainly detected inside blood vessels. We observed that human SMPCs localize in blood vessels distinctly in wt-NSG and mdx-NSG and mdxD2- NSG, with prominent clotting identified in mdxD2-NSG after human SMPCs IA systemic delivery. These findings suggest that the severity of DMD has impacted human SMPCs systemic delivery.

Discussion

Cell based therapies for muscle diseases including DMD offer enormous potential for personalized therapies especially in combination with gene correction [64,141]. The challenge faced is the lack of the ability to efficiently deliver cells to multiple muscles, which will be needed for neuromuscular diseases where multiple muscles are affected. Previously published reports for systemic delivery targeting multiple muscles did not deliver cells at a constant flow rate or were not able to re-establish blood flow back into the artery after cell delivery. Therefore, it was imperative to optimize an IA cell delivery protocol that provides delivered cells with the optimal conditions for muscle homing. Here we developed an optimized protocol for IA cell delivery by delivering the cells at a constant flow rate using a pump and catheter, and by establishing blood flow back into the femoral artery after cell delivery. This protocol confirmed its versatility with SMPCs delivered in three different mouse models, immunocompromised healthy and two dystrophic mouse models. Although this protocol has been developed for the delivery of SMPCs, it can be adapted for the delivery of other cell types, which we demonstrated by the delivery of mouse SCs, or for the delivery of gene therapy.

The optimization of the IA protocol led us to focus on evaluating the systemic delivery potential of SMPCs in healthy and DMD mouse models. We found that although SMPCs can reach multiple lower limb muscles after IA systemic delivery, the efficiency is too low to lead to robust long-term engraftment. Moreover, cells are detected in the tibialis anterior, gastrocnemius, hamstring and lateral thigh muscles of the injected leg (right or left) where the procedure is performed, but not in the contralateral hindlimb muscle (data not shown). Evaluation of gastrocnemius muscle structure after IA delivery showed severe clotting evident in mdxD2-NSG, but not in wt-NSG or mdx-NSG muscles. Despite the fact that about the same number of cells were delivered to all mice across the mouse models, significantly fewer human SMPCs were detected in the wt-NSG gastrocnemius muscles in overall quantified cross-sectional areas. Interestingly, of the total human SMPCs quantified in the wt-NSG gastrocnemius muscle cross-sections, significantly higher number of cells were detected outside blood vessels compared to mdx-NSG and

mdxD2-NSG. We therefore propose that less human SMPCs adhered to blood vessels in wt-NSG muscles compared to both DMD mouse models, which indicates a role the diseased microenvironment plays in the efficiency of systemic cell delivery.

Nonetheless, the previous findings do not suggest that human SMPCs are homing efficiently to healthy muscle, as the majority of human SMPCs quantified were still detected inside blood vessels in all mouse models. However, interestingly, the localization of human SMPCs was distinct between the mouse models, with cells in the mdxD2-NSG observed in large blood vessels forming clots, not observed in mdx-NSG and wt-NSG muscles. These findings suggest that hSMPCs are not endowed with the machinery to escape blood vessels to the surrounding muscle. This challenge could perhaps be overcome by overexpressing the components needed to enable cells to extravasate utilizing the machinery used by leukocytes [142].

In summary, here we optimized an IA cell delivery protocol that can be utilized for both cell delivery and gene therapy applications. We have shown that IA systemic based cell delivery can be performed using human SMPCs, but the efficiency is too low to be considered for use in therapeutic applications. We have shown differences in human SMPCs delivery in healthy, dystrophic and severely dystrophic muscles. These findings highlight the need to further understand the differences in skeletal muscle microenvironment between healthy, dystrophic and severely dystrophic mouse models, namely endothelial cells that line the interior surface of blood vessels. Future studies will likely need to develop combination therapies targeting both the diseased microenvironment as well as generating a better SC in parallel prior to use in regenerative medicine approaches for muscular dystrophy

Acknowledgments

First author is supported by fellowship from Qatar National Research Fund (QNRF)- Qatar Research Leadership Program (QLRLP9-G-3330003). Authors would like to thank Michael R. Hicks and Mandee Yang for their help with IA surgeries. We would like to thank Dr. Luisa Iruela-Arispe and post-doctoral fellow in her lab Dr. Georg Hilfenhaus for thoughtful discussions. We acknowledge FACS support provided by BSCRC Flow Cytometry Core at UCLA, we'd like to especially thank Felicia Codrea, Jessica Scholes, and Jeffrey Calimlim for their support. We acknowledge UCLA CFAR- Humanized Mouse Core for mouse colony husbandry. We acknowledge UCLA CFAR- Gene and Cellular Therapy Core and ABR for providing human muscle tissue. Illustrations in this paper were created with BioRender.com

Figures

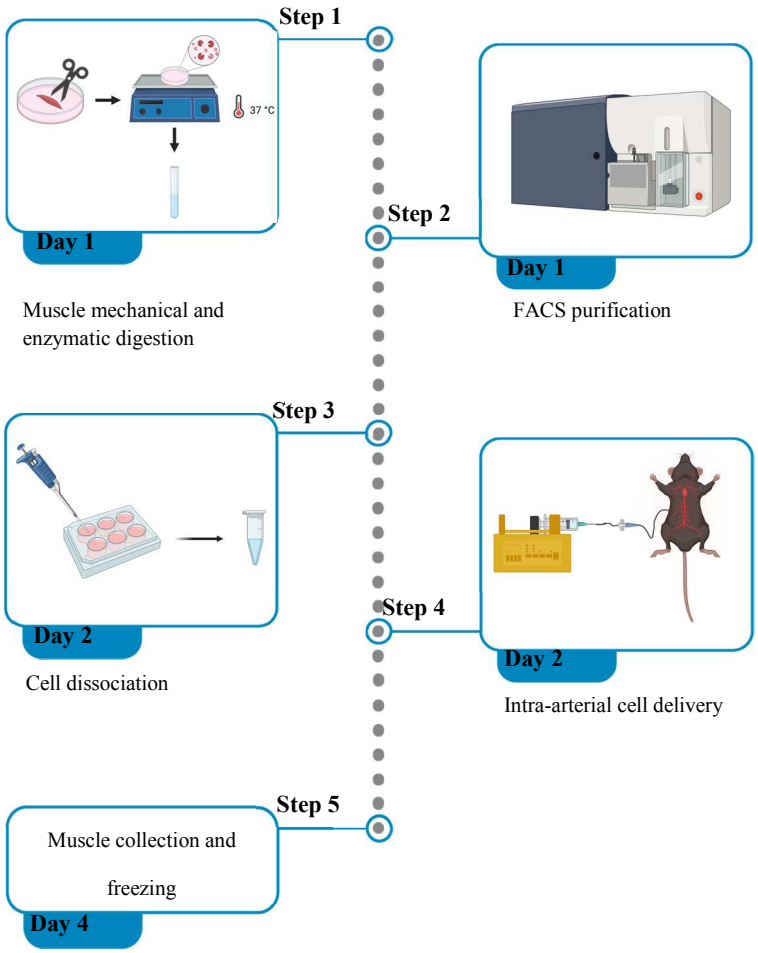

Figure 2-1: Schematic diagram illustrating the experimental workflow for Intra-arterial cell delivery protocol

Fetal week 13 (FW13) muscles are first digested then lineage depleted and cultured overnight. The next day cells are dissociated, and IA delivered at a 50 µl/min flow rate, and lower hindlimb muscles are collected 48 hours after surgery

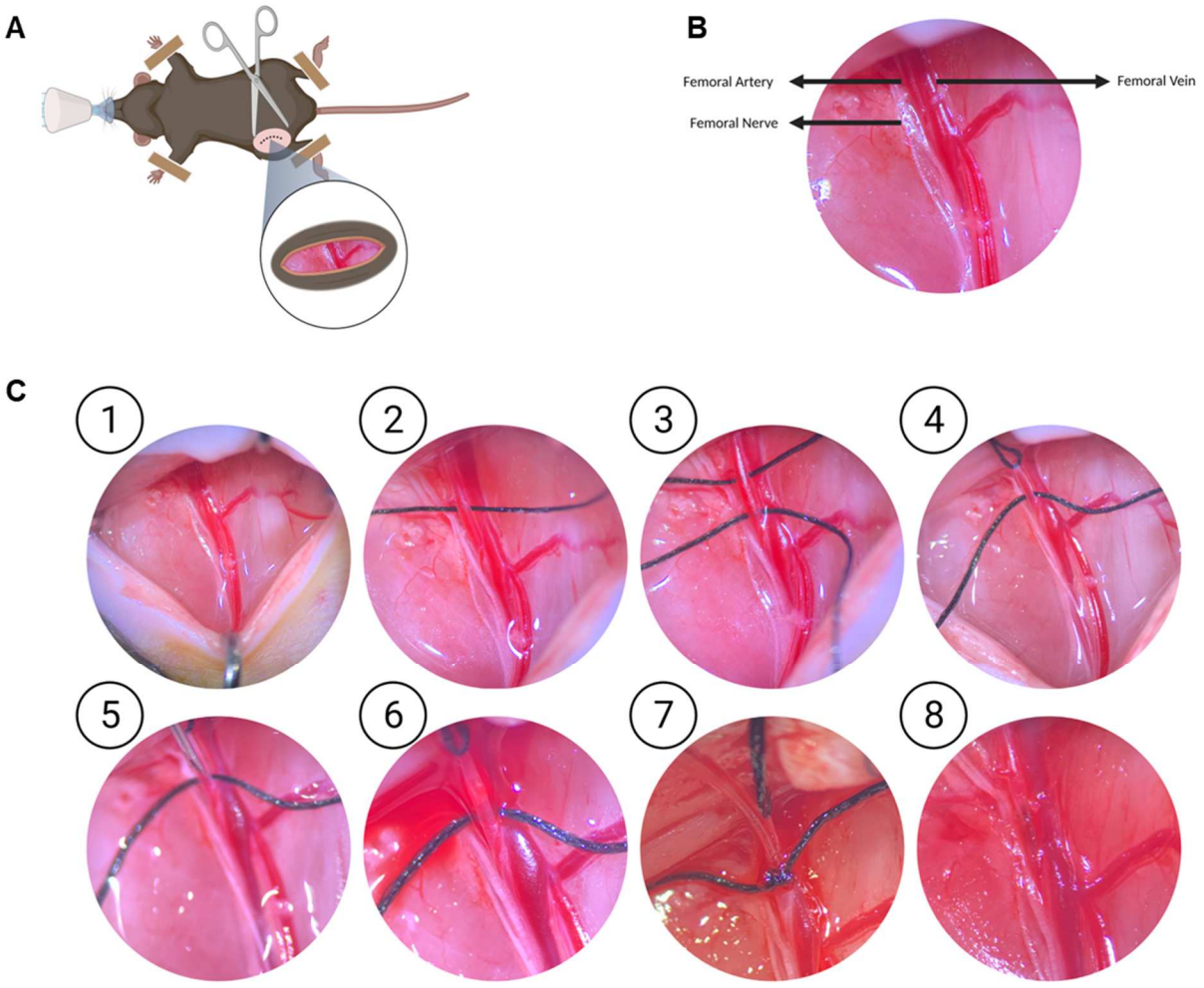

Figure 2-2: Step by step method of optimized intra-arterial cell delivery protocol to lower hindlimb

A) Schematic of the incision site.
B) The femoral bundle consisting of the femoral artery, femoral nerve and femoral vein are exposed once retractors are used to open the incision site.
C) Step by step images of the intra-arterial cell delivery procedure.

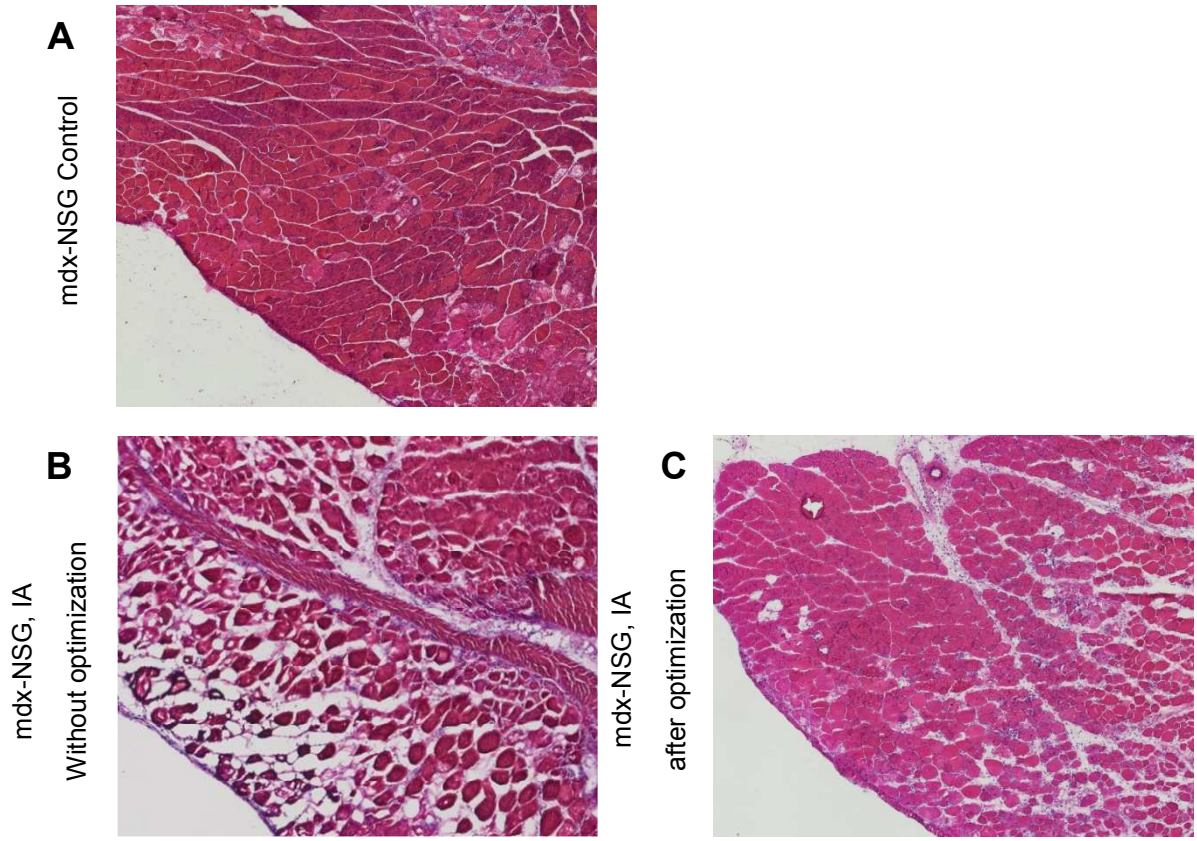

Figure 2-3: Optimized intra-arterial cell delivery prevents muscle ischemia

Histological analysis, hematoxylin and eosin staining of mdx-NSG gastrocnemius muscle 48 hours after intra-arterial cells delivery in the right femoral artery

A) control left gastrocnemius muscle.

B) mdx-NSG right gastrocnemius muscle with femoral artery ligation

C) right gastrocnemius muscle with intra-arterial cell delivery procedure optimization.

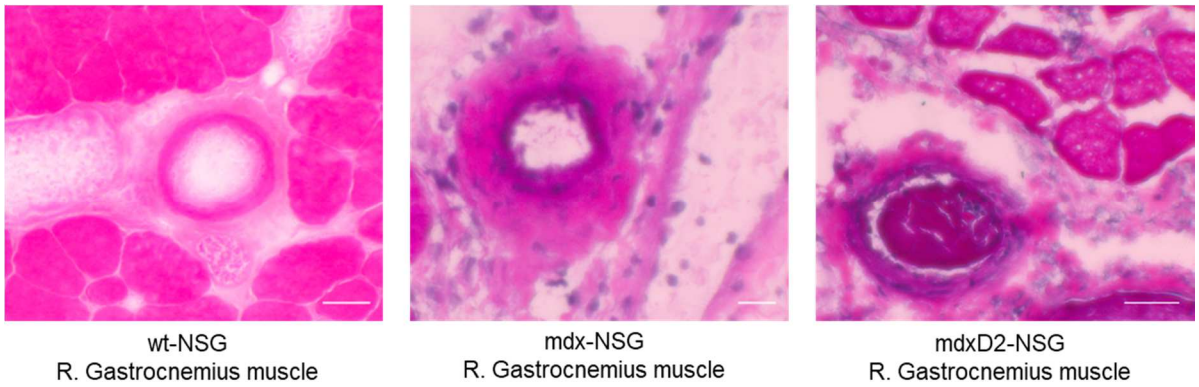

Figure 2-4: The Severity of DMD mouse model impacts cell delivery into lower hindlimb muscles

Histological analysis of right gastrocnemius muscle after IA cell delivery in wt-NSG, mdx-NSG and mdxD2-NSG muscles.

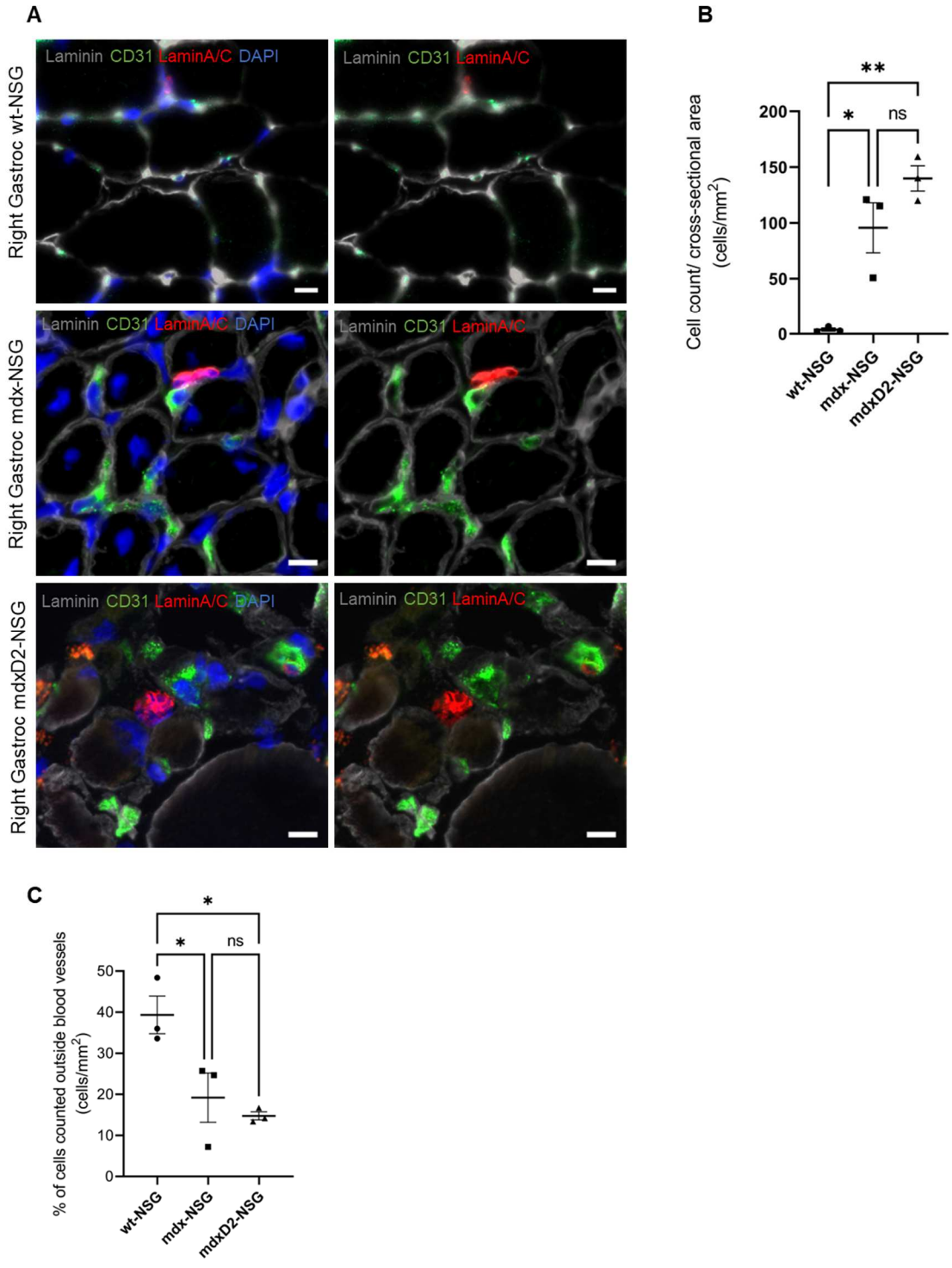

Figure 2-5: Optimal outcome of IA cell delivery

A) Gastrocnemius muscle cross-sections stained for human skeletal muscle progenitors (marked by human nuclei marker LaminA/C, red) and blood vessels (marked by endothelial cells marker CD31, green) with human cells detected outside the blood vessels. Scale bars at 10µm

B) Plot of the total human cells quantified/cross-sectional area of the gastrocnemius muscles of wt-NSG, mdx-NSG and mdxD2-NSG mouse models. One Way ANOVA with Tukey's multiple comparisons, errors bars show mean±SD,, *$P \leq 0.01$, *$P < 0.01$
C) Plot of the percentage of the total cells quantified outside blood vessels/cross-sectional area in wt-NSG, mdx-NSG and mdxD2-NSG muscles. One Way ANOVA with Tukey's multiple comparisons, errors bars show mean±SD, *$P \leq 0.05$

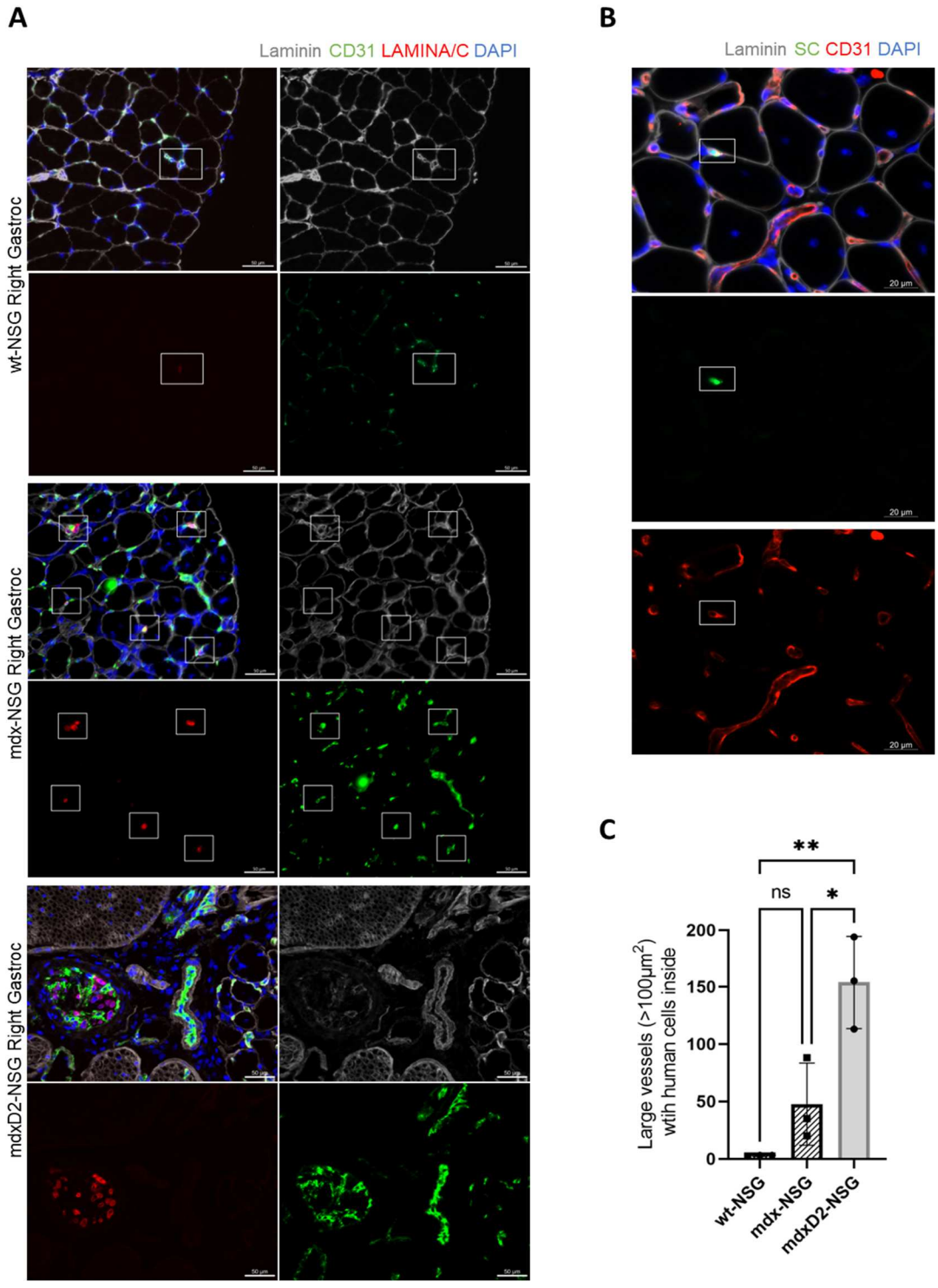

Figure 2-6: Significantly more human skeletal muscle progenitor cells are detected in large blood vessels in severely dystrophic gastrocnemius muscles

A) Cross sections of right gastrocnemius muscles of wt-NSG, mdx-NSG, and mdxD2-NSG showing human nuclei (H-laminA/C, red) 48 hours post IA cell delivery. SMPCs are detected inside blood vessels. Scale bars at 50 μm.
B) 50K of healthy mouse Zsgreen satellite cells (green) were IA delivered to mdx-NSG mice (n=2) and they were detected in capillaries. Scale bar 20 μm.
C) Comparison of the average number of blood vessels with a cross-sectional area > 100 μm^2 with hSMPCs detected inside in wt-NSG, mdx-NSG and mdxD2-NSG gastrocnemius muscles. One was ANOVA with Tukey's multiple comparisons, error bars represent mean ± SD, $*P<0.05$ $**P<0.01$.

CHAPTER 3: Single Cell Sequencing Maps Cellular Diversity in Increasing Disease Severity in Dystrophic Mouse Models

Introduction

Duchenne muscular dystrophy (DMD) is an X-linked recessive, severe progressive muscle wasting disease affecting ~1-5000 male live births [27–29]. Both devastating and fatal, DMD patients are diagnosed typically before their fifth year of age, are wheelchair bound in their teens, and prematurely die in their thirties. DMD is caused by a loss-of-function mutation in the *DMD* gene, the largest known gene in the human genome, that results in the absence of a functional dystrophin protein [30]. The regenerative capacity of skeletal muscle is mainly achieved through the differentiation of satellite cells, a muscle stem cell (MuSC) population present between the basal lamina and sarcolemma of the muscle fibers [3,119–121]. In DMD, impaired regeneration arises because either MuSCs are rendered dysfunctional due to impaired polarity establishment or because of progressive exhaustion [36–38]. Eventually, lack of proper regeneration leads to muscle fiber necrosis and generation of excess fibrotic tissue [39].

The most common mouse model used to study DMD is the mdx mouse, which has a nonsense mutation in exon 23 in the X chromosome that arose spontaneously in a C57BL/10 colony [41,42]. The mdx mouse model lacks dystrophin protein, has elevated plasma levels of muscle creatine kinase, and present histological muscle lesions like that of human disease. However, adult mdx mice do not fully recapitulate the human disease in terms of pathogenic progression. The mdx mouse model lifespan is not significantly reduced, regeneration of muscle fibers is not persistent, and lacks extensive fibro-fatty replacement of muscle fibers, thus the mdx model does not fully recapitulate human clinical disease progression [43–45]. Since the discovery of mdx mice, several other mouse models have been generated for DMD in different genetic backgrounds. One of which is the DBA/2-mdx (hereafter referred to as mdxD2) mouse strain. MdxD2 mice exhibit lower muscle weight, fewer muscle fibers and increased fibro-fatty deposition in comparison with the mdx strain [46]. Genetic modifiers on the DBA/2 genetic background, including osteopontin (Spp1), synonymous variant in Annexin A6 (Anxa6) exon 1, and polymorphisms in the

coding region of the latent TGF-β-binding protein 4 gene (Ltbp4), generates a more severe muscular dystrophy mouse model [47–49]. The exacerbated TGF-β signaling, increased inflammation, increased fibrosis and progressive weakness and atrophy in the mdxD2 mouse model better recapitulates the characteristics of DMD human disease [50–52].

Recently, Single-Cell RNA Sequencing (scRNA-seq) has improved our understanding of skeletal muscle and the cellular dynamics and myogenic continuum of homeostatic and regenerating muscle [20,22–25]. Recent studies have shown that endothelial cells (ECs) are incredibly heterogenous in healthy muscle [90–92]. Additionally, the cross-talk between ECs and MuSCs has been established [86,87,143]. However, a thorough characterization of skeletal muscle-resident cellular composition and dynamics in pathological conditions, such as in DMD mouse models, has not been described at the single-cell transcriptomic level. Moreover, in DMD mouse models there is little understanding of the cellular interaction between supportive cells in the muscle, such as stromal cells and macrophages, and ECs or how these interactions contribute to disease progression.

Here we evaluated the cellular composition of skeletal muscle-resident cell populations between healthy (wt-NSG), dystrophic (mdx-NSG), and severely dystrophic (mdxD2-NSG) mouse models, which are used routinely to evaluate cell-based therapeutics. We found that as the disease severity increases, the dynamics of cellular subpopulations of stromal cells, macrophages, and ECs changes. We show an increased prevalence of macrophages, both pro-inflammatory and anti-inflammatory macrophages, activated fibro-adipogenic progenitor (FAP) cells and, activated fibroblasts in the dystrophic and severely dystrophic muscles. Moreover, we identify a capillary EC subpopulation with an increased occurrence in severely dystrophic muscle. To further our understanding of EC differences between healthy and DMD conditions, and the role that the microenvironment plays in such differences, we investigated interactions between predicted released ligands from stromal cells and macrophages, and their potential differentially expressed target genes on EC, utilizing NicheNet analysis [144]. To the best of our knowledge, for the first time we have identified upregulation of extracellular matrix (ECM) genes in severely dystrophic ECs. We

have further identified the upregulation of plasminogen activator inhibitor-1 (PAI-1), a serine protease inhibitor that functions as procoagulant, in severely dystrophic ECs, indicating further functional impairment of ECs [145]. Overall, this work provides a resource for understanding how the cellular dynamics and skeletal muscle microenvironment changes as disease severity progresses and could provide potential avenues for considering when developing combination stem cell or single therapeutics for DMD.

MATERIALS AND METHODS

Experimental Model and Subject Details

Mice

All animal work was conducted under protocols approved by the UCLA Animal Research Committee (ARC) (ARC-2006-119). Animals used in this study were housed in an immunocompromised core facility. C57BL/6 mice were crossed with NSG mice to generate C57-NSG mice (referred to as wt-NSG). mdx-NSG mice: mdx/C57BL/10 mice were crossed to NSG mice to generate mdx-NSG mice. mdxDBA2 mice were a generous gift from Dr. Melissa Spencer, UCLA, and were crossed to NSG mice to generate mdxD2-NSG mice. Pups were genotyped using TransnetYX to ensure allele mutations. wt-NSG mice were genotyped for *Scid* and *Il2rg* alleles, mdx-NSG were genotyped for *Scid*, *Il2rg* and *mdx* alleles, mdxD2-NSG were genotyped for *Anxa6*, *Ltbp4*, *Scid*, *Il2rg* and *mdx* alleles. All animals used in this study were homogenous for *Il2rg* knockout and *Scid*. All animals used in this study were backcrossed to the original C57Bl/6 and mdxC57Bl/10 backgrounds for at least five generations. Western blot studies were performed on 11-week gastrocnemius muscle lysates.

Method Details

Muscle Digestion and Single-Cell suspension preparation

Gastrocnemius muscles were harvested from the right hindlimb of 8 weeks old wt-NSG, mdx-NSG, and mdxD2-NSG each separately. The muscles were first washed with wash buffer consisting of DMEM/F12, 10% FBS, 0.5% P/S and 0.1% Ampho. The muscles were then finely chopped in digestion buffer at room temperature (RT) in digestion buffer consisting of DMEM/F12, 0.5% P/S, 5% FBS and 500 u/ml Collagenase II. The chopped muscles were then placed in 37 ˚C incubator on a shaker for 20 minutes, pipetting with a serological pipette after 10 minutes for trituration. The digested muscles were then mashed with a 5 ml syringe plunger one for each sample. Digestion was stopped by adding ice cold wash buffer to each sample and the tissue slurry was then transferred to 50 ml conical tube. The tubes were then

filled with wash buffer and centrifuged at 600 g for 5 minutes. The pellets were resuspended in second digestion buffer consisting of DMEM/F12, 0.5% P/S, 5% FBS, 1.5 u/ml Collagenase D, and 2.4 u/ml Dispase. The tissue was then placed in a 37 ˚C incubator on a shaker for 15 minutes with intermittent trituration. Ice cold FACS buffer consisting of 2% FBS, 0.5% P/S in PBS was added to the tubes to stop digestion. The solution was filtered through a 70 um filter and then a 40 um filter. The cell suspension was then centrifuged at 400 g for 5 minutes at 4 ˚C, the pellet was resuspended with FACS buffer and centrifuged at 600 g for 5 minutes at 4 ˚C. Cell number was counted, resuspended in FACS buffer, stained with 1 µg/ml DAPI and kept on ice until sorted.

10X Genomics library preparation and sequencing

Single-cell suspension prepared as described above was sorted by BD FACSAria sorter for live cells at UCLA Broad Stem Cell Research Center Flow Cytometry Core. Standard gating strategies were applied to exclude debris, doublets and dead cells. The cells were pelleted and washed twice with BSA buffer, consisting of 1 × PBS with 0.04% UltraPure BSA, with 300 g centrifugation between washes for 2 minutes. Cells were then counted and resuspended in a 1200 cells/µl BSA buffer ratio. Chromium™ Single Cell 3' Library Construction was performed by the Technology Center for Genomics and Bioinformatics (TCGB) at UCLA. The samples were then sequenced using the llumina NovaSeq S2 (2×50).

Immunofluorescence staining

Mouse muscles were frozen in isopentane cooled in liquid nitrogen. Frozen muscles were serially sectioned at 10 µm thick cryosections. A hydrophobic barrier was drawn around sections, then washed with 0.1% Tween in PBS (PBST). The sections were then fixed with 4% PFA for 10 minutes. A permeabilization step, if necessary, followed with 0.3% Triton X-100 in PBS at room temperature for 10 minutes. Sections were then blocked with 0.25% Gelatin, 0.1% Tween, 3% bovine serum albumin (BSA) and 10% goat serum (GS) in distilled water for 60 minutes at room temperature. Sections were

then incubated in humidified chambers with primary antibodies overnight at 4°C in 0.25% gelatin, 0.1% Tween, 3% BSA and 1% GS. Sections were next incubated for 60 minutes with fluorophore-conjugated secondary antibodies diluted in PBS and 1% goat serum. DAPI vecatshield mounting media was then used to counterstain nuclei, coverslips were applied, and nail polish was used to seal the coverslips. Images were captured using a Zeiss Axio Observer.Z1 microscope equipped with an AxioCamMR3 camera.

Western blot

Muscle lysates and western blotting was carried using Western Blotting Application Solutions Kit from Cell Signaling Technology, following manufacturer protocol. In brief, gastrocnemius muscles were harvested from 11 weeks wt-NSG, mdx-NSG and mdxD2-NSG after euthanization, and immediately frozen in liquid nitrogen. Muscle samples were homogenized using Qiagen TissueRuptor in ice cold 2X cell lysis buffer supplemented with 1mM PMSF (100 mg of tissue to 1 ml of 2X buffer) and sonicated for 10-15 seconds. Samples were kept on ice at all times. Total proteins were quantified using Pierce BCA Protein Assay Kit. Samples were prepared with 1X SDS sample buffer, diluted from 3X SDS buffer consisting of 187.5 mM Tis-HCl (pH 6.8 at 25 ˚C), 6% (w/v) SDS, 30% glycerol and 0.03% (w/v) bromophenol blue, supplemented with 1/10 volume of 30X DTT reducing agent, consisting of 1.25 M dithiothreitol. Samples were heated to 95-100 ˚C for 5 minutes, and then cooled on ice for 5 minutes. Lysates, with a total protein of 30 µg, were resolved by SDS-PAGE using 1X running buffer carried out using Criterion Vertical Electrophoresis Cell (Bio-Rad) on 4-20% Gels (Bio-Rad) for 70-80 minutes at 120 V (depending on protein size). Gels were then transferred in wet conditions to nitrocellulose membrane using 1X transfer buffer for 120 minutes at 200 mA in cold room. Membranes were then blocked in TBST with 5% nonfat dry milk for 60 minutes at room temperature. Next, the membranes were incubated overnight at 4 ˚C with primary antibodies diluted in 3% BSA in TBST (1:1000). Membranes were then incubated in species appropriate HRP conjugated secondary antibodies (1:2000)

for 60 minutes at room temperature and developed with Pierce ECL Western Blotting substrate using ChemiDoc MP Imaging system.

Sirius Red histological stain

Picrosirius red stain solution was prepared by adding 0.1% direct red 80 and 0.1% fast green FCF to aqueous saturated Picric acid. Slides were then washed in Xylene for 5 minutes (2X), 100% EtOH for 2 minutes (2X), 90% EtOH for 2 minutes (2X), 80% EtOH for 2 minutes (2X), 70% EtOH for 2 minutes (2X), and dH2O for 2 minutes (2X). Tissue sections on the slides were then outlined with a pap pen. Picrosirius red solution was applied to the sections and left to incubate for 60 minutes. Slides were then washed in H_2O (10 dips), 70% EtOH (10 dips), 100% EtOH (2X 10 dips), and Xylene (2X 10 dips). Finally, slides were mounted with Permount mounting medium and imaged.

Quantification and Statistical Analysis

Quantification of immunofluorescence imaging

For capillary density: gastrocnemius muscle cross-sections were stained with CD31 and DAPI. Quantification was performed on n=3 of each mouse model for all the stainings. A total of 3-20X IF images were taken for 10 gastrocnemius muscle cross-sections per mouse, resulting in about 30-35 images for quantification per mouse. Using ImageJ quantified number of capillaries was then normalized to the total area of images counted. For PAI-1 colocalization with CD31 (5/6-20X IF images/mouse) and COLI, COLIV and COLVI (5/6-40X images/mouse), the Zen 2.6 blue edition was used for quantification. Quantified staining was divided by the area of the quantified images (mm^2).

Statistical analysis

Prism Graphpad was utilized for statistical analysis (https://www.graphpad.com). The *P* values for IF images quantification such as in COLI, COLIV, COLVI, CD31 and PAI-1,and western blot densitometric

analysis were calculated using One Way ANOVA with Tukey's multiple comparison test. Graphs show mean±SEM, unless otherwise specified.

Computational analysis: Seurat

Read alignment and gene-expression quantification of mouse scRNA-seq data was performed using the CellRanger Count pipeline (version 3.1.0, 10X Genomics). The CellRanger pre-built mouse reference package was used for read alignment (mm10 Ensembl 93). The filtered feature bc matrices output was then used to create Seurat object using Seurat package version 3.1.5. Quality Control (QC), data normalization and scaling, and detection of highly variable features were then carried out for each sample individually, with minimal alterations from the published workflow [146]. Briefly, quality control was performed by removing cells with fewer genes than 500, 800 and 800 and higher genes than 5000, 6000 and 6000 genes from the analysis in wt-NSG, mdx-NSG and mdxD2-NSG samples, respectively. Moreover, cells with more than 15% of UMIs mapped to mitochondrial genes were removed. Next, the data were normalized, highly variable genes identified and scaled using "SCTransform" with regression of cell cycle scores and percent mitochondrial genes. Next, dimensionality reduction by principal components (PCs) was calculated using "RunPCA" and to estimate the significant number of PCs to be used "ElbowPlot" function was used. Next, the uniform manifold approximation and projection (UMAP) embedding were calculated and visualized using "RunUMAP" and "UMAPPlot". Unsupervised clustering was carried using "FindNeighbors" and "FindClusters". Differentially expressed genes were then defined with "FindallMarkers" with Wilcox test, return.thresh set to 0.01, logfc.threshold set to 0.41, and with "min.pct" set to 0.25. Muscle clusters of each replicate from each mouse model were then defined (data not shown). The normalized Seurat objects were then merged using "merge". We found that for the merged Seurat object normalizing and scaling the data with the following functions "NormalizeData", "FindVariableFeatures" and "ScaleDATA", with regression of cell cycle score, resulted in a more conserved and better clustering of the datasets. Integration was then performed as below.

Computational analysis: Harmony integration

The merged Seurat object was used to integrate all cells from the different mouse models using Harmony[147]. Briefly, after running dimensionality reduction with "RunPCA", Harmony integration follows with "RunHarmony". In downstream analysis, Harmony embeddings were used for UMAP embeddings and clustering with "RunUMAP", "FindNeighbors" and "FindClusters". Differentially expressed genes between clusters were identified with "FindAllMarkers" using following parameters: test used "Wilcox", "return.thresh" set to 0.01, minimum expression fold change "logfc.threshold" set to 0.41, and minimum percent of cells expressing a certain gene "min.pct" set to 0.25 and minimum gene difference "min.diff.pct" set to 0.15 . Clusters were then identified from the integrated data based on gene expression (table S2) and visualized. A total of 20,920 cells were integrated after carrying Harmony integration from wt-NSG (4180), mdx-NSG (5723), and mdxD2-NSG (11017) (n=2/mouse model).

Computational analysis: Subset data

To obtain a Seurat object containing only desired cell type of the integrated data, endothelial cells for example, the "subset" function was used. The subset Seurat object goes through Seurat filtering and normalization, and Harmony integration workflows as described above.

Computational analysis: NicheNet Analysis

NicheNet analysis was performed as published code (nichenetr/seurat_wrapper_circos.md at master · saeyslab/nichenetr · GitHub) [144]. Briefly, the expression data of interacting cells was extracted from Seurat object of the integrated data. Then, the receiver cell population (EC) and sender cell populations (FAP and Mphage) were defined. The analysis was set as such the gene set of interest are the genes differentially expressed in ECs in dystrophic inflammatory environment compared to healthy state. Therefore, the condition of interest was set to mdx-NSG and mdxD2-NSG (each analyzed separately), and the reference condition was set to wt-NSG. Utilizing a model of already published ligand-target, ligand-receptor network and weighted integrated networks, NicheNet analysis is performed according to

the published workflow. The predicted ligand activity inferred active ligand-target links and average expression of inferred ligand activity between conditions are shown in **Figure 3-10**. Circos plots were then used to visualize groups the top predicted active ligands according to the strongest expressing cell type.

Gene Ontology Enrichment Analysis

Gene Ontology (GO) enrichment was performed using Metascape (Meta http://metascape.org/gp/index.html#/main/step1scape)[148]. In short, all statistically GO/KEGG terms were calculated and used for filtering. Significant terms were then hierarchically clustered into a tree based on statistical similarities. $P<0.01$

Table 3-1 Materials Resource Table

REAGENT or RESOURCE	SOURCE	IDENTIFIER
Antibodies		
Anti-Mouse CD31 (MEC 13.3)	BD Biosciences	Cat# 553370
Anti-Mouse/Human PAI1 [EPR21850-82]	Abcam	Cat# ab222754
Anti-Mouse/Human Fibronectin antibody	Abcam	Cat# ab2413
Anti-Mouse/Human Collagen IV antibody	Abcam	Cat# ab19808
Anti-Mouse Collagen Type VI Antibody	Fitzgerald Industries International	Cat# 70R-CR009X
Anti-Mouse Collagen Type I	Cedarlane Labs	Cat# CL50151AP-1
Rabbit IgG Isotype Control (Polyclonal)	R&D	Cat# AB-105-C
Mouse IgG2a Isotype Control	Biolegend	Cat# 401501
Anti-Rat Alexa fluor 488	Fisher Scientific	Cat# A11006
Anti-Rabbit Alexa Fluor 647	Fisher Scientific	Cat# A21245
Anti-Rabbit Alexa Fluor 568	Fisher Scientific	Cat# A11011
Anti-Rabbit HRP antibody	Cell Signaling technology	Cat# 7974S
Chemicals, peptides, and recombinant proteins		
Collagenase, Type 2 (Collagenase II)	Worthington-Biochem	Cat# LS004177
Dispase II	Thermo Fisher Scientific	Cat# 17105041
Collagenase D	Sigma-Aldrich	Cat# 11088882001
DMEM/F-12, HEPES medium	Thermo Fisher Scientific	Cat# 11330032
Amphotericin B	Thermo Fisher Scientific	Cat# 15290018
Fetal bovine serum (FBS)	Thermo Fisher Scientific	Cat# 16000044
Bovine Serum Albumin	Sigma Aldrich	Cat# A9418-100G

UltraPure BSA	Thermo Fisher Scientific	Cat# AM2616
Fast Green FCF	Sigma-Aldrich	Cat#:F7258-25G
Direct Red 80	Sigma-Aldrich	Cat#: 365548-25G
Picric Acid, Saturated	Sigma-Alrdrich	Cat#:5860-16
Critical commercial assays		
Thermo Scientific™ Micro BCA™ Protein Assay Kit	Fisher Scientific	Cat# PI23235
Western Blotting Application Solutions Kit	Cell Signaling Technology	Cat# 12957S
Pierce™ ECL Plus Western Blotting Substrate	Thermo Fisher Scientific	Cat# 32132X3
Experimental models: Organisms/strains		
C57Bl/6-NSG	N/A	N/A
mdx-NSG	N/A	N/A
mdxD2-NSG	N/A	N/A
Software and algorithms		
Zen 2.6 (blue edition)	Carl Zeiss Microscopy	
Prism 9.1.1	GraphPad	https://www.graphpad.com
CellRanger	10X Genomics	Cell Ranger Installation -Software -Single Cell Gene Expression - Official 10x Genomics Support
Seurat Version 3.1.5	Butler et al., 2018	Release Version 3.1.5 · satijalab/seurat · GitHub
Harmony	Korsunsky et al., 2019	GitHub - immunogenomics/harmony: Fast, sensitive and accurate integration of single-cell data with Harmony
NicheNet	Browaeys et al., 2020	GitHub - saeyslab/nichenetr: NicheNet: predict active ligand-target links between interacting cells
Metascape	Zhou et al., 2019	Metascape
ImageLab versions 5.1 and 6.1	Bio-Rad Labratories	

Results

scRNA-seq Reveals Skeletal Muscle Cellular Heterogeneity Between Healthy and DMD Immunodeficient Mouse Models

Using scRNA-seq we evaluated changes in cellular composition of 8-week-old healthy (wt-NSG), dystrophic (mdx-NSG) and severely dystrophic (mdxD2-NSG) gastrocnemius muscles. In brief, single-cell suspensions from gastrocnemius muscles were prepared, live cells were collected using fluorescence activated cell sorting (FACS), the single cell libraries were generated using the 10X Genomics Chromium platform and samples were sequenced on Illumina NovaSeq platform (n=2 muscles per mouse model, individually sorted and sequenced) (**Figure 3-1A**). Samples were first individually analyzed using Seurat by performing filtering, normalizing, scaling, and dimensionality reduction analysis (**Figure 3-2A-C**). After the initial analysis we were able to obtain and integrate a total of 4180, 5723 and 11017 cells from wt-NSG, mdx-NSG and mdxD2-NSG, respectively, using the Harmony package (**Figure 3-2 D,E, Table 3-1**). We used uniform manifold approximation and projection (UMAP) to visualize our scRNA-seq data set (**Figure 3-1B,C**)[147]. Unsupervised clustering resulted in a total of 46 different clusters in our integrated data which we merged based on gene expression into established identified cell types in skeletal muscle.

Muscle satellite cells (MuSC) were marked by *Pax7* and *Myf5* expression, myocytes (MC) were marked by *Myl1* and *Tnni2*, tenocytes (Teno) were marked by *Scx* and *Tnmd*, Schwann cells (Schwann) were marked by *Ptprz1* and *Sox10*, ECs were marked by *Pecam1* and *Cdh5* and pericyte (Peri) expressed *Rgs5, Abcc9*, and *Kcnj8* [22,23,74,149,150]. Because these mice are immunodeficient, they lack mature T-, B- and natural killer cells which are absent in our scRNA-seq set. However, we were able to detect clusters of immune cells namely neutrophils (Neutro), which are marked by *Cxcr2* and *S100a9*, mast cells (Mast), marked by *Cma1* and *Cma2*, and dendritic cells (DC), marked by *Ly6d* and *Flt3*, which are not ablated in NSG immunodeficient mouse models (**Figure 3-1E**). Additionally, we were able to capture macrophages, marked by *Ptprc* and *Cd68*, which constituted one of the largest clusters in mdx-NSG and mdxD2-NSG

muscles (**Figure 3-1D**). Stromal cells (Stromal), marked by *Pdgfrα* and *Ly6a,* constituted the largest cluster in wt-NSG muscles, and second largest clusters in mdx-NSG and mdxD2-NSG muscles. A list of the top 20 marker genes in each cell type cluster is provided in **Table 3-2**.

Muscle Satellite Cell Sub-Clustering Reveals Differences in Stem Cell States and a Subpopulation with Immune Gene profile in mdxD2-NSG mouse model

To explore the transcriptional changes between healthy, dystrophic and severely dystrophic MuSC, we subclustered a total of 269 MuSCs, performing further normalization and integration of MuSCs to identify cellular subtypes. Unsupervised clustering resulted in a total of 6 subpopulations in which we merged to 5 MuSC subtypes or derivatives based on their gene expression profile (**Figure 3-3**). We identified a cluster of differentiated or committed MuSC was marked by *Myog* (Myog+), and a cluster of quiescent satellite cells that was marked by *Pax7*, *Myf5*, *Chodl* and *Spry1* (Pax7+Myf5+Myod1-). Moreover, we identified two clusters of activated MuSC with *Pax7*, *Myf5* and *Myod1* expression, however one of these clusters only was enriched for Cxcr4 (Pax7+Myf5+Cxcr4+, and Pax7+Myf5+Myod+) (**Figure 3-3A,C**)**.** Interestingly, we have identified a MuSC cluster that had an immune signature expressing *C1qa/b*, *Lyz2* and *Cd53* (**Figure 3-3A**). This immune cluster compromised about 25% of MuSCs subtypes in mdxD2-NSG model (**Figure 3-3B,D**). A cluster of immune signature was identified recently in regenerating muscle where 21 days post injury about 50% of MuSC were identified as immuno-myoblast [24]. Collectively, our findings show differences in the MuSC cellular subtype compositions and states between healthy and dystrophic muscles, where it is clearly evident that the quiescent MuSCs compromise a smaller proportion of the total MuSCs in dystrophic environments, whereas a higher proportion of committed and differentiated MuSCs are evident as disease severity increases. We further identified a MuSC subpopulation with an immune signature that is highly expressed/present in severely dystrophic muscle.

Stromal Cell Sub-Clustering Reveals Stromal Subtypes arising in Dystrophic and Severely Dystrophic Muscle

One of the most striking differences that we observed in cellular composition between healthy, dystrophic and severely dystrophic skeletal muscles was the shift of the stromal cell population percentages, from being the most abundant cell type in healthy gastrocnemius muscle of wt-NSG mice, accounting for 62% of all cells, to lower proportions in dystrophic muscles at 42% in mdx-NSG and only 25% of all cells in mdxD2-NSG (**Figure 3-1D**). To discriminate the different stromal cell subtypes present, we subclustered a total of 7526 cells and performed differential gene expression within the cluster, performing further normalization and integration of the subset data (**Figure 3-4**). We were able to identify seven stromal cell subtypes and one subtype with immune identity (**Figure 3-4A**). Two subtypes, labeled *Dpp4*+ Stromal and *Cxcl14*+ Stromal, resembled fibro-adipogenic precursors (FAPS) which were similarly identified in non-injured tibialis anterior muscle [24]. The *Dpp4*+ stromal cell subtype has a similar gene expression signature to $Tie2^{high}Vcam1^{low}$ identified in C57Bl/10 WT model [151]. Interestingly, the proportion of these stromal cell subtypes decreases significantly in severely dystrophic environment falling from a total of 72% in healthy muscle, to 56% in dystrophic muscle, to only 31% in severely dystrophic muscle (**Figure 3-4B**). *Adam12*+ Stromal cell subtype, which appear to be activated fibroblast, expressed high levels of *Postn* [152] (**Figure 3-5A**). In mdxD2-NSG muscle, *Adam12*+ stromal cell subpopulation constituted about 33% of the total stromal cell composition making it the dominant stromal cell subpopulation, while only 15% and 3% of stromal cell composition in mdx-NSG and wt-NSG muscles, respectively. Additionally, *Cxcl5*+ stromal cell subtype, which appear to be activated FAPS, has been also described in an acute injury model [23,24], and in our dataset its proportion increases from about 2% in healthy wt-NSG muscle, to about 10% in dystrophic mdx-NSG, and 16% in severely dystrophic mdxD2-NSG environments (**Figure 3-4A,B**). Both *Adam12*+ and *Cxcl5*+ stromal subtypes have a $Tie2^{low}Vcam1$+ signature similar to published work in the mdx model, which emphasizes the power of scRNA-seq in further deconvoluting the cellular composition of skeletal muscle cell types [151].

In addition, we were able to identify a stromal cell subtype of traditional fibroblasts, labeled *Gdf10*+ Stromal, that has been described to inhibit adipogenesis and were shown to decrease in dystrophic muscles of Sarcoglycan-null mouse model [26]. In our dataset, the proportion of *Gdf10*+ Stromal subtype decreased from 20% in healthy wt-NSG muscle, to about 17% in dystrophic, to about 16% in severely dystrophic mdxD2-NSG muscle (**Figure 3-4B**). We have, moreover, identified three small clusters of stromal cells, labeled as *Thrsp+,Tenm2*+ Stromal, and *Cd53*+ Immune, that clustered separately from other stromal cells and had a distinct gene expression profile. Although the *Cd53*+ Immune cell subtype expresses *Ly6a* and *Pdgfra*, it also has an immune profile including expression of *Cd68* and *Cd53* (**Figure 3-4C**). Overall, we observed stromal cell subtype shifts with a reduction in FAPS, a reduction in traditional fibroblasts and an increase in activated fibroblasts in mdxD2-NSG compared to both wt-NSG and mdx-NSG (**Figure 3-4B**).

We further examined the differentially expressed genes (DEGs) upregulated in the total stromal cell cluster in mdxD2-NSG versus wt-NSG and mdx-NSG, followed by Gene Ontology (GO) enrichment analysis to identify enriched biological processes and signaling pathways (**Figure 3-4D,E**)[148]. The main GO enriched term was extracellular matrix (ECM) organization, with an enrichment of genes such as *Fn1*, *Fbn2*, *Fbln1,* and collagen genes such as *Col8a1*, *Col14a1* and *Col16a1* between mdxD2-NSG and wt-NSG, and *Adam12*, *Col12a1*, *Col14a1*, *Col8a1* and *Plod2* enriched in mdxD2-NSG compared to mdx-NSG. Of interest, the GO enriched term for regulation of chemokine production was observed in mdxD2-NSG compared to mdx-NSG (**Figure 3-4E**), with enriched genes such as *Il1r1*, *Postn, Ccl2*, *Ccl6*, *Cxcl12*, and *Cxcl5*. Overall, our findings helped identify stromal cell dynamics in healthy and muscular dystrophy states. Our scRNA-seq dataset provide a powerful tool that could further untangle stromal cells contribution to the severity of muscular dystrophy.

Macrophage Heterogeneity between Healthy, Dystrophic and Severely Dystrophic Skeletal Muscle

Next, we explored macrophage heterogeneity since it is well known that macrophages play pivotal roles in exacerbating muscle pathology in dystrophic muscles [50,153–156]. In our scRNA-seq dataset the frequency of macrophage cluster increases from 15% in wt-NSG, 639 cells, to 44%, 2560 cells, and 67%, 7426 cells, in mdx-NSG and mdxD2-NSG, respectively (**Figure 3-1D**). To further our understanding of macrophage population heterogeneity, we subclustered the macrophages (Mphage) and performed further normalization and integration of the subset data (**Figure 3-6**). Unsupervised clustering resulted in a total of ten different macrophage subtypes, which we merged into classically and alternatively activated macrophage clusters depending on their gene expression profile (**Figure 3-6A**)**.** Compared to dystrophic muscles, macrophage heterogeneity was less evident in healthy muscle with M2a-like Mphage and M2c-like Mphage subpopulations arising in mdx-NSG and mdxD2-NSG muscles (**Figure 3-6B**). Resident and *Lyve1*+ M2-like macrophages were the dominant subtypes of macrophage cellular composition in wt-NSG, accounting for a total of about 88%, while it accounted for a total of 52% of macrophages cellular composition in dystrophic mdx-NSG muscle, and only 40% in severely dystrophic mdxD2-NSG muscle (**Figure 3-6B**). M1-like macrophage cluster was mainly evident in dystrophic mdx-NSG muscle, constituting a proportion of about 20%, and severely dystrophic muscle with about 21% macrophage composition, while it accounted for only 4% of healthy muscle macrophage subtypes. We identified this cluster by the expression of *Ly6c2, Ccr2, Arg1, Vcan* and low expression of *Cx3cr1* (**Figure 3-6C**). This cluster has been described previously in the mdx muscle to exert profibrotic functions toward fibroblasts [157]. M2c-like macrophages is another predominant macrophage subtype in mdx-NSG muscle, constituting about 17%, and mdxD2-NSG muscle, at about 23% of total macrophage cellular composition, while it constituted less than 1% in healthy muscle macrophage subtype composition. M2a-like macrophage, although a small cluster, but it was detected comprising about 3% and 2% in mdx-NSG and mdxD2-NSG macrophages compared to about 1% in wt-NSG muscle. Other small macrophage subpopulations that clustered separately from other clusters were identified as Cd248 M2-like, Itgae resident macrophages and proliferative macrophages. These findings indicate the complexity of macrophage subpopulations in

both dystrophic and severely dystrophic environments and the involvement of dynamic macrophage phenotypes in the pathological process of muscular dystrophy [158]. GO analysis of DEGs in mdxD2-NSG macrophages showed enriched terms for degradation of the ECM, positive regulation of lipid localization, *Abcg1, Plin2, Lpl, Trem2, Spp1* and *Mif1,* regulation of cytokine production, with upregulated genes such as *Acp5, Arg1, Stat1, Mmp12* and *Pld3,* among others (**Figure 3-6D,E**).

Overall, our findings provide a tool to explore the dynamic existence of pro-inflammatory, M1 , and anti-inflammatory, M2, macrophages in the dystrophic and severely dystrophic muscle. Moreover, it provides insights on the involvement of immune cells in the severity of muscular dystrophy with their increased relative proportion compared to dystrophic and healthy skeletal muscles. Our scRNA-seq macrophage dataset and our integration method detected small populations of macrophages that need to be further studied to elucidate their pathological contribution to muscular dystrophy disease severity.

Characterization of Endothelial Cell subpopulations in Healthy, Dystrophic and Severely Dystrophic Skeletal Muscle

Endothelial cells are often underexplored in published scRNA-seq datasets, although their critical role in maintaining skeletal muscle homeostasis and in regeneration has been demonstrated by multiple groups [86,87,159,160]. To examine EC differences between healthy and dystrophic muscles, a total of 1150 ECs and pericytes were analyzed by performing differential gene expression within these clusters (**Figure 3-7A,B**). We used genes enriched in each EC subtype to annotate the clusters based on published literature [90,91](**Figure 3-7C, Table 3-3**). We were able to identify two large vessel EC clusters; arterial ECs (Arterial.EC) enriched for *Hey1*, *Gja4*, *Alpl* and *Sema3g* and venous ECs (Venous.EC) enriched for *Selp*, *Plvap* and *Vcam1*. Interestingly, in mdxD2-NSG we observed an increase in Venous.EC, compromising about 14% of total EC subpopulations, compared to about 11% and 5% in mdx-NSG and wt-NSG, respectively. We have also noticed a slight decrease in Arterial.EC proportion, at about 10%, compared to 12% and 14% in mdx-NSG and wt-NSG, respectively (**Figure 3-7D**).

Recently published scRNA-seq datasets in gastrocnemius muscle from C57BL/6n mouse 8 weeks of age, identified two capillary EC subtypes with one capillary EC population enriched in glycolytic muscle area, enriched with glycolytic fibers expressing myosin heavy-chain IIx or IIb isoforms[90]. We were similarly able to identify two distinct capillary EC populations, however, with a different gene signature. Capillary.EC.1 expressed *Aqp1*, *Pltp*, and *Aqp7* and Capillary.EC.2 expressed *Mme*, *Fbln1* and *Scara5* (**Figure 3-7A,C**). Interestingly, the proportion of these capillary EC subtypes changes drastically between healthy, dystrophic, and severely dystrophic muscles (**Figure 3-7D**). While Capillary.EC.1 contribute the highest proportion of EC in all the muscles, Capillary.EC.2 constitute 2% of total proportion in wt-NSG compared to 4% and 10% in mdx-NSG and mdxD2-NSG, respectively. We observed a pronounced decrease of both capillary EC subtypes in our dataset from 412 cells in wt-NSG, to 155 and 150 cells in mdx-NSG and mdxD2-NSG, respectively. We subsequently wondered if the decrease in capillary ECs in the dystrophic and severely dystrophic models reflected an increased frequency of stromal cells and macrophages or if there was a true decrease of capillary ECs in the dystrophic and severely dystrophic models. In cross-sections of the gastrocnemius muscle we quantified increased capillary density in mdxD2-NSG compared to both mdx-NSG and wt-NSG, while the capillary density of mdx-NSG was not significantly increased compared to wt-NSG (**Figure 3-8A**). Our observed result of normal capillary density in the mdx-NSG muscle, is similar to previous findings in 3-month-old mdx gastrocnemius muscle [96]. To infer differences between the two capillary EC subtypes we performed GO enrichment analysis on DEGs in each cluster (**Figure 3-8B,C**). Capillary.EC.1 top biological processes enriched terms were regulation of angiogenesis and regulation of vasculature development. Unexpectedly, Capillary.EC.2 enriched for ECM organization terms.

In addition, we identified a small EC subtype that expresses an immune profile such as *Ptprc* (CD45), *Cd44*, and *Spp1* in addition to the main EC markers *Pecam1* (CD31) and *Cdh5* (VE-Cadherin) (**Figure 3-7C**). Human umbilical cord ECs (HUVECs) have been shown to express CD45 in response to interleukin-1 (IL-1) *in vitro* [161]. Furthermore, in response to TGF-□ it has been shown that mitral valve ECs in the

heart express CD45 both *in vitro* and *in vivo* [162]. Therefore, we identified this subtype as an activated subtype of ECs (Activated.EC) (**Figure 3-7A**). It is noteworthy that the Activated.EC subtype constitutes 13% of the total ECs in mdxD2-NSG, 6% in mdx-NSG and only 2% in wt-NSG.

When exploring the DEGs upregulated in mdxD2-NSG EC, we found an enrichment for neutrophil degranulation and neutrophil chemotaxis GO terms, with genes enriched such as *Cd63, Fcer1g, Gsn, Ctss* and *Alad,* and enriched GO terms for positive regulation of cell migration, *Calr, Col18a1, Col1a1, Fn1, Plvap* and *Thbs4* (**Figure 3-7E,F**). Interestingly, one of the enriched GO terms in mdxD2-NSG versus mdx-NSG was platelet activation, signaling and aggregation, with genes enriched such as *Cd63*, *Col1a1*, *Fn1*, *Plek*, and *Col3a1* (**Figure 3-7E**). Although not shown on the top enriched terms, we also found that the platelet activation, signaling and aggregation enriched GO term, with genes expressed such as *Cd63*, *Clu*, *Col1a1*, *Fcer1g*, *Fn1*, *Plek*, and *Pf4* were upregulated in mdxD2-NSG EC DEGs vs. wt-NSG. Taken together, ECs in the severely dystrophic mouse model showed an increased ECM gene upregulation, especially genes involved in collagen formation, regulation of cell adhesion and platelet activation and aggregation. When comparing DEGs upregulated in mdx-NSG ECs vs. wt-NSG, enriched terms for ECM organization or degradation was lacking and not evident (not shown). Because of these prominent differences especially in ECM upregulation in the severely dystrophic ECs, which has not been previously shown in pathological muscular dystrophy conditions, we focused our attention into validating these findings.

Ligand-Gene Interaction Model Identifies Intercellular Communication Influencing Endothelial Cells in Dystrophic Muscles

The skeletal muscle microenvironment and intercellular network interactions is critical in maintaining muscle homeostasis in healthy and diseased conditions. Released ligands from cell populations, stromal cells and macrophages for instance, can govern and drive cellular gene expression changes. Therefore, to address our question of whether the dystrophic microenvironment led to changes and upregulation of

ECM gene expression, among others, between healthy, dystrophic and severely dystrophic muscles, we investigated the possible interaction between released ligands from stromal cells and macrophages and their target genes on EC. We carried out NicheNet analysis, a computational tool that uses gene expression data of interacting cells and combines it with existing knowledge to infer ligand-to-target interactions [144] (**Figure 3-9**). In our NicheNet analysis, we prioritized ligands released from stromal cells and macrophages driving the differential expression observed in dystrophic and severely dystrophic ECs. Because the prioritization of ligands in NicheNet analysis is not directly related to their expression level, we confirmed the upregulation of the prioritized ligand in diseased conditions. We indeed found some ligands lowly expressed in mdx-NSG and mdxD2-NSG stromal cells and macrophages, therefore when performing further analysis and validation experiments, we only considered target genes affected by upregulated ligands in the diseased conditions (data not shown). The top five predicted ligands upregulated in stromal cells and macrophages most likely influencing gene expression differences in mdx-NSG EC are *Tgfb1*, disintegrin and metalloprotease 17 (*Adam17*), selectin P ligand (*Selplg),* apolipoprotein E (*Apoe)*, and interleukin 1□ (*Il1b*). The top five predicted ligands released in mdxD2-NSG were *Tgfb1*, *Apoe, Tnf*, colony stimulating factor 1 (*Csf1*), *Il1b* (**Figure 3-10A, B**). We further explored predicted ligands differentially expressed in mdxD2-NSG compared to mdx-NSG stromal cells and macrophages most likely regulating target genes in ECs, and the identified ligands were *Tgfb1*, *Adam17*, bone morphogenetic protein 2 (*Bmp2*), midkine (*Mdk*) and osteopontin (*Spp1*) (**Figure 3-10C**). These results come in agreement with extensively studied cytokine and chemokine signaling in dystrophic muscles and are further validated by our scRNA-seq dataset and NicheNet analysis [163,164]. The heatmap of predicted ligand target genes and their regulatory potential in ECs for mdx-NSG and mdxD2-NSG is shown in **Figure 3-10D-F**. To confirm target gene differential expression on ECs we plotted the average expression of target genes between diseased and healthy conditions (**Figure 3-10G-I)**. The main intercellular interactions of stromal cell-specific, macrophage-specific, and common ligands and their potential target genes were mapped on circle plots to simplify cell-cell interaction visualization (**Figure 3-**

9 A-C). We found that the main ligands driving ECM expression in mdxD2-NSG ECs were TGF-□, ostepontin, TNFα and IL-□. While in mdx-NSG EC Hgf and TGF□ were the main ligands upregulating ECM expression. Because ECM genes were notably upregulated in mdx-NSG and mdxD2-NSG EC, we simplified their expression visualization, along with other genes of interest, in **Figure 3-9 D,E**. Collectively, NicheNet analysis highlighted top predicted ligand interactions released from stromal cells and macrophages with their potential target genes on ECs in dystrophic and severely dystrophic muscles identifying TGF-□ pathway as the main upstream signal driving EC gene expression changes.

Dystrophic and Severely Dystrophic Endothelial Cells have Increased ECM Deposition

To validate our findings of increased ECM expression of vascular ECs, especially in severely dystrophic muscles, we examined collagen IV, collagen I, and collagen VI deposition around capillaries in cross sections of wt-NSG, mdx-NSG and mdxD2-NSG muscles (**Figure 3-11A-C and Figure 3-12**). We found significantly higher deposition of collagen IV, collagen I and collagen VI in mdxD2-NSG compared to both mdx-NSG and wt-NSG, while higher deposition of collagen I and collagen VI were evident in mdx-NSG compared to wt-NSG (**Figure 3-11A-C**). In addition, one of the major ECM genes that was upregulated in dystrophic and severely dystrophic muscle EC was fibronectin (FN) encoded by *Fn1* (**Figure 3-9E**). ECs from murine models are difficult to isolate in large numbers, therefore, to examine the protein expression of fibronectin in the different mouse models we performed western blots (WB) using whole gastrocnemius muscle lysates. We detected significantly increased protein abundance of fibronectin in mdx-NSG and mdxD2-NSG muscles compared to wt-NSG (**Figure 3-12A)**. When muscle cross-sections were examined, fibronectin had increased deposition around mdx-NSG and mdxD2-NSG ECs compared to wt-NSS (**Figure 3-11D**). We further confirmed these findings with Sirius red staining in muscle cross-sections (**Figure 3-12B**). Collectively, we confirmed that the upregulation of ECM genes in ECs, regulated mainly by TGF-□ signaling predicted by NicheNet analysis, translates to protein expression in muscle cross-sections of healthy, dystrophic and severely dystrophic muscles.

Serpine1, which encodes PAI-1, was one of the genes detected to be upregulated in severely dystrophic ECs in NicheNet analysis (**Figure 3-9B**). It was predicted by NicheNet analysis that *Serpine1* is regulated by TGF-β, IL-1□ and TNF signaling (**Figure 3-10E**). To further explore this finding, we assessed *Serpine1* expression in ECs and verified its enrichment in mdxD2-NSG EC (**Figure 3-9E**). In order to confirm if our gene expression data corresponds to protein expression, we performed immunostaining of PAI-1 on muscle cross-sections and we found that it colocalizes with some, but not all, ECs (CD31+) in mdxD2-NSG (**Figure 3-11E, 3-12C**). Overall, we show the upregulation of ECM genes by dystrophic and severely dystrophic ECs, and the upregulation of PAI-1 especially in the severely dystrophic ECs.

Discussion

Recent advances in scRNA-seq technology have allowed for the evaluation and dissection of skeletal muscle-resident cell populations in homeostatic and regenerating states [22–25,151]. These studies collectively described a comprehensive scRNA-seq datasets and provided insights into the complexity and diversity of normal muscle-resident populations, and how cell populations change during muscle regeneration. However, limited studies have examined cellular heterogeneity of skeletal muscle at single cell resolution in pathological conditions, for instance in inflammatory muscle diseases such as in DMD mouse models [165]. Many studies have demonstrated that the diseased environment plays an enormous role in the effectiveness of therapies [166,167]. Therefore, utilizing scRNA-seq, here we focused on evaluating the changes in the cellular composition and microenvironment as disease severity increases in mouse models of DMD. We explored the transcriptional differences and heterogeneity within different muscle-resident populations including MuSCs, stromal cells, macrophages, and EC populations between healthy, dystrophic, and severely dystrophic muscles.

MuSC has been demonstrated to be a heterogenous population influenced by microenvironment signaling [168,169]. The first scRNA-seq study that focused on MuSC heterogeneity in homeostatic muscle constituted of only 21 FACS isolated MuSCs [20]. Since then, multiple groups examined the temporal dynamics of MuSCs during regeneration where quiescent MuSCs, activated MuSCs [25], progenitors, committed progenitors, mature skeletal muscle [23,25], and immunomyoblasts [24] have been described. We described a MuSC subpopulation that expressed an immune profile that constitutes about 25% of MuSC in the mdxD2-NSG muscle, similar to described in the regenerating muscle [24]. The functional validation of this subpopulation is necessary in the severely dystrophic muscle to understand its implications in the disease context. We further described four MuSC subpopulations that are transcriptionally distinct in healthy, dystrophic and severely dystrophic scRNA-seq integrated dataset, with an increased proportion of committed (*Myod1*+) and differentiated (*Myog*+) MuSC in the dystrophic and severely dystrophic muscle. Furthermore, we were able to identify, in dystrophic and severely dystrophic skeletal muscles, cell

populations that have been otherwise described in healthy regenerating muscle after acute injury, such as *Cxcl5*+ stromal cell subpopulation [23,24]. We were able to further describe the dynamic changes of macrophages with the co-existence of both pro-inflammatory, M1-like macrophage, and anti-inflammatory, M2-like macrophage, signatures in the dystrophic and severely dystrophic skeletal muscles.

The EC skeletal muscle-resident population is an understudied cell population although its implications for cell-based therapeutics are critical. In the mdx mouse model, it has been reported that the vascular changes are age-dependent, with impaired angiogenesis, migration, and proliferation of ECs in *vitro* and *in vivo* in older mdx mice [96–98]. To understand the role of the microenvironment in EC transcriptional changes in dystrophic and severely dystrophic muscles, we were interrogated intercellular communication with predicted ligands released from stromal cells and macrophages and their targets in dystrophic ECs utilizing NicheNet analysis [144]. Our analysis identified the TGF-□ pathway, with expression of *Spp1* and *Tgfb1,* as one of the main upstream signals driving EC changes in both dystrophic and severely dystrophic muscles. Recent work has provided evidence that osteopontin promotes fibrosis and upregulates collagen expression in mdx fibroblasts by enhancing TGF-□ signaling [164]. To the best of our knowledge, we are showing here for the first time that in severely dystrophic environment a subset of capillary ECs upregulates ECM genes including *Col1a1*, *Col3a1*, *Col4a1, Col6a1* and *Fn1*. We further confirm the significant increase of Collagen IV, I, VI and fibronectin deposition around capillaries in severely dystrophic environment compared to both dystrophic and healthy environment. Our findings are in line with reported thickened connective tissue around capillaries of DMD patients [93]. Nichenet analysis moreover identified PAI-1, encoded by *Serpine1*, as an upregulated gene in ECs. We have also seen a similar upregulation of *Serpine1* in stromal cells and macrophages (data not shown). PAI-1 is a procoagulant and inhibits degradation of clots when they arise [170]. We confirmed upregulation of PAI-1 protein expression with immunofluorescence imaging in muscle cross-sections, further indicating EC impairment in severely dystrophic muscles.

In summary, we have used scRNA-seq of gastrocnemius skeletal muscle to investigate differences in the microenvironment and cellular constitution as disease severity increases in mouse models of DMD. We have identified critical changes in transcriptional profiles of MuSC, stromal cells, macrophages and ECs regulated by DMD disease progression. Our scRNA-seq data provides the community with a tool to further explore muscle-resident cell type changes and differences in muscle make up between healthy, dystrophic and severely dystrophic phenotypes. Our work further highlights that future studies will likely need to develop combination therapies targeting both the diseased microenvironment in addition to delivering new cell, genetic or other novel therapeutics to DMD patients.

LIMITATION OF THE STUDY

The confirmation of muscle-resident subpopulations identified in this study will require the use of combination approaches of *in vivo* and *in vitro* studies to validate and determine their role in driving disease progression in dystrophic and severely dystrophic mouse models. Moreover, future studies will require investigating ECs in DMD disease model to evaluate their functional role and potential for targeting to restore a healthy phenotype.

Acknowledgments

First author is supported by fellowship from Qatar National Research Fund (QNRF)- Qatar Research Leadership Program (QLRLP9-G-3330003). H.X was funded by NIAMS/NIH (R01AR064327). E.S is funded by California Institute for Regenerative Medicine (CIRM) bridges stem cell scientist training program (EDUC2-08411). M.R is supported by NIAMS/NIH supplement fellowship (3R01AR064327-06A1:S1), A.P. Giannini Foundation, Ford Foundation, and University of California President's Postdoctoral Fellowship Program. P.C is supported by NIAMS/NIH fellowship (F31AR078640), the Center for Duchenne Muscular Dystrophy (CDMD) at UCLA Azrieli Graduate Student Award, BSCRC pre-doctoral training program and NIH T32 award (T32 AR065972). D.G is funded by HHMI Gilliam Fellowship for Advanced Study (GT11468). M.H was funded by Muscular Dystrophy Association (MDA) grant (#629098) and by Broad Stem Cell Research Center at UCLA (BSCRC). This work was funded by CIRM Quest grant (#DISC2-08824) and NIAMS/NIH grant (R01AR064327). We would like to thank Dr. Rachelle Crosbie and Dr. Luisa Iruela-Arispe and post-doctoral fellow in her lab Dr. Georg Hilfenhaus for thoughtful discussions. We acknowledge FACS support provided by BSCRC Flow Cytometry Core at UCLA, we'd like to especially thank Felicia Codrea, Jessica Scholes, and Jeffrey Calimlim for their support. We acknowledge the Technology Center for Genomics and Bioinformatics at UCLA for their help and services provided for 10X Genomics scRNA-seq library preparation and sequencing. We acknowledge the BSCRC microscopy core at UCLA, especially Dr. Nathanael Prunet for his support. We would like to acknowledge the UCLA CFAR- Humanized Mouse Core for mouse colony husbandry. Illustrations in this paper were created with BioRender.com

Figures

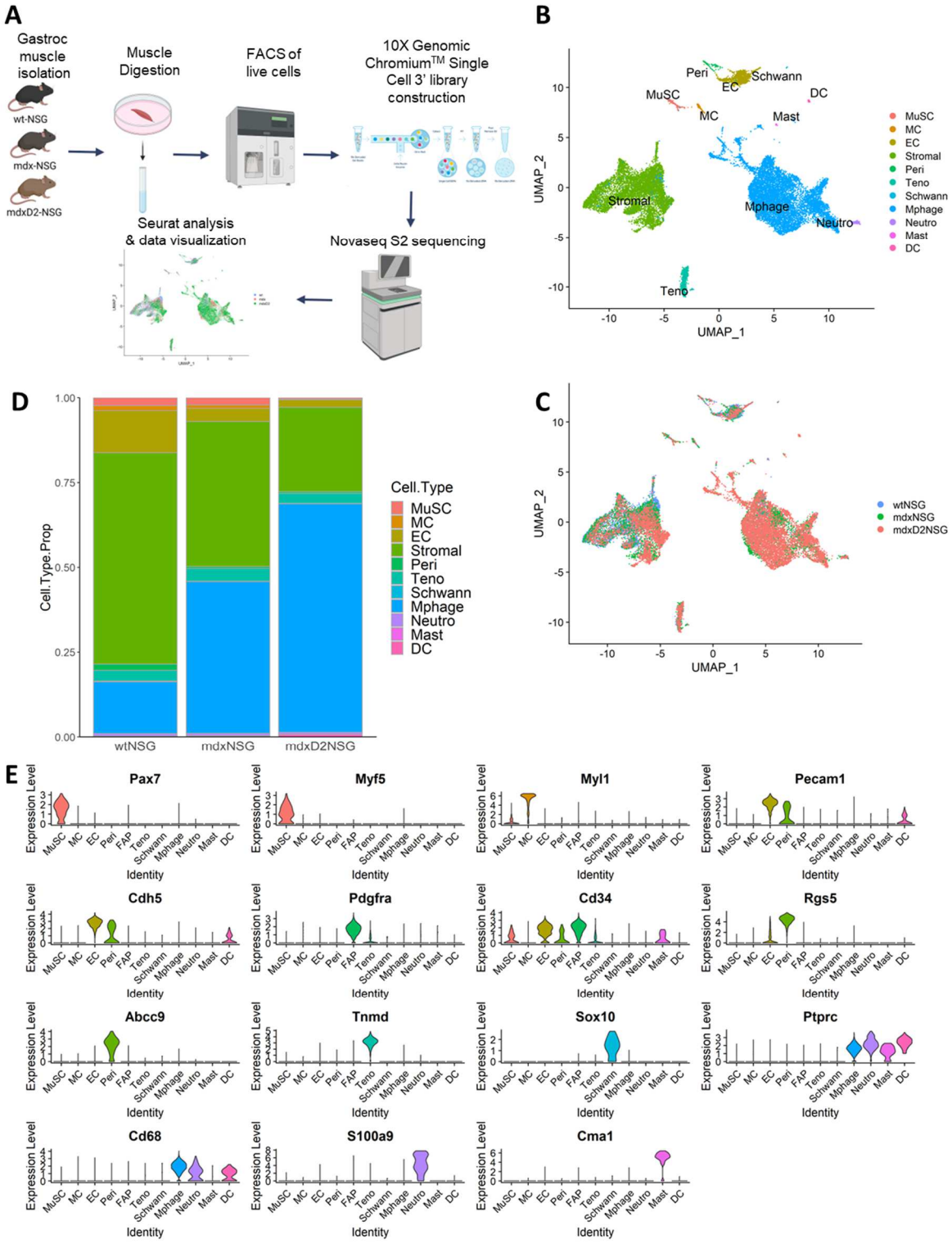

Figure 3-1: Single-Cell RNA Sequencing reveals cellular heterogeneity between healthy and dystrophic muscle states

(A) Schematic illustrating the experimental workflow for scRNA-seq with 10X genomics platform. A single cell suspension from right gastrocnemius muscles are prepared by mechanical and enzymatic dissociation followed by live cell sorting. Following library preparation, sequencing was performed on Illumina Novaseq S2 platform, and the raw data were processed by Cell Ranger (10X Genomics) to generate a gene-cell expression matrix. Metrices were then analyzed individually using Seurat and integrated using Harmony packages (n=2 replicates for each mouse model).

(B) UMAP embedding of integrated scRNA-seq data with a total of 20920 cells analyzed from wt-NSG, mdx-NSG and mdxD2-NSG gastrocnemius muscles.

(C) UMAP embedding of integrated scRNA-seq data grouped by mouse model.

(D) Relative proportion of cell populations in healthy, dystrophic and severely dystrophic gastrocnemius skeletal muscles.

(E) Violin Plot showing the main gene expression markers used to identify gastrocnemius skeletal muscle cellular composition.

MuSC: muscle satellite cells, MC: myocytes, EC: endothelial cells, Stromal: stromal cells, Peri: pericytes, Teno: tenocytes, Schwann: schwann cells, Mphage: macrophages, Neutro: neutrophils, Mast: Mast cells, DC: dendritic cells

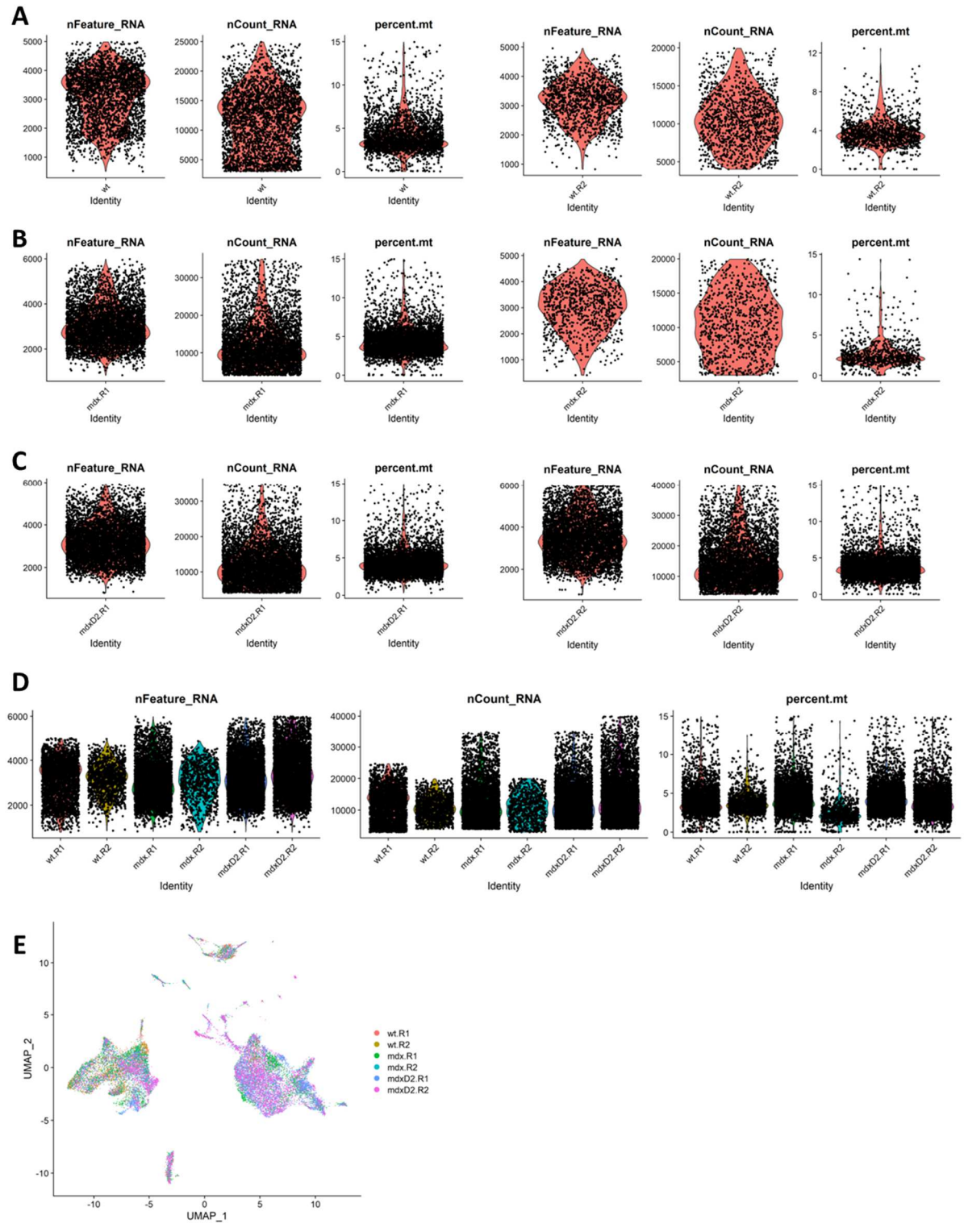

Figure 3-2: Quality control for scRNA-seq

Violin plots of analyzed samples showing the distribution of the number of genes (nFeature_RNA), number of RNA counts (nCount_RNA) and percent mitochondrial RNA (percent.mt) in (A) replicate 1 and 2 of wt-NSG gastrocnemius muscles. (B) replicate 1 and 2 of mdx-NSG gastrocnemius muscles. (C) Replicate 1 and 2 of gastrocnemius mdxD2-NSG muscles. (D) The integration of all sample replicates. (E) UMAP embedding of all muscles integrated grouped by replicates.

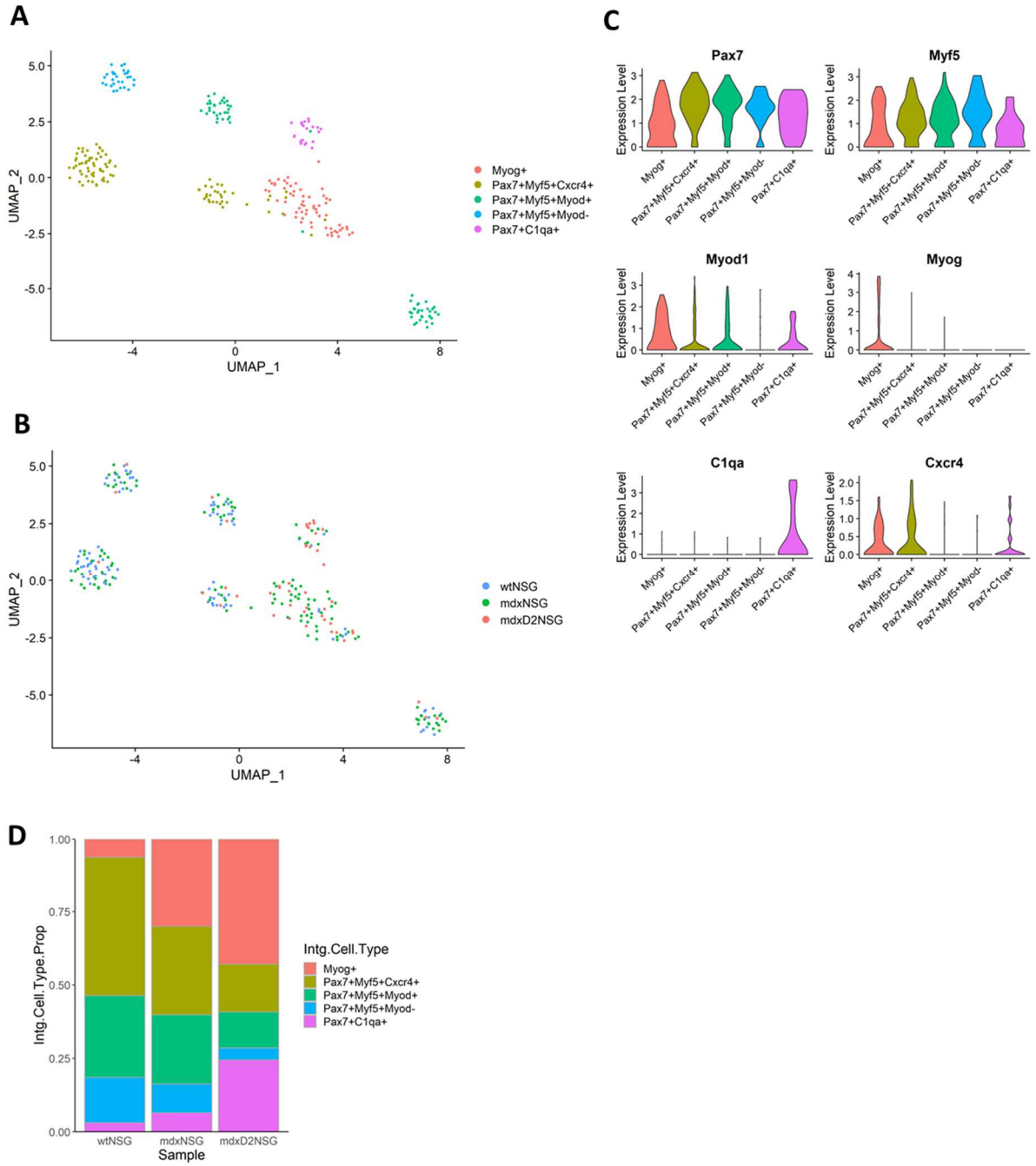

Figure 3-3: Muscle satellite cell sub-clustering reveals differences in stem cell dtates and a subpopulation with immune gene profile in mdxD2-NSG mouse model

(A) UMAP embedding of integrated muscle stem cell subpopulations in all mouse models.

(B) UMAP embedding representing mouse model contribution to integrated muscle stem cell subpopulations.

(C) Gene expression of markers used to identify the muscle stem cell subpopulations.

(D) Relative proportion of muscle stem cell subpopulations in each mouse model.

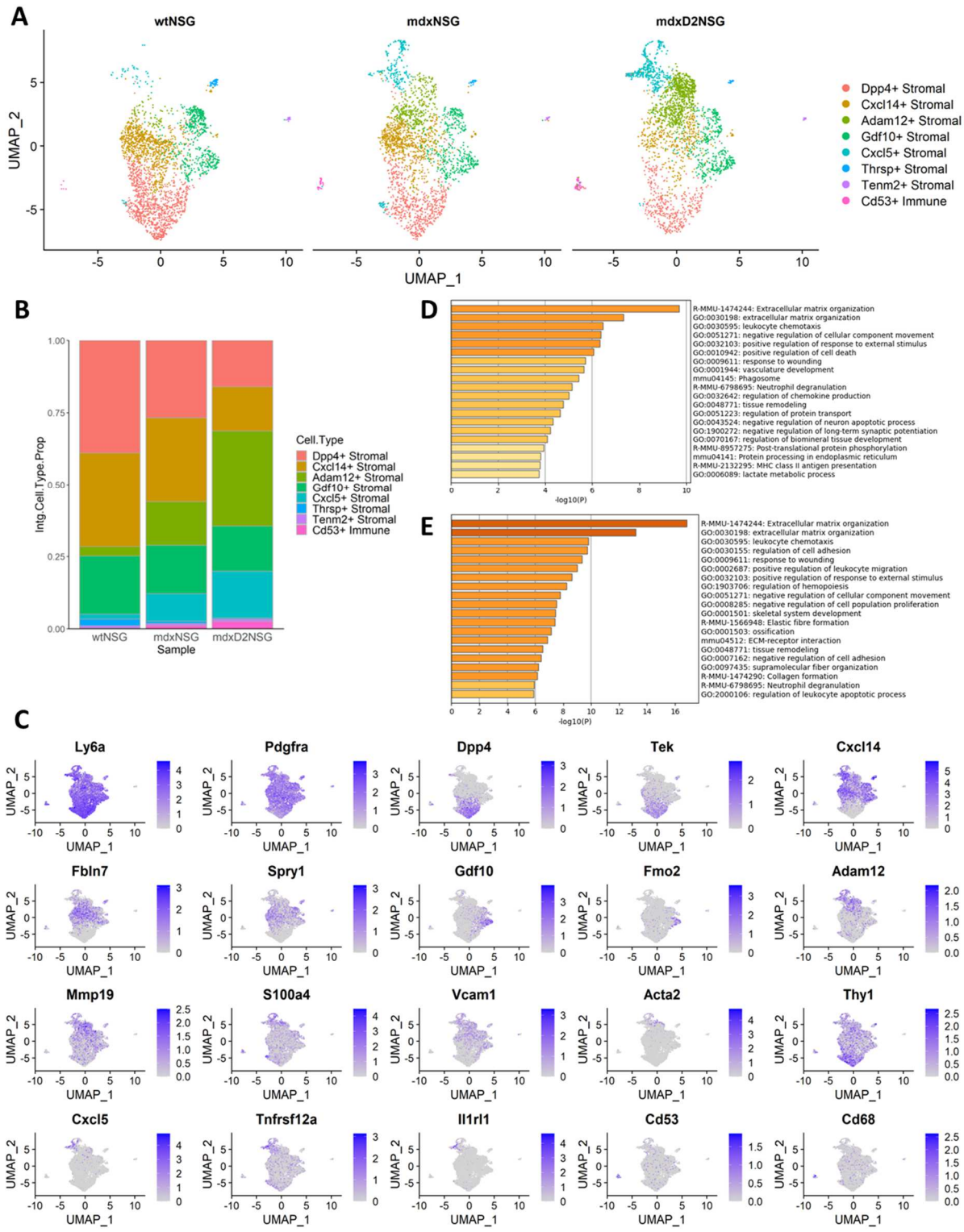

Figure 3-4: Stromal cell sub-clustering reveals stromal subtypes arising in severely dystrophic muscle

(A) UMAP of stromal cell subpopulations split by mouse model.

(B) Relative proportion of stromal cell subpopulations in healthy, dystrophic and severely dystrophic muscles.

(C) Marker gene expression used to identify stromal cell subpopulations.

(D) GO enrichment analysis of DEGs in mdxD2-NSG stromal cells versus mdx-NSG.

(E) GO enrichment analysis of DEGs in mdxD2-NSG stromal cells versus wt-NSG.

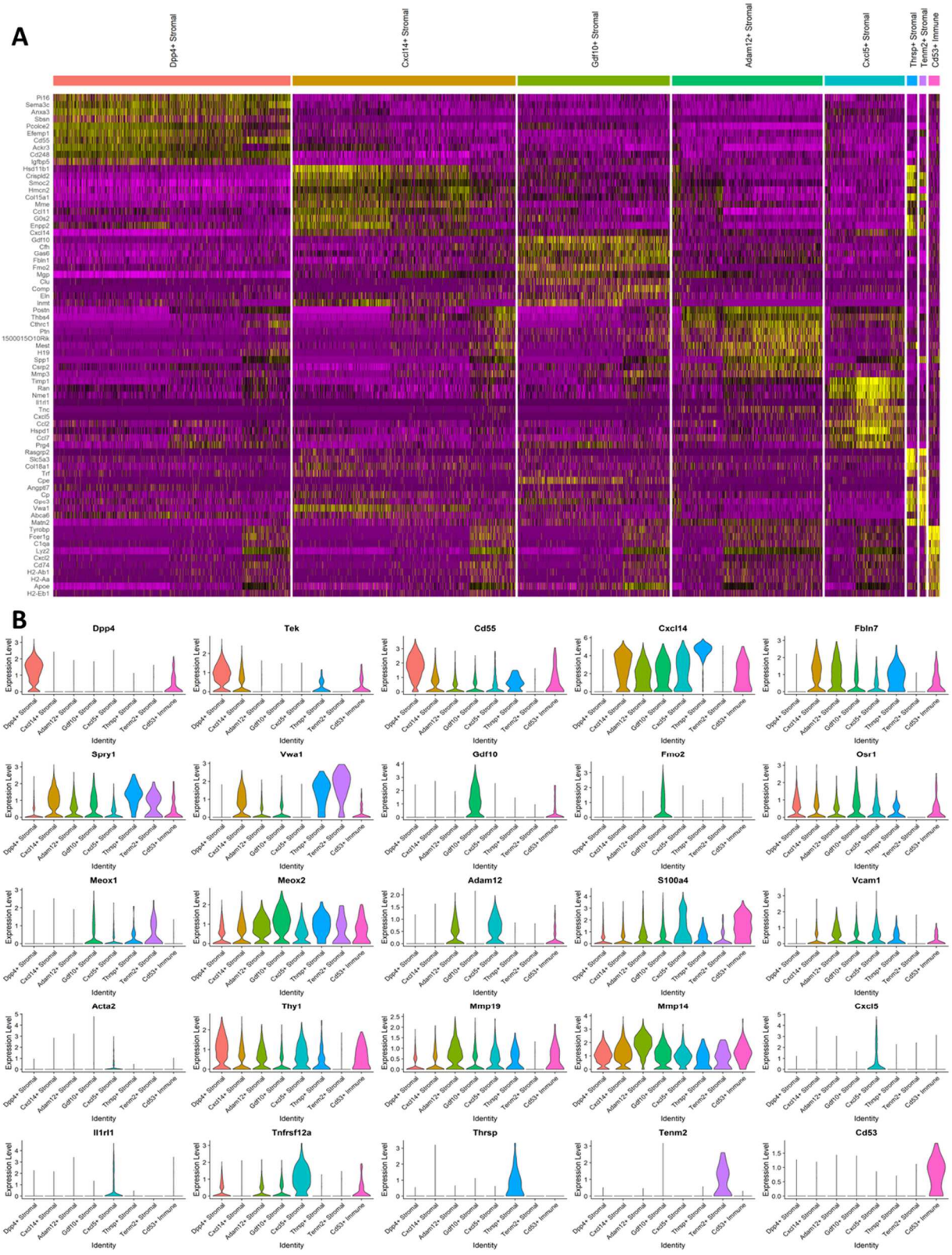

Figure 3-5: Extended gene expression profile of stromal cell subtypes

(A) Heatmap of top 10 genes expressed in each stromal cell subtype.

(B) Violin plot of an expanded panel gene expression used to identify stromal cells subtypes.

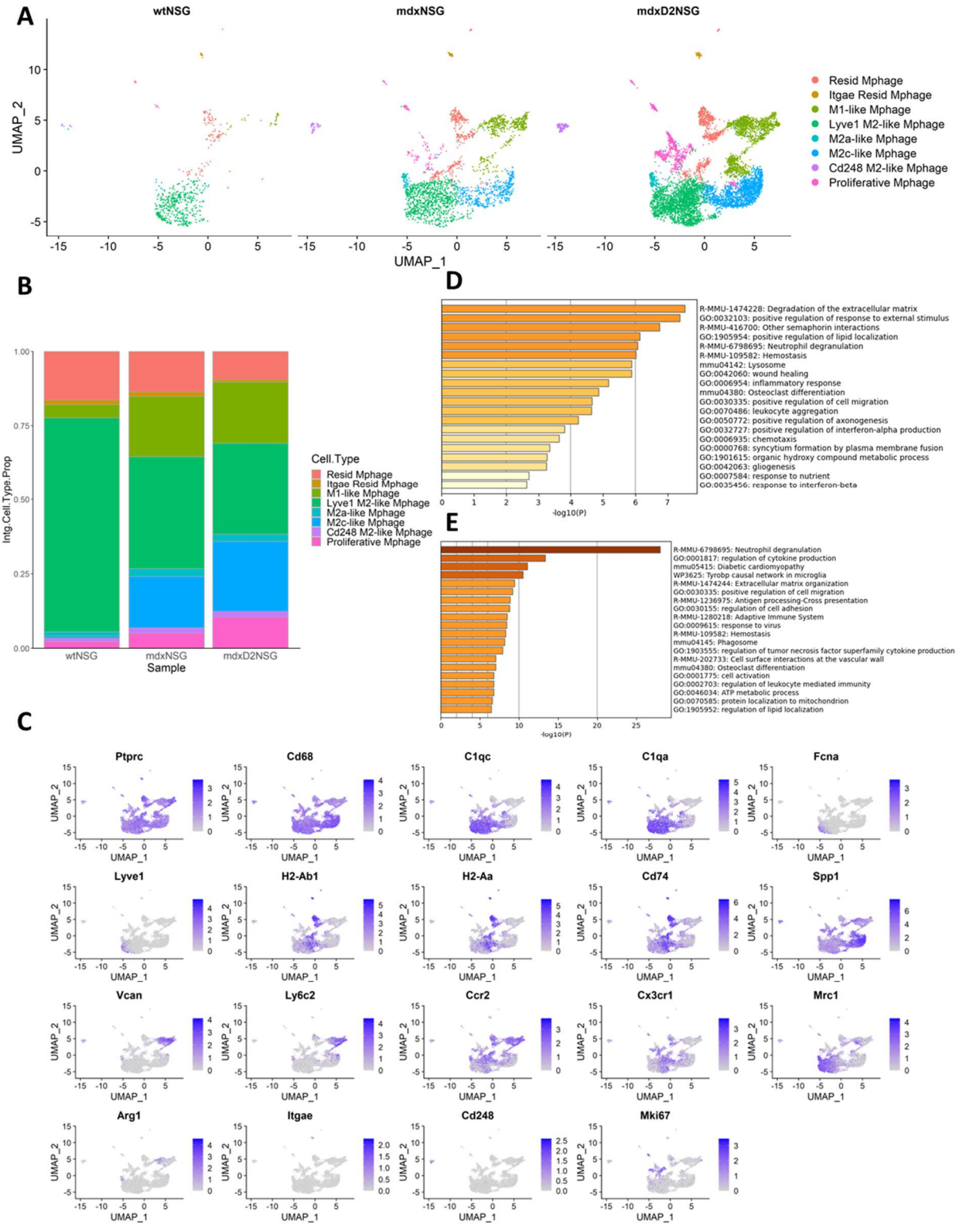
A
wtNSG
mdxNSG
mdxD2NSG
UMAP_2
UMAP_1
Resid Mphage
Itgae Resid Mphage
M1-like Mphage
Lyve1 M2-like Mphage
M2a-like Mphage
M2c-like Mphage
Cd248 M2-like Mphage
Proliferative Mphage
B
Intg.Cell.Type.Prop
Sample
wtNSG
mdxNSG
mdxD2NSG
Cell.Type
D
R-MMU-1474228: Degradation of the extracellular matrix
GO:0032103: positive regulation of response to external stimulus
R-MMU-416700: Other semaphorin interactions
GO:1905954: positive regulation of lipid localization
R-MMU-6798695: Neutrophil degranulation
R-MMU-109582: Hemostasis
mmu04142: Lysosome
GO:0042060: wound healing
GO:0006954: inflammatory response
mmu04380: Osteoclast differentiation
GO:0030335: positive regulation of cell migration
GO:0070486: leukocyte aggregation
GO:0050772: positive regulation of axonogenesis
GO:0032727: positive regulation of interferon-alpha production
GO:0006935: chemotaxis
GO:0000768: syncytium formation by plasma membrane fusion
GO:1901615: organic hydroxy compound metabolic process
GO:0042063: gliogenesis
GO:0007584: response to nutrient
GO:0035456: response to interferon-beta
-log10(P)
E
R-MMU-6798695: Neutrophil degranulation
GO:0001817: regulation of cytokine production
mmu05415: Diabetic cardiomyopathy
WP3625: Tyrobp causal network in microglia
R-MMU-1474244: Extracellular matrix organization
GO:0030335: positive regulation of cell migration
R-MMU-1236975: Antigen processing-Cross presentation
GO:0030155: regulation of cell adhesion
R-MMU-1280218: Adaptive Immune System
GO:0009615: response to virus
R-MMU-109582: Hemostasis
mmu04145: Phagosome
GO:1903555: regulation of tumor necrosis factor superfamily cytokine production
R-MMU-202733: Cell surface interactions at the vascular wall
mmu04380: Osteoclast differentiation
GO:0001775: cell activation
GO:0002703: regulation of leukocyte mediated immunity
GO:0046034: ATP metabolic process
GO:0070585: protein localization to mitochondrion
GO:1905952: regulation of lipid localization
-log10(P)
C
Ptprc
Cd68
C1qc
C1qa
Fcna
Lyve1
H2-Ab1
H2-Aa
Cd74
Spp1
Vcan
Ly6c2
Ccr2
Cx3cr1
Mrc1
Arg1
Itgae
Cd248
Mki67
UMAP_1
UMAP_2

Figure 3-6: Macrophage heterogeneity between healthy, dystrophic and severely dystrophic skeletal muscle

(A) UMAP embedding of macrophage subpopulations gastrocnemius skeletal muscle split by mouse model.

(B) Relative proportion of macrophage subpopulations cellular composition between mouse models.

(C) Gene expression panel of markers used to distinguish the different macrophage subpopulations.

(D) GO enrichment analysis of DEGs in all mdxD2-NSG macrophages versus mdx-NSG.

(E) GO enrichment analysis of DEGs in all mdxD2-NSG macrophages versus wt-NSG.

Resid Mphage = Resident macrophages

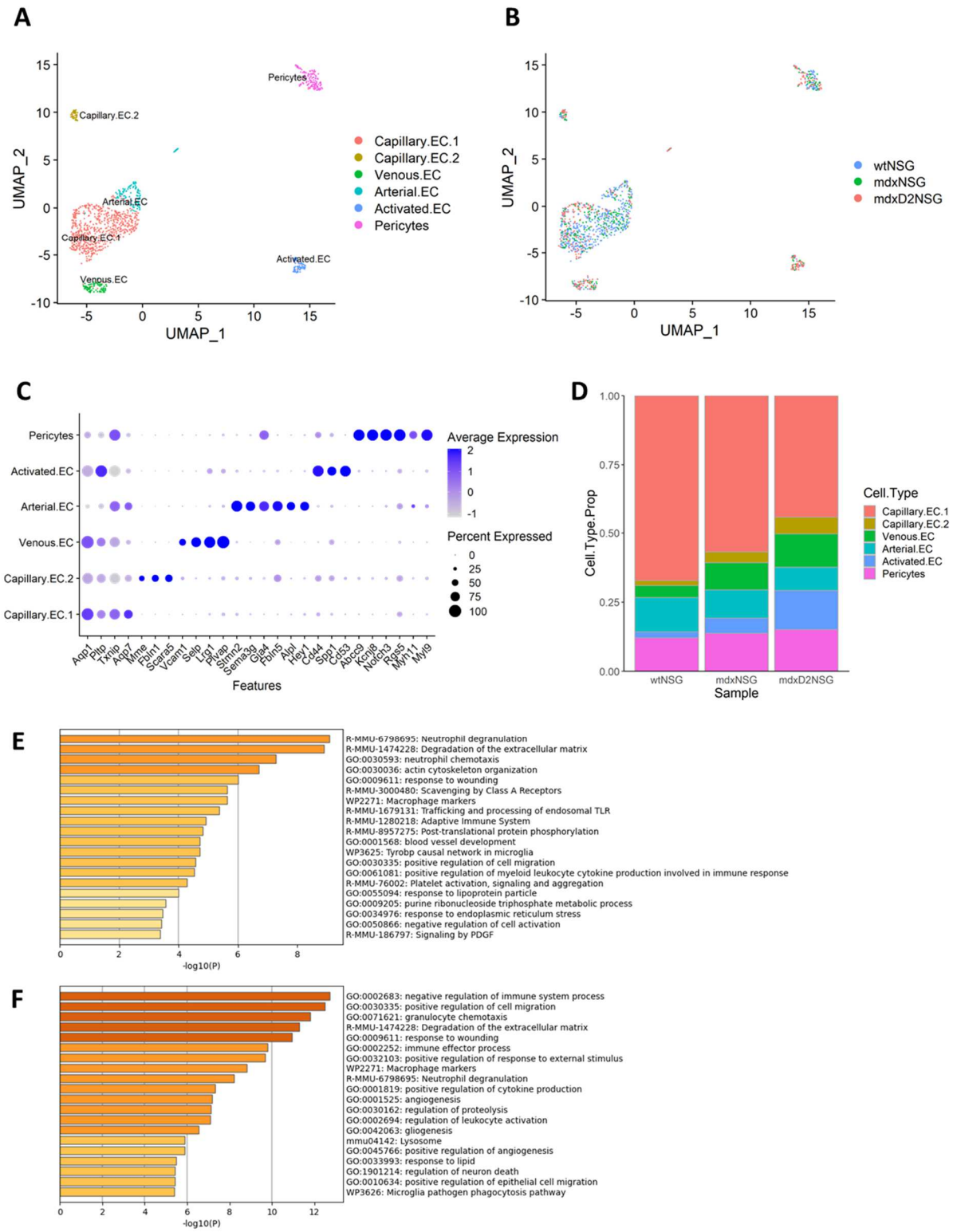

Figure 3-7: Characterization of endothelial cell subpopulations in healthy, dystrophic and severely dystrophic skeletal muscle

(A) UMAP embedding of integrated pericytes and endothelial cell subpopulations.

(B) UMAP embedding representing mouse model contribution to endothelial cell subpopulations.

(C) Dot plot of chosen genes used to identify subtypes of endothelial cells.

(D) Relative proportion of endothelial cell subpopulations identified in healthy and dystrophic muscles.

(E) GO enrichment analysis of DEGs in mdxD2-NSG endothelial cells versus mdx-NSG.

(F) GO enrichment analysis of DEGs in mdxD2-NSG endothelial cells versus wt-NSG.

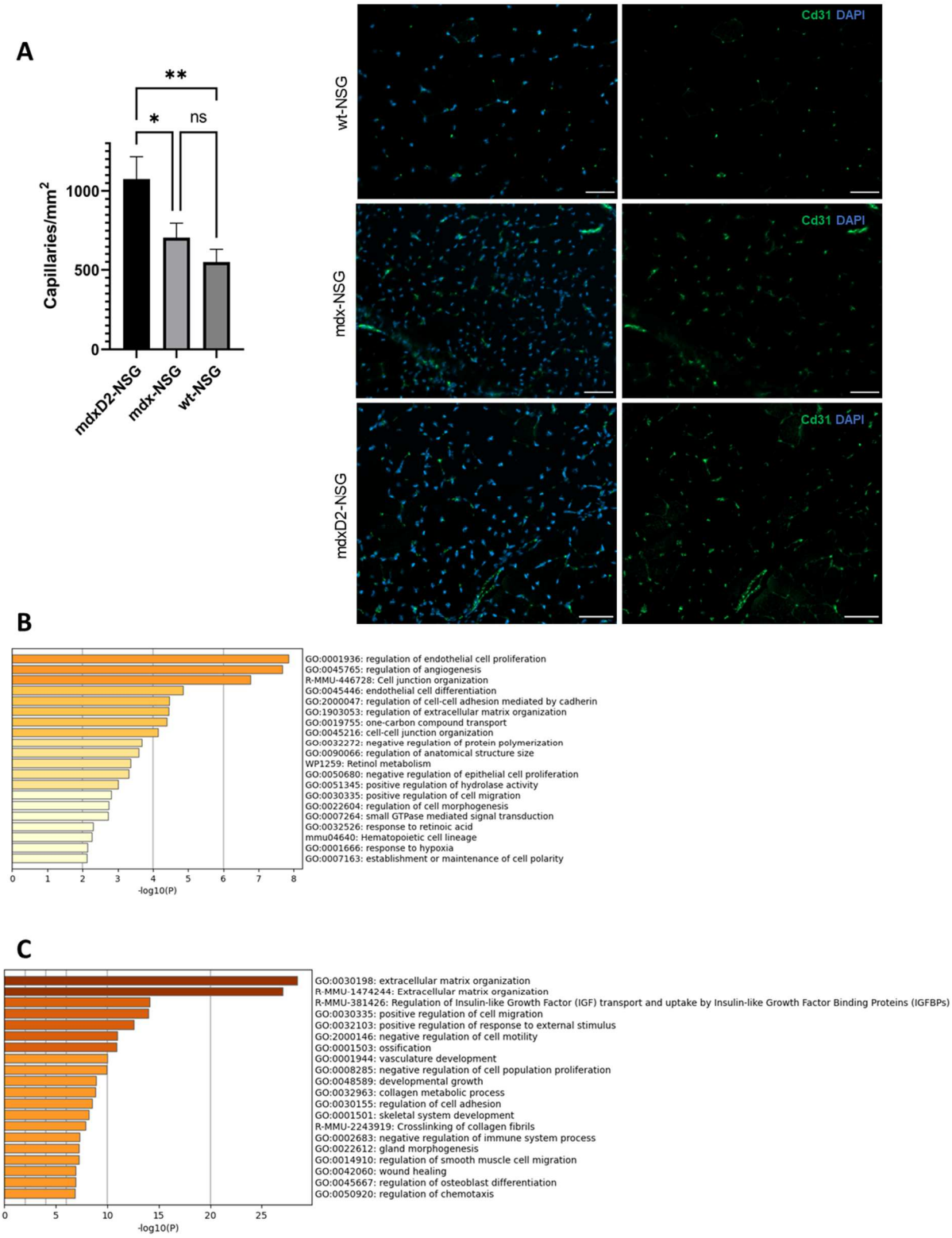

Figure 3-8: Capillary endothelial cell differences

(A) Left: capillary Density of 8 weeks gastrocnemius muscles in each mouse model. Right: IF images of representative gastrocnemius muscle cross-sections of the mouse models used for quantification, only

capillaries were counted per cross-section. Scale bar on IF images are at 20 μm. Quantification was performed using ImageJ on at least 30 images for each mouse, n=3 per mouse model. One Way-ANOVA with Tukey's multiple comparison test, error bars+SD, *P<0.05, **P<0.01

(B) GO enriched terms of DEGs in Capillary EC.1.

(C) GO enriched terms of DEGS in Capillary EC.2.

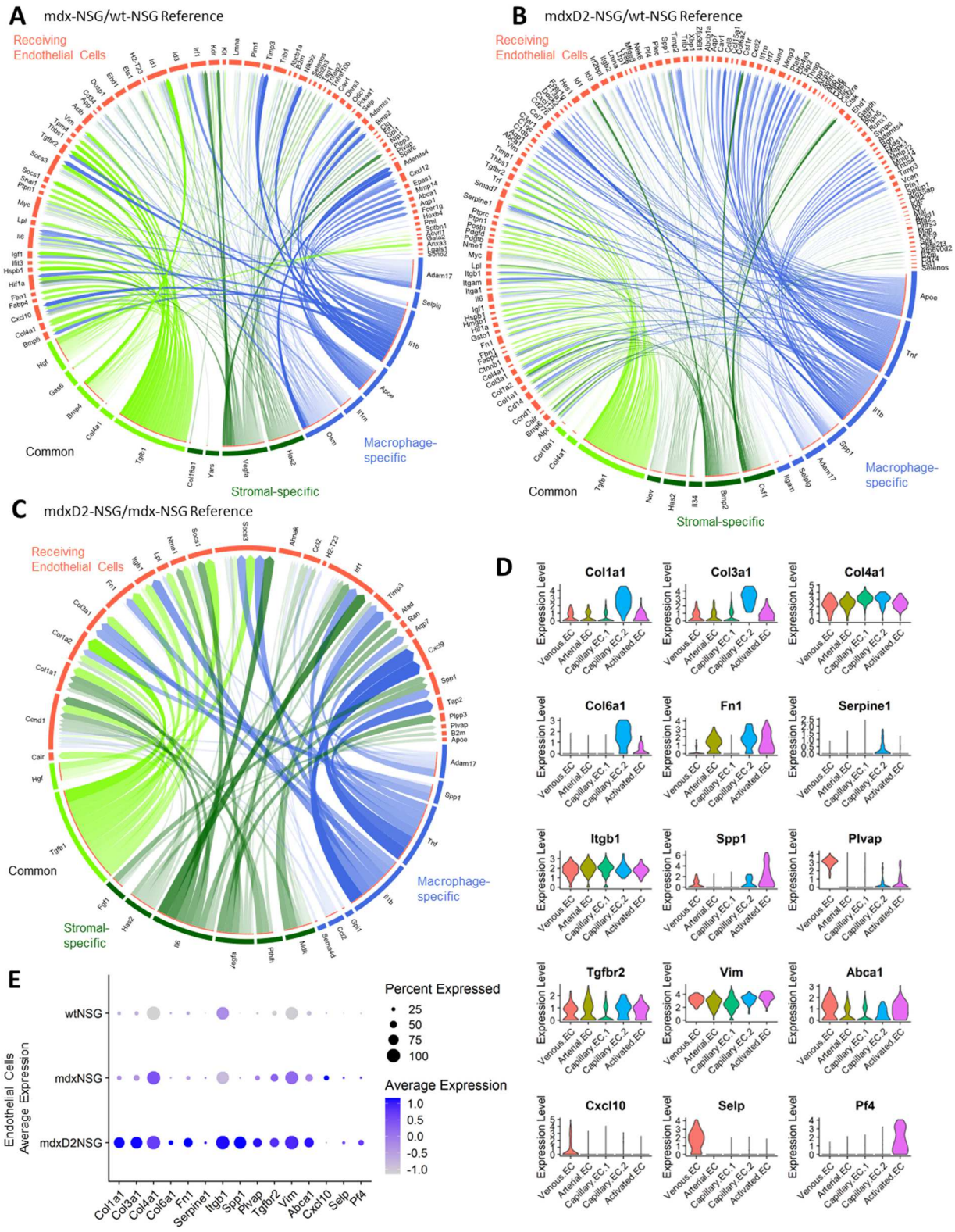

Figure 3-9: Stromal cells and macrophages released ligands and their regulated target genes on endothelial cells in dystrophic and severely dystrophic environment

Circos plot of NicheNet analysis showing links of cell-cell interactions between predicted ligands from stromal cells and macrophages with most likely regulated target genes that are differentially expressed on (A) mdx-NSG endothelial cells, wt-NSG as a reference (B) mdxD2-NSG endothelial cells, wt-NSG as a reference, and (C) mdxD2-NSG endothelial cells, wt-NSG as a reference. Degree of transparency is determined by the regulatory potential value of a ligand-target interaction (Blue: macrophage-specific ligands, Green: stromal cell-specific ligands, Lawn green = common ligands released from both stromal cells and macrophages). (D) Violin plots of some genes of interest that were differentially expressed in the dystrophic endothelial cells identified by NicheNet analysis. (E) Dot plot of average expression between the mouse models of some genes of interest that were differentially expressed in the dystrophic endothelial cells identified by NicheNet analysis.

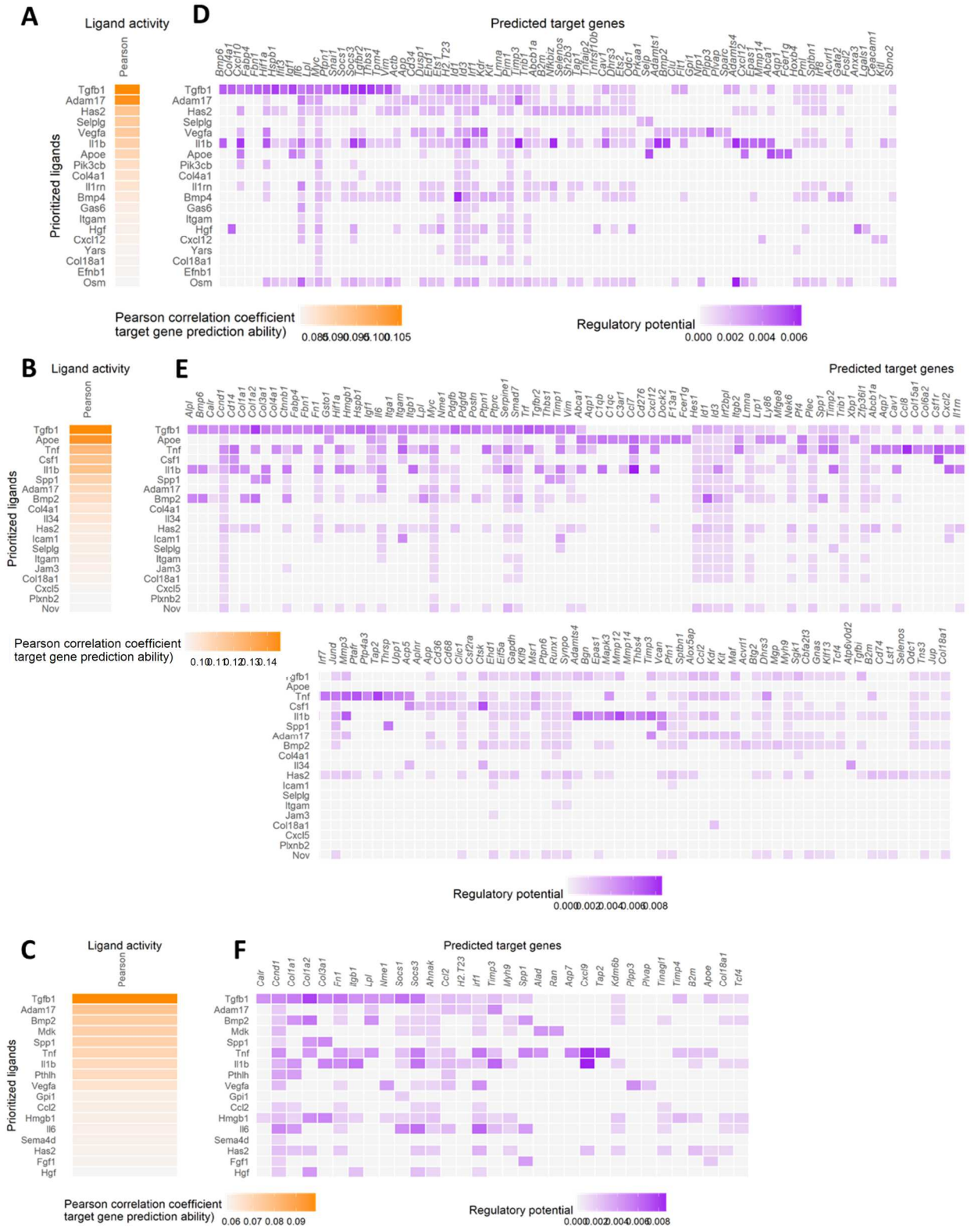
A
Ligand activity
Pearson
Prioritized ligands
Tgfb1
Adam17
Has2
Selplg
Vegfa
Il1b
Apoe
Pik3cb
Col4a1
Il1rn
Bmp4
Gas6
Itgam
Hgf
Cxcl12
Yars
Col18a1
Efnb1
Osm
D
Predicted target genes
Pearson correlation coefficient
target gene prediction ability)
0.085 0.090 0.095 0.100 0.105
Regulatory potential
0.000 0.002 0.004 0.006
B
Ligand activity
Pearson
Prioritized ligands
Tgfb1
Apoe
Tnf
Csf1
Il1b
Spp1
Adam17
Bmp2
Col4a1
Il34
Has2
Icam1
Selplg
Itgam
Jam3
Col18a1
Cxcl5
Plxnb2
Nov
E
Predicted target genes
Pearson correlation coefficient
target gene prediction ability)
0.10 0.11 0.12 0.13 0.14
Regulatory potential
0.000 0.002 0.004 0.006 0.008
C
Ligand activity
Pearson
Prioritized ligands
Tgfb1
Adam17
Bmp2
Mdk
Spp1
Tnf
Il1b
Pthlh
Vegfa
Gpi1
Ccl2
Hmgb1
Il6
Sema4d
Has2
Fgf1
Hgf
F
Predicted target genes
Pearson correlation coefficient
target gene prediction ability)
0.06 0.07 0.08 0.09
Regulatory potential
0.000 0.002 0.004 0.006 0.008

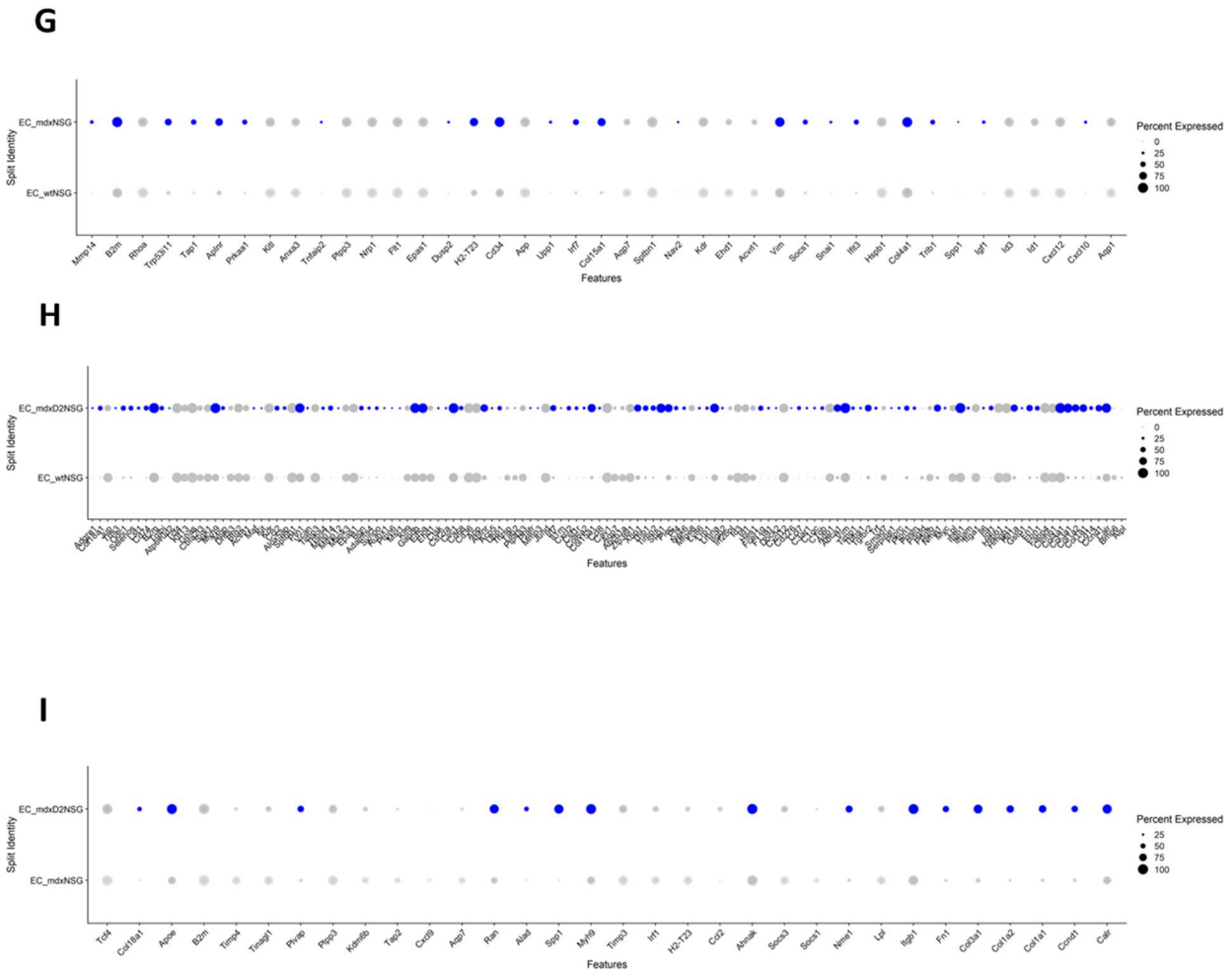

Figure 3-10: Outcome of NicheNet's ligand activity prediction released from stromal cells and macrophages in dystrophic muscle and their target gene expression regulated on EC

Outcome of NicheNet's ligand activity prediction of stromal cells and macrophages in (A) mdx-NSG (wt-NSG as reference). (B) mdxD2-NSG (wt-NSG as reference) and (C) mdxD2-NSG (mdx-NSG as reference). Pearson correlation coefficient was used between prior regulatory potential scores and endothelial cell gene set assignments. Pearson correlation indicates the ability of each ligand to predict the endothelial cell (EC) target gene, therefore better predictive ligands are ranked higher.

NicheNet's ligand-target matrix denoting the regulatory potential between predicted released ligands and target gene from EC in (D) mdx-NSG ECs and (E) mdxD2-NSG ECs (F) mdxD2-NSG ECs (mdx-NSG as reference).

(G) Dot plot showing the average expression of NicheNet's predicted target genes on ECs in wt-NSG and mdx-NSG. (H) Dot plot showing the average expression of NicheNet's predicted target genes on ECs in wt-NSG and mdxD2-NSG. (I) Dot plot showing the average expression of NicheNet's predicted target genes on ECs in mdxD2- NSG and mdx-NSG

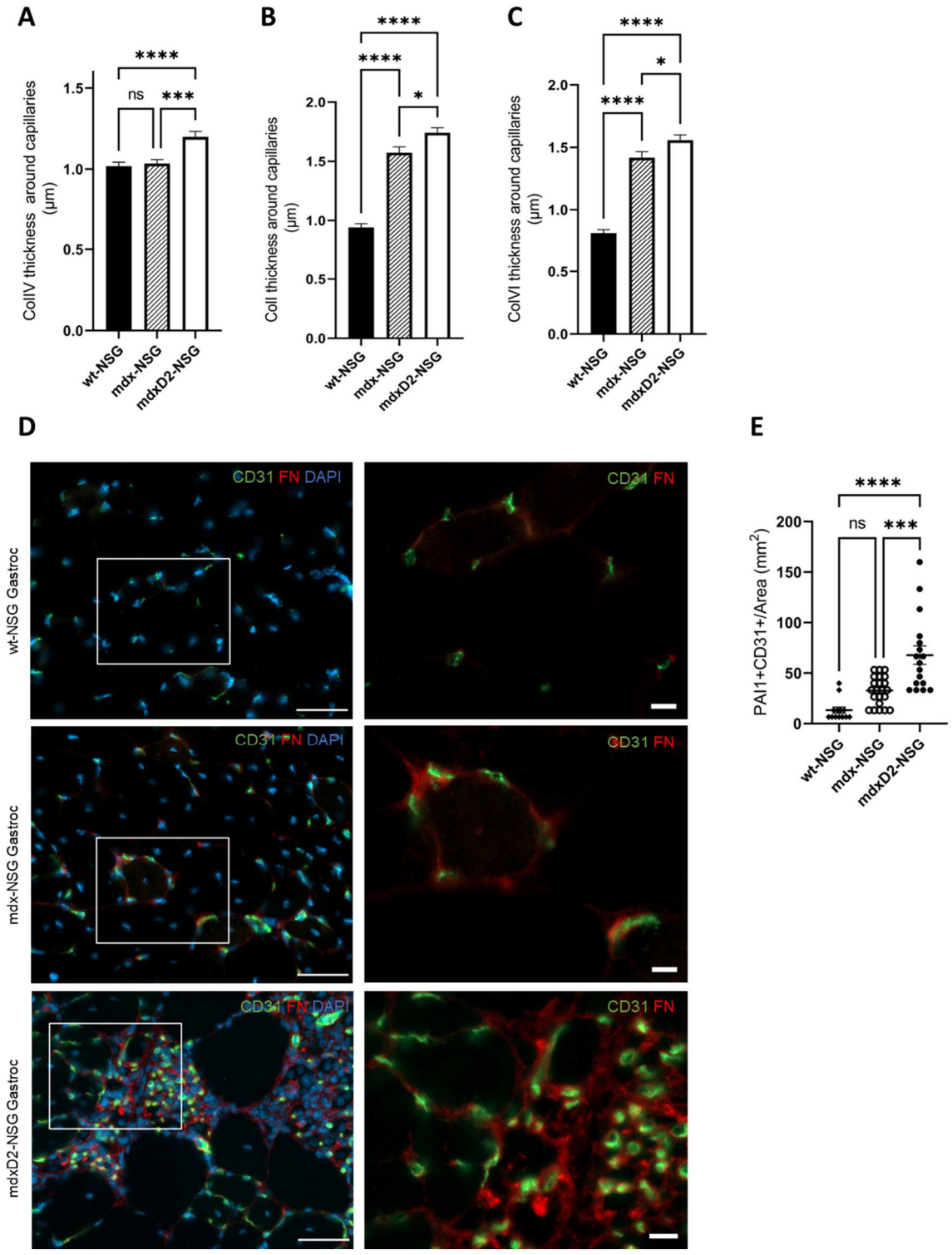

Figure 3-11: Dystrophic and severely dystrophic endothelial cells have increased ECM deposition

Quantification of (A) Collagen type IV (COLIV), (B) Collagen I (COLI), (C) Collagen VI (COL VI) deposition around capillary endothelial cells in healthy and DMD muscles. One Way ANOVA with

Tukey's multiple comparison test (error bars show mean+SEM *P <0.05, ***$P \leq 0.0001$, ****$P <$ 0.0001). (D) Immunofluorescence staining of gastrocnemius muscle cross-sections for endothelial cell (CD31, green), and fibronectin (FN, red) and nuclear markers (DAPI, blue). Left column scale bar at 50 µm, right column are magnified images of boxed, scale bar at 10 µm. (E) Quantification of PAI-1 and CD31 colocalization in gastrocnemius muscle cross-sections across the mouse models. One way-ANOVA with Tukey's multiple comparisons test (error bars show mean±SEM ***$P \leq 0.001$, ****P<0.0001).

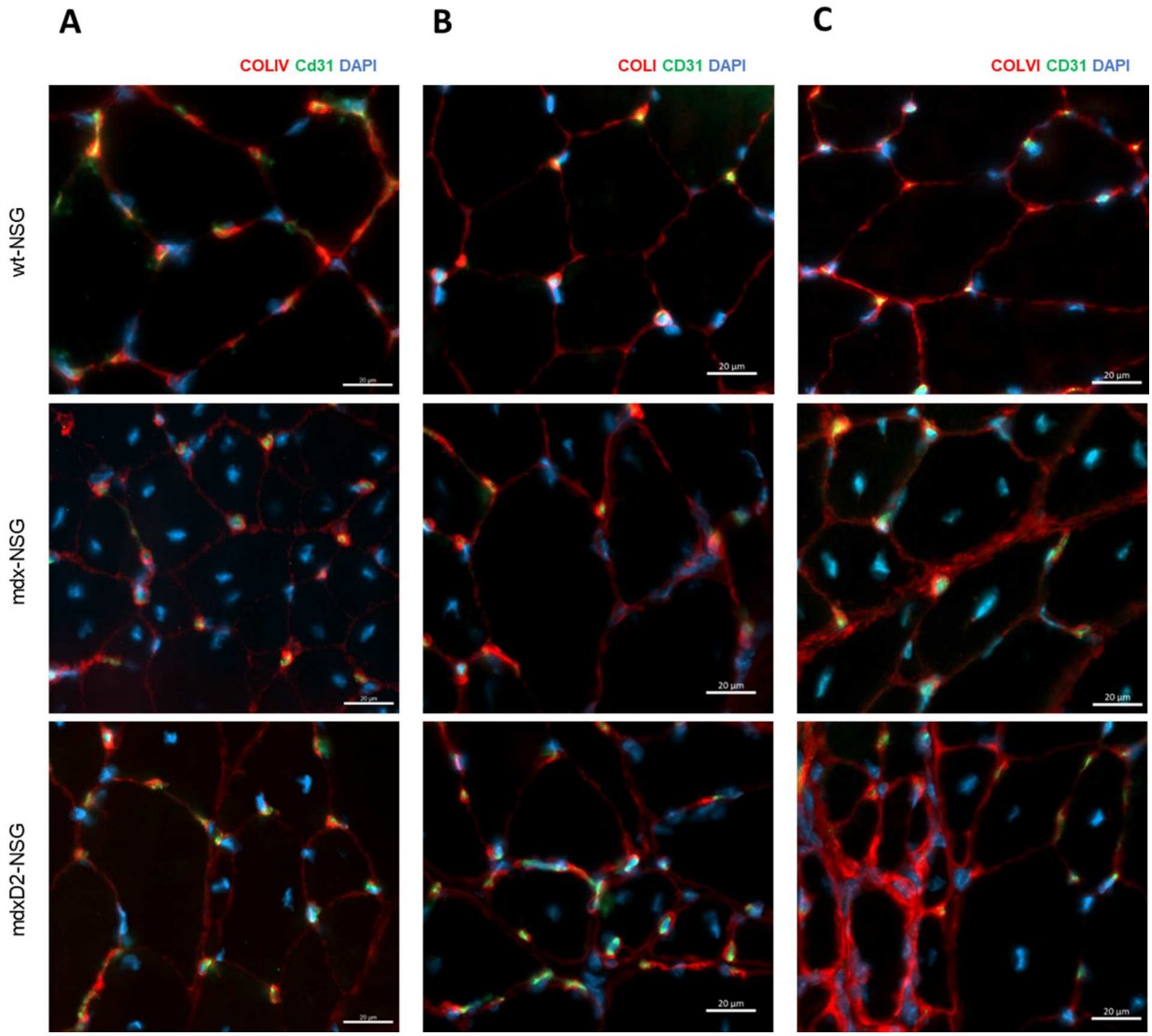

Figure 3-12: ECM protein staining in wt-NSG, mdx-NSG and mdxD2-NSG of gastrocnemius muscle cross sections

Immunofluorescence staining of gastrocnemius muscle cross-sections for vasculature (CD31, green), and nuclear marker (DAPI, blue) and column (A) collagen type IV (COLIV, red), (B) collagen type I (COLI, red), (C) Collagen type VI (COLVI, red) (Scale bar at 20 µm).

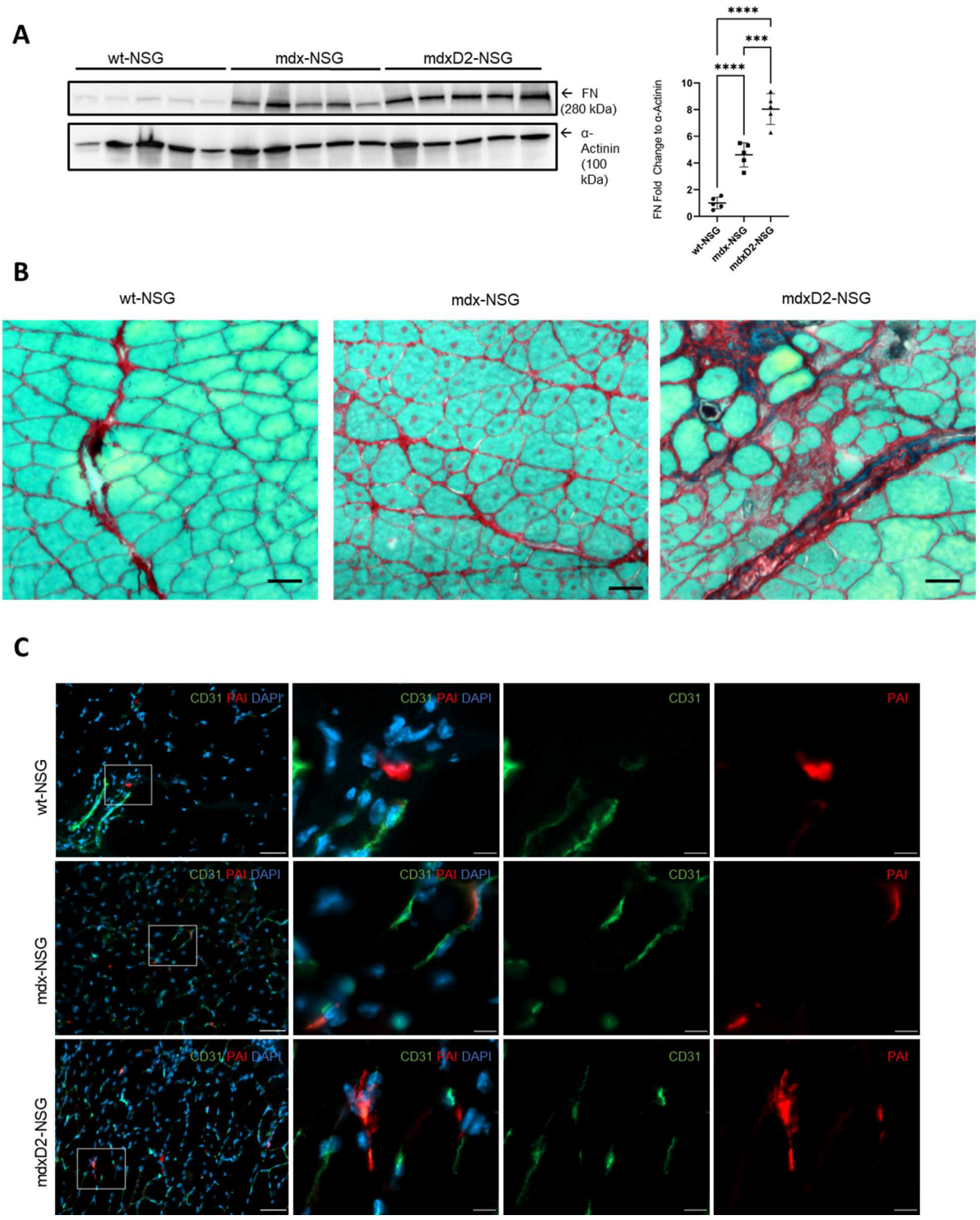

Figure 3-13: Validation of fibronectin and plasminogen activator inhibotr-1 upregulation in severely dystrophic gastrocnemius muscle

(A) Fibronectin (FN) expression analysis by Western Blotting in whole muscle lysates of healthy, dystrophic and severely dystrophic muscles (graph show individual data points of fold change to α-

Actinin, One way ANOVA with Tukey's multiple comparisons, mean±SD. ***$P \leq 0.001$, ****$P < 0.001$)

(B) Sirius red stained gastrocnemius skeletal muscle cross-sections of healthy, dystrophic and severely dystrophic mouse models (Scale bar at 50 μm).

(C) Immunofluorescence staining for plasminogen activator inhibitor-1 (PAI-1) and CD31 colocalization of gastrocnemius skeletal muscles across the mouse models.

Table 3-2: Cell counts per mouse model

Sample	Cell subpopulation	Cell Number	Proportion
wtNSG	MuSC	97	2.320574
wtNSG	MC	62	1.483254
wtNSG	EC	519	12.41627
wtNSG	Stromal	2604	62.29665
wtNSG	Peri	78	1.866029
wtNSG	Teno	130	3.110048
wtNSG	Schwann	10	0.239234
wtNSG	Mphage	639	15.28708
wtNSG	Neutro	30	0.717703
wtNSG	Mast	11	0.263158
mdxNSG	MuSC	123	2.149222
mdxNSG	MC	57	0.995981
mdxNSG	EC	222	3.879084
mdxNSG	Stromal	2446	42.73982
mdxNSG	Peri	33	0.576621
mdxNSG	Teno	216	3.774244
mdxNSG	Schwann	5	0.087367
mdxNSG	Mphage	2560	44.73178
mdxNSG	Neutro	38	0.663987
mdxNSG	Mast	10	0.174734
mdxNSG	DC	13	0.227154
mdxD2NSG	MuSC	49	0.444767
mdxD2NSG	MC	16	0.14523
mdxD2NSG	EC	249	2.260143
mdxD2NSG	Stromal	2738	24.8525
mdxD2NSG	Peri	49	0.444767
mdxD2NSG	Teno	330	2.995371
mdxD2NSG	Schwann	10	0.090769
mdxD2NSG	Mphage	7426	67.40492
mdxD2NSG	Neutro	64	0.58092
mdxD2NSG	Mast	6	0.054461
mdxD2NSG	DC	80	0.72615

Table 3-2: Top 20 genes expressed in each muscle cell population Cluster

p_val	p_val_adj	avg_logFC	pct.1	pct.2	pct.diff	cluster	gene
0	0	2.087254	0.569	0.006	0.563	MuSC	*Gal*
0	0	1.994018	0.807	0.024	0.783	MuSC	*Chodl*
0	0	1.837388	0.944	0.096	0.848	MuSC	*Des*
0	0	1.778041	0.862	0.002	0.86	MuSC	*Pax7*
0	0	1.632942	0.48	0.027	0.453	MuSC	*Nppc*
0	0	1.413237	0.747	0.001	0.746	MuSC	*Myf5*
0	0	1.35393	0.803	0.002	0.801	MuSC	*Fgfr4*
0	0	1.336328	0.866	0.11	0.756	MuSC	*Ncam1*
0	0	1.247071	0.803	0.003	0.8	MuSC	*Cdh15*
0	0	1.227649	0.621	0.007	0.614	MuSC	*Asb5*
0	0	1.182947	0.654	0.03	0.624	MuSC	*Heyl*
0	0	1.113891	0.621	0.041	0.58	MuSC	*Clmn*
0	0	1.112344	0.725	0.029	0.696	MuSC	*Notch3*
0	0	1.106231	0.461	0.002	0.459	MuSC	*Erfe*
0	0	1.10508	0.524	0.001	0.523	MuSC	*Chrdl2*
0	0	1.093793	0.717	0.08	0.637	MuSC	*Sytl2*
0	0	1.009846	0.424	0.004	0.42	MuSC	*Ankrd1*
0	0	0.925271	0.349	0.003	0.346	MuSC	*Myod1*
0	0	0.8987	0.58	0.003	0.577	MuSC	*Chrna1*
0	0	0.863802	0.528	0.009	0.519	MuSC	*Prox1*
0	0	4.004987	0.807	0.032	0.775	MC	*Pvalb*
0	0	3.835723	0.933	0.074	0.859	MC	*Eno3*
0	0	3.535134	0.926	0.022	0.904	MC	*Pgam2*
0	0	3.494085	0.933	0.024	0.909	MC	*Tcap*
0	0	3.445538	0.911	0.025	0.886	MC	*Myoz1*
0	0	3.14889	0.793	0.039	0.754	MC	*Actn3*
0	0	3.13944	0.933	0.043	0.89	MC	*Atp2a1*
0	0	3.087627	0.659	0.02	0.639	MC	*Mb*
0	0	3.072949	0.911	0.041	0.87	MC	*Cox6a2*
0	0	3.066165	0.911	0.032	0.879	MC	*Cox8b*
0	0	2.981615	0.822	0.015	0.807	MC	*Car3*
0	0	2.747432	0.681	0.032	0.649	MC	*Myh4*
0	0	2.257539	0.541	0.01	0.531	MC	*Actc1*
0	0	2.2402	0.719	0.013	0.706	MC	*Mybpc2*
0	0	2.160849	0.815	0.046	0.769	MC	*Pygm*
0	0	2.123959	0.859	0.014	0.845	MC	*Sh3bgr*
0	0	2.035805	0.852	0.005	0.847	MC	*Smpx*
0	0	2.017449	0.815	0.005	0.81	MC	*Apobec2*
0	0	1.955044	0.844	0.017	0.827	MC	*Rpl3l*
0	0	1.918742	0.852	0.01	0.842	MC	*Eef1a2*

0	0	4.67246	0.998	0.169	0.829	EC	*Fabp4*
0	0	3.450905	0.869	0.058	0.811	EC	*Aqp1*
0	0	2.874778	0.953	0.017	0.936	EC	*Gpihbp1*
0	0	2.816982	0.996	0.026	0.97	EC	*Cdh5*
0	0	2.800582	0.982	0.029	0.953	EC	*Flt1*
0	0	2.71544	0.98	0.113	0.867	EC	*Cavin2*
0	0	2.662642	0.993	0.036	0.957	EC	*Egfl7*
0	0	2.594639	0.997	0.288	0.709	EC	*Cav1*
0	0	2.535362	0.973	0.015	0.958	EC	*Ptprb*
0	0	2.525736	0.896	0.047	0.849	EC	*Ctla2a*
0	0	2.471541	0.989	0.032	0.957	EC	*Pecam1*
0	0	2.454838	0.83	0.014	0.816	EC	*Cldn5*
0	0	2.393962	0.891	0.021	0.87	EC	*Tcf15*
0	0	2.356841	0.971	0.015	0.956	EC	*Adgrf5*
0	0	2.34662	0.991	0.305	0.686	EC	*Cd36*
0	0	2.311033	0.974	0.142	0.832	EC	*Mgll*
0	0	2.308028	0.831	0.133	0.698	EC	*Id1*
0	0	2.254094	0.933	0.032	0.901	EC	*Kdr*
0	0	2.250066	0.986	0.446	0.54	EC	*Gng11*
0	0	2.185818	0.937	0.107	0.83	EC	*Tspan13*
0	0	3.05557	1	0.731	0.269	Stromal	*Col3a1*
0	0	2.653351	1	0.53	0.47	Stromal	*Dcn*
0	0	2.600467	0.931	0.106	0.825	Stromal	*Clec3b*
0	0	2.59767	0.99	0.197	0.793	Stromal	*Mfap5*
0	0	2.447856	0.987	0.258	0.729	Stromal	*Fbn1*
0	0	2.36756	0.998	0.239	0.759	Stromal	*Serping1*
0	0	2.342741	0.66	0.051	0.609	Stromal	*Myoc*
0	0	2.338409	0.811	0.084	0.727	Stromal	*Smoc2*
0	0	2.303839	0.671	0.368	0.303	Stromal	*Cxcl14*
0	0	2.25583	0.996	0.278	0.718	Stromal	*Fstl1*
0	0	2.254516	0.994	0.208	0.786	Stromal	*Nid1*
0	0	2.241293	0.944	0.175	0.769	Stromal	*Lum*
0	0	2.220012	0.98	0.156	0.824	Stromal	*Dpt*
0	0	2.14752	0.938	0.182	0.756	Stromal	*Meg3*
0	0	2.109978	0.633	0.136	0.497	Stromal	*Pi16*
0	0	2.054631	0.906	0.104	0.802	Stromal	*Tnxb*
0	0	2.04018	0.969	0.228	0.741	Stromal	*Igfbp6*
0	0	2.036787	0.994	0.247	0.747	Stromal	*Col5a2*
0	0	2.027391	0.976	0.197	0.779	Stromal	*Col6a3*
0	0	2.007719	0.742	0.04	0.702	Stromal	*Ccl11*
0	0	4.300499	0.994	0.034	0.96	Peri	*Rgs5*
0	0	2.780083	0.881	0.013	0.868	Peri	*Kcnj8*
0	0	2.542324	0.881	0.024	0.857	Peri	*Abcc9*

0	0	2.082793	0.919	0.086	0.833	Peri	*Art3*
0	0	2.054162	0.881	0.033	0.848	Peri	*Gm13889*
0	0	2.045709	0.969	0.031	0.938	Peri	*Notch3*
0	0	2.026312	0.944	0.025	0.919	Peri	*Gucy1a1*
0	0	1.946113	0.888	0.003	0.885	Peri	*Higd1b*
0	0	1.907523	0.925	0.008	0.917	Peri	*Cox4i2*
0	0	1.901101	0.7	0.006	0.694	Peri	*Myh11*
0	0	1.836726	0.944	0.033	0.911	Peri	*Gucy1b1*
0	0	1.782874	0.925	0.092	0.833	Peri	*Mylk*
0	0	1.756487	0.856	0.01	0.846	Peri	*Rgs4*
0	0	1.732931	0.931	0.044	0.887	Peri	*Tinagl1*
0	0	1.58353	0.881	0.038	0.843	Peri	*Ppp1r14a*
0	0	1.583368	0.719	0.005	0.714	Peri	*Casq2*
0	0	1.514195	0.781	0.036	0.745	Peri	*Rasl11a*
0	0	1.500548	0.888	0.054	0.834	Peri	*Cpe*
0	0	1.444496	0.8	0.008	0.792	Peri	*Gja4*
0	0	1.42616	0.888	0.055	0.833	Peri	*Esam*
0	0	4.529303	0.997	0.066	0.931	Teno	*Fmod*
0	0	3.263175	0.984	0.029	0.955	Teno	*Tnmd*
0	0	3.119834	1	0.307	0.693	Teno	*Thbs4*
0	0	2.978802	0.864	0.077	0.787	Teno	*Comp*
0	0	2.769838	0.661	0.046	0.615	Teno	*Angptl7*
0	0	2.768182	0.741	0.009	0.732	Teno	*Chad*
0	0	2.723459	0.93	0.011	0.919	Teno	*Cilp2*
0	0	2.708079	0.849	0.085	0.764	Teno	*1500015O10Rik*
0	0	2.672087	0.895	0.012	0.883	Teno	*Kera*
0	0	2.455316	0.985	0.029	0.956	Teno	*Col11a1*
0	0	2.370109	0.987	0.404	0.583	Teno	*Abi3bp*
0	0	2.2104	0.991	0.436	0.555	Teno	*Mgp*
0	0	2.198296	1	0.743	0.257	Teno	*Col1a1*
0	0	2.093234	1	0.749	0.251	Teno	*Col1a2*
0	0	2.066338	0.91	0.133	0.777	Teno	*Cpxm2*
0	0	2.036615	0.96	0.211	0.749	Teno	*Mfap4*
0	0	1.972886	1	0.484	0.516	Teno	*Serpinf1*
0	0	1.956016	0.981	0.151	0.83	Teno	*Col12a1*
0	0	1.825808	0.87	0.013	0.857	Teno	*Scx*
0	0	1.720561	1	0.747	0.253	Teno	*Sparc*
0	0	2.762875	0.88	0.001	0.879	Schwann	*Kcna1*
0	0	2.635039	0.64	0.001	0.639	Schwann	*Mal*
0	0	2.583424	1	0.009	0.991	Schwann	*Plp1*
0	0	2.062326	0.6	0.003	0.597	Schwann	*Fxyd3*
0	0	1.824527	0.72	0.001	0.719	Schwann	*Gjc3*

0	0	1.771797	0.72	0.001	0.719	Schwann	*Sfrp5*
0	0	1.754858	0.84	0.008	0.832	Schwann	*Cadm4*
0	0	1.648794	0.64	0	0.64	Schwann	*Gpr37l1*
0	0	1.63077	0.8	0	0.8	Schwann	*Sox10*
0	0	1.616546	0.8	0.008	0.792	Schwann	*Plekhb1*
0	0	1.597798	0.36	0.001	0.359	Schwann	*Cldn19*
0	0	1.561583	0.56	0.004	0.556	Schwann	*Ptprz1*
0	0	1.488221	0.68	0	0.68	Schwann	*Foxd3*
0	0	1.326907	0.48	0	0.48	Schwann	*Sostdc1*
0	0	1.293462	0.48	0.003	0.477	Schwann	*Reln*
0	0	1.162376	0.28	0.001	0.279	Schwann	*Ajap1*
0	0	1.087139	0.72	0	0.72	Schwann	*Cmtm5*
0	0	0.987317	0.32	0	0.32	Schwann	*Ugt8a*
0	0	0.917852	0.48	0.003	0.477	Schwann	*Slc35f1*
0	0	0.8408	0.44	0.001	0.439	Schwann	*Gal3st1*
0	0	3.319028	0.996	0.506	0.49	Mphage	*Lyz2*
0	0	2.967352	0.827	0.242	0.585	Mphage	*Cd74*
0	0	2.795101	0.997	0.258	0.739	Mphage	*Ctss*
0	0	2.719053	0.969	0.716	0.253	Mphage	*Apoe*
0	0	2.704733	0.701	0.15	0.551	Mphage	*C1qa*
0	0	2.662917	0.803	0.356	0.447	Mphage	*Spp1*
0	0	2.589212	0.709	0.157	0.552	Mphage	*C1qb*
0	0	2.532003	0.598	0.138	0.46	Mphage	*H2-Aa*
0	0	2.522222	0.995	0.22	0.775	Mphage	*Fcer1g*
0	0	2.480335	0.976	0.517	0.459	Mphage	*Lgals3*
0	0	2.465738	0.6	0.143	0.457	Mphage	*H2-Ab1*
0	0	2.41402	0.531	0.13	0.401	Mphage	*H2-Eb1*
0	0	2.313052	0.71	0.147	0.563	Mphage	*Pf4*
0	0	2.304647	0.681	0.095	0.586	Mphage	*C1qc*
0	0	2.304346	0.996	0.224	0.772	Mphage	*Tyrobp*
0	0	2.301151	0.787	0.228	0.559	Mphage	*Cxcl2*
0	0	2.203474	0.912	0.188	0.724	Mphage	*Ccl6*
0	0	2.148269	0.898	0.124	0.774	Mphage	*Cd52*
0	0	2.02226	0.995	0.13	0.865	Mphage	*Laptm5*
0	0	2.007304	0.906	0.146	0.76	Mphage	*Ccl9*
0	0	5.983103	0.924	0.047	0.877	Neutro	*S100a9*
0	0	3.621105	0.583	0.002	0.581	Neutro	*Retnlg*
0	0	2.43733	0.879	0.069	0.81	Neutro	*Il1r2*
0	0	2.297768	0.424	0.003	0.421	Neutro	*Wfdc21*
0	0	2.26181	0.894	0.063	0.831	Neutro	*Trem1*
0	0	2.150576	0.689	0.018	0.671	Neutro	*Acod1*
0	0	2.037901	0.78	0.035	0.745	Neutro	*Mmp9*
0	0	2.013862	0.697	0.011	0.686	Neutro	*Hdc*

0	0	1.928581	0.742	0.033	0.709	Neutro	*Pglyrp1*
0	0	1.78749	0.295	0.001	0.294	Neutro	*Stfa2l1*
0	0	1.603845	0.697	0.011	0.686	Neutro	*Cxcr2*
0	0	1.53489	0.803	0.053	0.75	Neutro	*Sell*
0	0	0.829915	0.432	0.004	0.428	Neutro	*Mirt1*
0	0	0.800909	0.386	0.001	0.385	Neutro	*AC110211.1*
0	0	0.767843	0.273	0.001	0.272	Neutro	*Il1f9*
0	0	0.757164	0.288	0.003	0.285	Neutro	*Chil1*
6.47E-272	1.28E-267	5.655579	0.97	0.101	0.869	Neutro	*S100a8*
1.40E-259	2.76E-255	0.713815	0.311	0.008	0.303	Neutro	*Fpr1*
2.12E-250	4.20E-246	0.954082	0.568	0.032	0.536	Neutro	*Trem3*
1.02E-228	2.02E-224	0.414187	0.288	0.008	0.28	Neutro	*Rab44*
0	0	5.692046	0.926	0.003	0.923	Mast	*Mcpt4*
0	0	5.373194	0.926	0.005	0.921	Mast	*Cma1*
0	0	5.061608	0.926	0.002	0.924	Mast	*Tpsb2*
0	0	5.019347	1	0.002	0.998	Mast	*Cpa3*
0	0	3.578582	0.963	0.014	0.949	Mast	*Hdc*
0	0	2.858678	0.852	0	0.852	Mast	*Mrgprb1*
0	0	2.530727	0.741	0	0.741	Mast	*Tpsab1*
0	0	2.514639	0.926	0.013	0.913	Mast	*Kit*
0	0	2.436428	0.333	0	0.333	Mast	*Cma2*
0	0	2.418319	0.926	0.001	0.925	Mast	*Cyp11a1*
0	0	2.206939	0.778	0	0.778	Mast	*Fcer1a*
0	0	1.977028	0.37	0	0.37	Mast	*Prss34*
0	0	1.939259	0.963	0	0.963	Mast	*Ms4a2*
0	0	1.935889	0.815	0.007	0.808	Mast	*Rab27b*
0	0	1.873939	0.889	0.003	0.886	Mast	*Slc6a4*
0	0	1.805867	0.852	0	0.852	Mast	*Mrgprb2*
0	0	1.754101	0.889	0.007	0.882	Mast	*Tespa1*
0	0	1.668516	0.852	0.007	0.845	Mast	*Slc18a2*
0	0	1.545677	0.63	0	0.63	Mast	*Tph1*
0	0	1.367697	0.815	0.004	0.811	Mast	*Sytl3*
0	0	3.053337	0.882	0.024	0.858	DC	*Siglech*
0	0	2.815606	0.806	0.002	0.804	DC	*Ly6d*
0	0	2.640587	0.882	0.006	0.876	DC	*Ccr9*
0	0	1.776259	0.656	0	0.656	DC	*Iglc3*
0	0	1.776141	0.849	0.007	0.842	DC	*Cd7*
0	0	1.733597	0.882	0.021	0.861	DC	*Bcl11a*
0	0	1.684004	0.903	0.006	0.897	DC	*Ptprcap*
0	0	1.52704	0.796	0.004	0.792	DC	*Pacsin1*

0	0	1.48293	0.667	0.005	0.662	DC	*Fcrla*
0	0	1.463509	0.763	0.025	0.738	DC	*Gpr171*
0	0	1.419283	0.71	0.003	0.707	DC	*Spib*
0	0	1.357869	0.72	0.001	0.719	DC	*Gm21762*
0	0	1.321748	0.71	0.02	0.69	DC	*Smim5*
0	0	1.306849	0.71	0.01	0.7	DC	*Mctp2*
0	0	1.25465	0.43	0.001	0.429	DC	*Igkc*
0	0	1.212644	0.72	0.01	0.71	DC	*Upb1*
0	0	1.187384	0.613	0.021	0.592	DC	*Lrp8*
0	0	1.144204	0.516	0	0.516	DC	*Mzb1*
0	0	1.122971	0.43	0	0.43	DC	*Klk1*
0	0	1.053417	0.57	0.017	0.553	DC	*Sh3bgr*

Table 3-4: Top 20 genes expressed in each endothelial cell subpopulation cluster

p_val	p_val_adj	avg_logFC	pct.1	pct.2	pct.diff	cluster	gene
1.70E-98	3.37E-94	1.062243	0.99	0.733	0.257	Capillary.EC.1	*Gpihbp1*
9.88E-82	1.95E-77	1.131859	0.947	0.574	0.373	Capillary.EC.1	*Rgcc*
2.24E-68	4.43E-64	0.865167	0.962	0.727	0.235	Capillary.EC.1	*Kdr*
2.98E-68	5.90E-64	0.865231	0.96	0.746	0.214	Capillary.EC.1	*Tspan13*
1.72E-66	3.39E-62	0.863168	0.916	0.61	0.306	Capillary.EC.1	*Cd300lg*
1.56E-64	3.08E-60	0.626818	0.999	0.824	0.175	Capillary.EC.1	*Cdh5*
3.70E-64	7.31E-60	1.065456	0.948	0.636	0.312	Capillary.EC.1	*Aqp1*
4.18E-58	8.27E-54	0.758685	0.94	0.778	0.162	Capillary.EC.1	*Cd200*
7.53E-56	1.49E-51	0.891523	0.938	0.763	0.175	Capillary.EC.1	*Tcf15*
4.85E-55	9.60E-51	1.204337	0.789	0.445	0.344	Capillary.EC.1	*Timp4*
1.86E-54	3.68E-50	0.80661	0.913	0.737	0.176	Capillary.EC.1	*Cav2*
6.22E-53	1.23E-48	0.831158	0.808	0.487	0.321	Capillary.EC.1	*Clic5*
7.30E-53	1.44E-48	0.66859	0.996	0.841	0.155	Capillary.EC.1	*Ly6c1*
1.03E-52	2.04E-48	0.682497	0.872	0.659	0.213	Capillary.EC.1	*Ctnnbip1*
2.54E-51	5.02E-47	0.738827	0.914	0.646	0.268	Capillary.EC.1	*C1qtnf9*
1.17E-49	2.31E-45	0.718219	0.841	0.57	0.271	Capillary.EC.1	*Jup*
1.31E-49	2.58E-45	0.779908	0.866	0.646	0.22	Capillary.EC.1	*Lims2*
1.22E-48	2.41E-44	0.685654	0.942	0.767	0.175	Capillary.EC.1	*Afdn*
6.95E-47	1.38E-42	0.811243	0.897	0.676	0.221	Capillary.EC.1	*Tcim*
1.07E-44	2.11E-40	0.966124	0.58	0.208	0.372	Capillary.EC.1	*Car4*
1.62E-44	3.20E-40	0.547063	0.944	0.75	0.194	Capillary.EC.1	*Emcn*
1.29E-90	2.56E-86	1.137749	0.59	0.013	0.577	Capillary.EC.2	*Scara5*
4.09E-77	8.10E-73	0.536022	0.41	0.005	0.405	Capillary.EC.2	*Mme*
6.00E-75	1.19E-70	1.300116	0.692	0.032	0.66	Capillary.EC.2	*Abi3bp*
1.34E-69	2.65E-65	0.750619	0.538	0.016	0.522	Capillary.EC.2	*Svep1*
4.34E-66	8.59E-62	0.585115	0.538	0.018	0.52	Capillary.EC.2	*Zfhx4*
2.94E-64	5.81E-60	0.487362	0.385	0.006	0.379	Capillary.EC.2	*Sox9*
3.96E-64	7.84E-60	0.964631	0.538	0.02	0.518	Capillary.EC.2	*Fbln1*
3.81E-62	7.54E-58	0.960262	0.513	0.018	0.495	Capillary.EC.2	*Gfpt2*
2.43E-58	4.80E-54	1.075102	0.513	0.021	0.492	Capillary.EC.2	*Dpep1*
1.09E-55	2.15E-51	1.194491	0.667	0.045	0.622	Capillary.EC.2	*Fndc1*
1.27E-55	2.50E-51	0.655964	0.487	0.019	0.468	Capillary.EC.2	*Podn*
2.30E-55	4.55E-51	1.001715	0.641	0.041	0.6	Capillary.EC.2	*Pdgfra*
7.12E-51	1.41E-46	1.281911	0.487	0.023	0.464	Capillary.EC.2	*Angptl1*
2.36E-49	4.68E-45	0.644649	0.436	0.017	0.419	Capillary.EC.2	*Arhgap20*
6.31E-49	1.25E-44	1.099917	0.615	0.044	0.571	Capillary.EC.2	*Loxl1*
6.74E-49	1.33E-44	1.238539	0.59	0.04	0.55	Capillary.EC.2	*Htra3*
2.29E-48	4.54E-44	0.757599	0.538	0.031	0.507	Capillary.EC.2	*Scn7a*
7.91E-48	1.57E-43	0.677453	0.487	0.024	0.463	Capillary.EC.2	*Lpar1*
4.74E-46	9.38E-42	0.564926	0.564	0.036	0.528	Capillary.EC.2	*Egfr*

6.07E-46	1.20E-41	0.535627	0.41	0.016	0.394	Capillary.EC.2	*Scara3*
2.82E-152	5.58E-148	0.681372	0.768	0.011	0.757	Activated.EC	*Arhgap30*
1.20E-148	2.37E-144	1.227475	0.826	0.019	0.807	Activated.EC	*Fcgr2b*
1.17E-144	2.31E-140	1.308057	0.884	0.03	0.854	Activated.EC	*Fyb*
6.71E-141	1.33E-136	1.156838	0.725	0.012	0.713	Activated.EC	*Ms4a6b*
1.32E-139	2.61E-135	1.153249	0.841	0.026	0.815	Activated.EC	*Adgre1*
5.90E-139	1.17E-134	1.83153	0.899	0.037	0.862	Activated.EC	*Cybb*
3.69E-138	7.30E-134	0.998384	0.855	0.028	0.827	Activated.EC	*Ncf2*
1.85E-137	3.67E-133	1.321298	0.826	0.026	0.8	Activated.EC	*C3ar1*
3.35E-137	6.64E-133	1.099285	0.855	0.03	0.825	Activated.EC	*Spi1*
2.94E-136	5.81E-132	0.711061	0.609	0.004	0.605	Activated.EC	*Tnfaip8l2*
4.74E-136	9.38E-132	1.157516	0.812	0.024	0.788	Activated.EC	*Aif1*
1.54E-135	3.05E-131	0.810659	0.768	0.019	0.749	Activated.EC	*Clec4a1*
3.62E-135	7.17E-131	1.588221	0.855	0.031	0.824	Activated.EC	*Ms4a6c*
7.76E-134	1.54E-129	1.39379	0.913	0.041	0.872	Activated.EC	*Ptprc*
1.04E-133	2.05E-129	0.739551	0.667	0.009	0.658	Activated.EC	*Dock2*
1.21E-132	2.40E-128	1.230584	0.855	0.031	0.824	Activated.EC	*Ly86*
1.36E-130	2.70E-126	0.957598	0.768	0.021	0.747	Activated.EC	*Csf2ra*
3.29E-130	6.51E-126	0.731448	0.667	0.01	0.657	Activated.EC	*Epsti1*
1.72E-129	3.39E-125	0.966317	0.696	0.014	0.682	Activated.EC	*Fcgr1*
1.01E-128	1.99E-124	1.990227	0.942	0.055	0.887	Activated.EC	*Laptm5*
4.66E-87	9.22E-83	1.302079	0.664	0.06	0.604	Arterial.EC	*Alpl*
1.71E-86	3.38E-82	1.458309	0.744	0.093	0.651	Arterial.EC	*Sema3g*
1.71E-84	3.38E-80	1.770119	0.8	0.127	0.673	Arterial.EC	*Fbln5*
2.46E-80	4.87E-76	1.729555	0.88	0.177	0.703	Arterial.EC	*Stmn2*
5.95E-80	1.18E-75	1.017539	0.456	0.018	0.438	Arterial.EC	*Gja5*
2.67E-79	5.28E-75	1.148044	0.624	0.06	0.564	Arterial.EC	*Col8a1*
1.80E-67	3.56E-63	0.789036	0.528	0.045	0.483	Arterial.EC	*Eps8l2*
4.49E-61	8.89E-57	0.706346	0.472	0.037	0.435	Arterial.EC	*Crispld1*
1.30E-60	2.58E-56	0.782563	0.488	0.043	0.445	Arterial.EC	*St8sia6*
1.63E-60	3.22E-56	1.355213	0.784	0.166	0.618	Arterial.EC	*Gja4*
1.46E-58	2.90E-54	1.206113	0.704	0.13	0.574	Arterial.EC	*Hey1*
2.07E-58	4.09E-54	0.464141	0.264	0.002	0.262	Arterial.EC	*Nebl*
1.38E-50	2.74E-46	1.280464	0.6	0.104	0.496	Arterial.EC	*Edn1*
3.49E-42	6.90E-38	0.933705	0.512	0.09	0.422	Arterial.EC	*Vegfc*
1.73E-37	3.42E-33	0.476869	0.288	0.022	0.266	Arterial.EC	*Alox12*
3.96E-35	7.83E-31	0.67643	0.44	0.077	0.363	Arterial.EC	*Atp2a3*
1.46E-33	2.88E-29	0.760157	0.432	0.077	0.355	Arterial.EC	*Tgfb2*
1.46E-32	2.89E-28	0.831464	0.464	0.099	0.365	Arterial.EC	*Palld*
3.06E-32	6.06E-28	0.551942	0.392	0.061	0.331	Arterial.EC	*Car7*
5.44E-31	1.08E-26	1.000036	0.76	0.351	0.409	Arterial.EC	*Pdcd4*
7.03E-138	1.39E-133	2.182839	0.782	0.025	0.757	Venous.EC	*Selp*
1.62E-104	3.21E-100	1.273694	0.828	0.062	0.766	Venous.EC	*Chp2*

7.25E-81	1.43E-76	1.220817	0.69	0.056	0.634	Venous.EC	*Slco2a1*
6.41E-77	1.27E-72	2.120923	1	0.217	0.783	Venous.EC	*Plvap*
4.35E-75	8.60E-71	2.06285	0.897	0.146	0.751	Venous.EC	*Lrg1*
3.61E-74	7.15E-70	0.845658	0.575	0.039	0.536	Venous.EC	*Ctnnal1*
3.88E-64	7.67E-60	1.898819	0.954	0.239	0.715	Venous.EC	*Vwf*
6.09E-63	1.20E-58	1.171017	0.862	0.156	0.706	Venous.EC	*Ptgs1*
7.75E-61	1.53E-56	1.206662	0.356	0.011	0.345	Venous.EC	*Ackr1*
1.25E-56	2.48E-52	0.832853	0.644	0.076	0.568	Venous.EC	*Cysltr1*
4.21E-56	8.33E-52	0.981141	0.529	0.049	0.48	Venous.EC	*Vcam1*
9.33E-56	1.85E-51	0.773888	0.701	0.1	0.601	Venous.EC	*Thsd7a*
6.20E-54	1.23E-49	1.820038	0.989	0.421	0.568	Venous.EC	*Ehd4*
1.45E-52	2.87E-48	0.599418	0.414	0.026	0.388	Venous.EC	*Lepr*
9.73E-51	1.93E-46	0.473249	0.276	0.007	0.269	Venous.EC	*Fam174b*
3.17E-49	6.28E-45	1.670995	1	0.503	0.497	Venous.EC	*Il6st*
1.75E-48	3.46E-44	1.280101	0.816	0.193	0.623	Venous.EC	*Rasa4*
2.53E-46	5.01E-42	0.499891	0.287	0.01	0.277	Venous.EC	*Enpp6*
3.45E-46	6.82E-42	0.893335	0.471	0.049	0.422	Venous.EC	*Lbp*
4.11E-46	8.12E-42	0.530151	0.402	0.031	0.371	Venous.EC	*Plekha7*
1.36E-42	2.68E-38	1.468284	0.92	0.294	0.626	Venous.EC	*Eln*
2.60E-178	5.15E-174	2.834275	0.941	0.05	0.891	Pericytes	*Vtn*
2.07E-174	4.10E-170	2.736126	0.901	0.041	0.86	Pericytes	*Kcnj8*
3.61E-170	7.15E-166	2.418101	0.954	0.065	0.889	Pericytes	*Pdgfrb*
6.07E-167	1.20E-162	1.855282	0.888	0.039	0.849	Pericytes	*Gucy1a1*
1.72E-166	3.40E-162	1.920828	0.921	0.051	0.87	Pericytes	*Notch3*
1.77E-163	3.51E-159	2.356185	0.934	0.064	0.87	Pericytes	*Steap4*
3.35E-160	6.63E-156	2.506243	0.901	0.059	0.842	Pericytes	*Abcc9*
3.95E-156	7.81E-152	1.723156	0.875	0.049	0.826	Pericytes	*Gucy1b1*
1.68E-155	3.32E-151	1.651181	0.803	0.028	0.775	Pericytes	*Rgs4*
9.01E-154	1.78E-149	1.352332	0.77	0.024	0.746	Pericytes	*Heyl*
2.21E-153	4.37E-149	1.867014	0.855	0.048	0.807	Pericytes	*Higd1b*
2.09E-149	4.14E-145	1.805337	0.882	0.062	0.82	Pericytes	*Cox4i2*
2.05E-143	4.05E-139	2.107985	0.934	0.092	0.842	Pericytes	*Aspn*
1.05E-141	2.07E-137	1.196336	0.77	0.035	0.735	Pericytes	*Arhgef17*
5.20E-134	1.03E-129	2.38312	0.934	0.115	0.819	Pericytes	*Ndufa4l2*
2.23E-133	4.41E-129	1.686806	0.868	0.079	0.789	Pericytes	*Cygb*
2.32E-127	4.58E-123	1.32045	0.822	0.069	0.753	Pericytes	*Lhfp*
2.97E-127	5.88E-123	1.109595	0.664	0.023	0.641	Pericytes	*Itga7*
1.09E-125	2.15E-121	1.188494	0.724	0.037	0.687	Pericytes	*Atp1b2*
7.59E-125	1.50E-120	1.122424	0.724	0.04	0.684	Pericytes	*Cystm1*

CHAPTER 4: Mesoporous Silica Nanoparticles Bio-distribute and Release Payload but Does Not Enhance Skeletal Muscle Progenitor Cell Homing to Dystrophic Skeletal Muscles

Introduction

Duchenne muscular dystrophy (DMD) is an X-linked recessive, muscle wasting disease affecting 1 in every 5000 male live births. By their teens, most DMD patients are wheelchair-bound and die prematurely in their early twenties. DMD is caused by an out-of-frame mutation in the dystrophin gene that leads to absence of a functional dystrophin protein. Without dystrophin, muscle fibers go through continuous cycles of contraction-induced damage, causing continuous degeneration and regeneration of the muscle. Currently, no cure exists for DMD. Human induced pluripotent stem cells (hiPSCs), reprogrammed from patients somatic cells, can be used to model diseases and generate cells and tissues for regenerative medicine. Becker muscular dystrophy (BMD) is an allelic disease with a milder clinical phenotype than DMD. BMD mutations retain the dystrophin reading frame and produce an internally deleted but functional protein. Using the clustered regularly interspaced short palindromic repeats (CRISPR) and CRISPR-associated nuclease (Cas) 9 system, we have created a DMD-focused personalized therapy[141]. The CRISPR/Cas9 platform, designed to restore dystrophin gene reading frame created the largest deletion in DMD to date. After successful non homologues end joining (NHEJ), the generated protein product is highly stable, similar to that which has been observed in patients with very mild BMD.

Delivering skeletal muscle progenitor cells (SMPCs) with restored dystrophin and function differentiated from *ex vivo* corrected hiPSCs provides a therapeutically relevant and potentially lifelong cure for patients with DMD. Our lab has identified two cell surface markers, ERBB3 and NGFR, that enrich for myogenic populations from both fetal SMPCs and hiPSCs-SMPCs[64]. IM injections of these cells has demonstrated the best dystrophin restoration to date in dystrophin deficient mice from directly differentiated hiPSCs. However, a considerable challenge for the use of hiPSC-SMPCs as a therapeutic strategy is the lack of efficient targeting of multiple muscles, as IM injection results in local engraftment, and lack of

understanding of the ability of human SMPCs to home to muscle. It has been previously demonstrated that the chemoattractant SDF-1 is overexpressed in dystrophic muscle, and can enhance the extravasation of mouse side population stem cells into skeletal muscle after intra-arterial transplantation[118]. This study provides a proof of principle that release of chemoattractants in muscle can result in stem cell homing and contribution to dystrophin restoration after cell systemic delivery. Because growth factors are only transiently expressed after delivery, nanoparticles can be used to deliver chemoattractants to the muscle for their sustained release to enhance hiPSC-SMPC homing after systemic delivery.

Mesoporous silica nanoparticles (MSNP) are a multifunctional delivery system that has been shown *in vitro* and in intact animal levels to be capable of delivering multiple APIs (*e.g.* chemotherapeutic agents, small molecule inhibitors, nuclear acid and their combinations) to a broad range of diseases including cancer and infectious diseases [114]. The multi-functionality of MSNPs provide the possibility of efficient payload encapsulation composed of various chemical structures with the additional power to image the delivery site of interest [171–174]. In this investigation, we explored the use of a mesoporous silica nanoparticle (MSNP) platform for systemic delivery of chemoattractant to enhance ERBB3 and NGFR enriched hiPSC-SMPC migration both *in vitro* and *in vivo* in immunocompromised DMD mouse model. We found that MSNP can biodistributed to dystrophic muscle more efficiently than healthy muscle. To optimize their biodistribution to skeletal muscle, we developed and characterized MSNP carriers that were systematically manipulated to vary in size, ranging from 50~300 nm. We coated the silica surface with a uniform and intact lipid bilayer (LB) coating, which sustains long circulatory half-life, improves colloidal stability, and has high biological compatibility[171,172,175]. We show that MSNPs have the ability to package proteins and ability to maintain payloads longer in dystrophic muscle than without MSNPs. We further show that hiPSC-SMPCs can migrate *in vitro* to lipid-coated MSNP loaded with different chemoaatractans in an incucyte assay. However, the homing of enriched hiPSC-SMPCs after their IA systemic delivery was not enhanced after 24 hours of MSNP-HGF delivery, indicating that MSNPs did not enhance hiPSC-SMPC migration *in vivo*. Overall, this MSNP platform provides a potential new tool

for enhanced protein or small molecule delivery to dystrophic muscles, but further investigation needs to be conducted for their use as a combination therapy for cell-based therapeutics.

Materials and Methods

Table 4-1 Materials

Product	Vendor	Catalog No.
Tetraethylorthosicate (TEOS)	Sigma-Aldrich	86578
Triethanolamine (TEA-ol)	Sigma-Aldrich	90279
Cetyltrimethylammonium chloride solution (CTAC)	Sigma-Aldrich	292737
3-aminopropyl)triethoxysilane (APTES)	Sigma-Aldrich	440140
Gold (III) chloride hydrate ($HAuCl_4 \cdot 3H_2O$)	Sigma-Aldrich	520918
Trisodium citrate dihydrate	Sigma-Aldrich	S4641
Cytochrome c	Avanti Polar Lipids	C2037
1,2-Distearoyl-sn-glycero-3-phosphocholine (DSPC)	Avanti Polar Lipids	850365
1, 2-distearoyl-sn-glycero-3-phosphoethanolamine-N-[methoxy (polyethylene glycol)-2000] (ammonium salt) ($DSPE\text{-}PEG_{2000}$)	Avanti Polar Lipids	880120
Cholesterol (Chol)	Avanti Polar Lipids	700000
Anti-CD31 antibody	BD Pharmingen	553708
Anti-collagen IV antibody	Abcam	ab19808
Anti-Laminin antibody	Sigma-Aldrich	L9393
Anti-alpha smooth muscle actin (a-SMA) antibody	Sigma-Aldrich	A5228
Alexa Fluor® 488 conjugated goat anti-rat IgG (H+L) secondary antibody	Thermo Fisher Scientific	A11006
Alexa Fluor® 594 conjugated goat anti-rat IgG (H+L) secondary antibody	Thermo Fisher Scientific	A11007
Alexa Fluor® 488 conjugated goat anti-rabbit IgG (H+L) secondary antibody	Thermo Fisher Scientific	A11008
Alexa Fluor® 594 conjugated goat anti-rabbit IgG (H+L) secondary antibody	Thermo Fisher Scientific	A11012
DyLight 680 NHS ester	Thermo Fisher Scientific	46418
Incucyte® Clearview 96-well Plate for Chemotaxis	Sartorius	4582

Animals

All animal work was conducted under protocols approved by the UCLA Animal Research Committee (ARC) in the Office of Animal Research Oversight (OARO). C57BL/10J (C57, #000665) C57BL/10ScSn-Dmd^{mdx}/J (Mdx, #001801). To generate immunocompromised strains, Mdx mice were crossed to NOD.Cg-

Prkdc^{scid} Il2rg^{tm1Wjl}/SzJ (NSG, 005557) mice. Mice containing the severe combined immune deficiency (scid) and a complete null allele of the IL2 receptor common gamma chain (IL2rgnull) were then back crossed to Mdx for at least 5 generations to create congenic strains. All the animals were housed in the Biomedical Sciences Research Building's Humanized Mouse Core at UCLA, an immunocompromised core facility. All mice experiments were conducted between 2 and 4 months of age, and all experiments were performed on age and sex matched controls.

Compare the biodistribution of MSNPs between DMD and wildtype mouse models

To compare the biodistribution of MSNPs between the dystrophic and wildtype mice, NIR labeled LB coated MSNPs with an optimized size (~70 nm) were used. In this experiment, C57BL/6 and mdx mice (n=3, ~3 months) received an identical dose of NIR-labeled particles (50 mg/kg MSNPs) by intravenous (IV) injection. After 24 h, animals were sacrificed and followed by *ex vivo* imaging of the excised different muscles and major organs. MSNPs signal intensity was quantified by IVIS Lumina Living Image software. Muscles were immediately cryo-embedded in OCT reagent to prepare sections for confocal microscopy study of MSNPs intramuscular distribution as described above.

Size dependent biodistribution of nanoparticles in mdx-NSG mice

To study the size effect of MSNPs on biodistribution in DMD mouse model, monodisperse spherical MSNPs with different primary size range from ~50 to ~300 nm but with the same lipids surface coating were synthesized. In order to detect the particles via *in situ* fluorescence imaging, the MSNP core was labeled by a near-infrared (NIR) dye. First, the different sized MSNPs were synthesized by a sol-gel chemistry using a seed-growth procedure. MSNPs (pore size ~3 nm) ~50 nm in diameter was synthesized with minor modifications as described in our previous reports[171,172]. Briefly, 5 mL of CTAC (25 wt% in water) was added to 15 mL of DI H_2O, followed by stirring at 500 rpm for 10 min at 85 °C. This was followed by the addition of 0.8 mL of 10% (w/v) TEA-ol for 10 min at the same temperature. Then, 1 mL of the silica precursor, TEOS, was added. The solution was stirred at 500 rpm at 85 °C for 1 h, leading to the formation particles with a primary size of ~50 nm. The as-synthesized 50 nm particles were further

used as seed to grow into large size MSNPs. Synthesis of larger MSNPs was performed in the same manner as making the 50 nm particles but add 1 mL of above 50 nm seed particles to the mixture of CTAC and TEA-ol solution before adding the TEOS. The final particle size of the MSNPs was controlled by adjusting the amount of TEOS in the growth step, which led to other three MSNPs of different particle sizes (~100, 200, and 300 nm). The particles were extensively washed by in acidic ethanol (HCl/ethanol, 4:100 v/v) through a repeated centrifugation and resuspension process (3 rounds) to remove the surfactant CTAC as before. Second, the purified MSNPs were labeled by the NIR dye as described previously[171,176], which were first surface functionalized with NH_2 groups using APTES and then were conjugated with the NHS ester of NIR fluorescent dye, DyLight 680 NHS ester (0.1 wt% to MSNPs). Last, the NIR labeled MSNPs in different sizes were coated with a lipid bilayer (LB)[171,177]. Briefly, a mixture of lipids (32 mg DSPC, 10.8 mg, cholesterol (Chol) and 5.4 mg DSPE-PEG_{2000}, yielding a DSPC/Chol/DSPE-PEG_{2000} molar ratio of 3:2:0.15) was dissolved in 100 μL pure ethanol at ~65°C. One mL of a preheated (~65 °C) solution, containing a 20 mg/mL NIR labeled MSNP suspension into was added into the lipid solution and mixed by pipetting. The mixture was treated by probe sonication (power = 52 W) using a 10s/5s on/off cycle for 10 min. The particle suspension was purified by centrifugation and washing with PBS for 3 times. The particle morphology is characterized using a transmission electron microscope (JEOL 1200-EX) and the coated lipid bilayer on MSNPs was visualized by cryoEM (TF20 FEI Tecnai-G2). The fluorescence spectra of labeled particles were measured by a Microplate Reader (M5e, Molecular Device, USA). Particle hydrodynamic size and zeta potential were measured by a ZETAPALS instrument (Brookhaven Instruments Corporation).

For the animal study, IVIS (Xenogen) imaging was used to evaluate the size effect on biodistribution of NIR-labeled NPs in mdx-NSG mice (n=3). Animals (2-4 months) received same dose of different size NIR-labeled particles (50 mg/kg MSNPs) by intravenous (IV) injection (100 μL). After 24 h, animals were sacrificed and all tissues immediately dissected. This was followed by *ex vivo* imaging of the excised

different muscles and major organs. MSNPs signal intensity was quantified by IVIS Lumina Living Image software.

Immediately following IVIS imaging, gastrocnemius, quadriceps, triceps, and tibialis anterior muscles were embedded in tissue plus optimal cutting temperature (O.C.T.) compound and flash frozen in isopentane chilled by liquid nitrogen (LN2) and then stored in isopentane filled scintillation vials at -80C. Liver and spleen were fixed in 4% PFA and stored in 70% EtOH for toxicity analysis.

Ultrastructural analysis of the intramuscular delivery of MSNPs through TEM viewing

The lipid coated MSNPs with an ~10 nm gold core was synthesized by a three-steps procedure as shown in our previous report[176], i.e., first make gold nanoparticles, then grow the mesoporous silica shell on the gold core to achieve the final size ~70 nm, finally coat the MSNP with LB coating. Mdx mice (~3 months) received an IV injection of 50 mg/kg of the Au-core marked MSNPs. After 24 h, animals were sacrificed and muscle biopsies were collected, washed in PBS, and immediately fixed with 2.5% glutaraldehyde. Further sample preparation and sectioning were performed by the Electron Microscopy Services Center at UCLA. After fixation in 1% OsO_4, the samples were dehydrated in propylene oxide and embedded in resin. Tissue slices of 60-80 nm thick were placed on copper grids, and viewed under a JEOL 1200-EX electron microscope.

Systemic delivery of NIR-Cytochrome-C loaded MSNP in mdx-NSG

MSNPs with different pore sizes larger than 3 nm were synthesized by applying a heterogeneous oil−water biphase stratification reaction system according to the literature with modification[114,178]. Generally, 0.18 g of TEA-ol was dissolved in 1 ml of H_2O, and then added to a mixture of 35 ml H_2O and 24 mL CTAC (25 w% solution) in a 100 ml flask at 60 °C under stirring at 350 rpm using a magnetic stir bar of 2.5 cm in length. After 0.5 h, 20 mL of TEOS cyclohexane solution were gently added to the top of aqueous solution for reaction overnight. Twenty percent v/v, 10 v/v% and 5 v/v % of TEOS was used to make MSNPs with

pore size ~7 nm, ~13 nm and ~19 nm, respectively. The big pore size MSNPs were purified by washing with acidic ethanol similar as the MSNPs with 3 nm pore size shown above.

Tanswell Incucyte Assay

Transwell migration assay was used to study the motility of hiPSC-SMPCs from top chamber (the insert wells) to the bottom chamber (the reservoir plate). hiPSC-SMPCs were dissociated from 6 well plate, counted and cultured in the top chamber of Incucyte® Clearview 96-well Plate for Chemotaxis at 1000 cells/ insert well. The following concentration of free chemoattractant or MSNP-chemoattractant were added to the bottom wells in n=3: 100, 250 and 500 ng/ml of NRG1; 400, 1000, and 1500 ng/ml of HGF; 500, 1000 and 1500 ng/ml FGF2; 100, 500, 2500 and 5000 ng/ml of MSNP-NRG1; 500,1500, 10000, and 15000 ng/ml of MSNP-HGF, and 500, 1500, 10000 and 15000 of MSNP-FGF2. The concentration of loaded MSNP-chemoattractant doses depended on a 10% release dose to media. 20%, 10%, 1% FBS as well as free media were used as controls for cell migration. The migration of cells was followed using an incucyte live-cell analysis system over 48-hour time period.

Immunofluorescence staining

Mouse muscles were frozen in isopentane cooled in liquid nitrogen. Frozen muscles were serially sectioned at 10 μm thick cryosections. A Hydrophobic barrier was drawn around sections, then washed with 0.1% Tween in PBS (PBST). Immunofluorescence staining included TrueBlack® Lipofuscin Autofluorescence Quencher (Biotium) and blocking buffer (0.2% gelatin, 3% BSA, 10% goat serum, 0.1% tween-20 in PBS) to improve signal to noise ratio in identifying MSNPs by epi-fluorescent (Zeiss Observer-1) and confocal (Zeiss LSM-780 and Leica SP8) microscopy. When needed, CD31 and Laminin were used for staining and were incubated in humidified chamber overnight at 4 ˚C.

Intra-arterial Cell Delivery

The surgery was performed by making an incision at the inguinal region on the right hindlimb parallel to the femoral vascular bundle, and the femoral vascular bundle is exposed. The femoral artery is then isolated, two 6-0 sutures are passed under it, and one suture is used to obstruct blood flow, upstream of the injection site. In a proximal location to the body, a small cut is made in the femoral artery using a 32 G needle. A 32 G catheter is then inserted (cannulation site) into the femoral artery. Using a pump 500K dissociated ERBB3 and NGFR enriched hiPSC-SMPCs were delivered at a flow rate of 50 ul/min in a volume of 150 ul of HBSS. After the cell injection, saline was flushed through the catheter to deliver any remaining cells in the catheter. The catheter then is retracted slowly, and while obstructing blood flow upstream of the injection site, a cautery is used to seal the femoral artery at the cannulation site. After sealing the femoral artery and removing the suture obstructing the blood flow, blood should be seen flushing again through the femoral artery. The opened incision area is filled with saline and the incision is sutured using a 5-0 absorbable suture. Mice are monitored after the surgery and kept in cages over a heating pad for recovery. Mice are provided with Carprofen 5 mg/kg of body weight. After 48 hours mice were sacrificed and their lungs and muscles were collected by freezing them in isopentane cooled in liquid nitrogen.

Western blot analysis

MSNP-HGF was intramuscularly injected in the quadricep muscles of mdx-NSG mice at different concentrations MSNP-HGF high at 450 ng, and MSNP-HGF low at 16 ng. Muscles were collected 24 hours after injection and flash frozen, then they were homogenized on ice in Mito-buffer (0.25 M sucrose, 20 mM Tris-HCl (pH 7.4), 0.2mM EDTA, protease/phosphatase inhibitor cocktail). The Lysates were centrifuged for 10 minutes at 13000 g to fractionate the lysates to a pellet with myofibrillar fraction which includes myofibrils, nuclei, mitochondria and MSNPs, and supernatant with cytosolic and membrane fractions. The Supernatant fraction was further centrifuged at 13000 g for 45 minutes to fractionate to a cytosol fraction (supernatant and pellet fraction (membrane fraction). The different fractions were used for western blot analysis.

Statistical analysis

Comparative analysis of differences between groups was performed using the 2-tailed Student's *t*-test (Excel software, Microsoft) for two-group comparison. A One-way ANOVA followed by a Tukey's test (Origin software, OriginLab) was performed for multiple group comparisons. Data were expressed as mean ± SD or SEM, as stated in the figure legends. A statistically significant difference was considered at $p < 0.05$.

Results

Systemic administration MSNP-based nanocarriers leads to abundant distribution in dystrophic skeletal muscles, but not the healthy muscles

As nanoparticles historically do not biodistribute to skeletal muscle [179,180], we set out to determine whether biodistribution to skeletal muscles would be enhanced in the dystrophic environment. We selected MSNP size of 70 nm for comparative analysis on age-matched healthy C57BL/6 vs mdx mice (**Figure 4-1A**). NIR-labeled MSNPs were IV administered (10mg/ml) via tail vein, followed by sacrifice at 24 hours, immediate muscle harvest, and imaging using the IVIS system. We found preferential and significant MSNP retention in all limb skeletal muscles of dystrophic mice, and this profile was completely changed in wildtype muscles in which little NIR signal was detected (**Figure 4-1B, top panel**). Quantitative analysis of signal intensity found MSNP distribution is muscle type-dependent, i.e. gastrocnemius and quadriceps exhibited 6-10-fold greater MSNP abundance than wildtype mice, while signal was 2-fold greater in tibialis anterior muscles. The NIR signal in the heart was weak suggesting MSNP retention in cardiac and skeletal muscles occur through separate mechanisms. In addition to muscles, we also harvested the major organs from the same mice including reticuloendothelial systems (RES), such as liver and spleen (**Figure 4-1B, bottom panel**). While IV injection of 70 nm MSNPs led to significant RES organ uptake in normal mice, we found a significant reduction in RES uptake in mdx mice. Most notably, MSNP signal was reduced in the spleen and liver by 3-fold and 1.5-fold in mdx mice, respectively. This is the first demonstration of a nanocarrier

to selectively target skeletal muscles as compared to off-targeted RES organs, presumably due to the competitive MSNP retention within dystrophic mdx muscles.

Size-controlled lipid-coated mesoporous silica nanoparticle for chemoattractant encapsulation

To optimize MSNP delivery to dystrophic skeletal muscle, we investigated whether MSNP homing was size-dependent. Four size-controlled MSNP diameter candidates were selected for synthesis at 50 nm, 100 nm, 200 nm, and 300 nm and fully characterized. Size control was achieved through a simple seed-growth process by first making 50 nm bare MSNPs using a sol-gel chemistry[171,172], and then using them as cores to further grow the larger particles[181,182]. The primary size of purified bare MSNPs were characterized using transmission electron microscopy (TEM), and four uniform MSNP sizes with incremental primary diameters of 47.5 ± 6.6 nm ~ 301.6 ± 11.2 nm were obtained (**Figure 4-2A**). To track the biodistribution of MSNPs at the tissue and cellular levels in dystrophic muscles, purified MSNPs were surface functionalized which enabled conjugation of near-infrared (NIR) dye. Characterization of LB coated MSNPs demonstrated uniform coatings, colloidal stability, and negative zeta potential which can minimize non-specific adsorption of serum proteins by NPs in blood and prolong the NP's circulation time [177,183,184] (**Figure 4-2A**).

To evaluate MSNP biodistribution, mdx-NSG mice received a single IV injection of 10 mg/mL NIR dye-labeled MSNPs with different size ranges at 50 mg silica dose *per* kg through the tail vein. All mice survived IV injections and were sacrificed 24 hours post injection. Skeletal and cardiac muscles were dissected and immediately imaged *ex vivo* using the IVIS imaging system (**Figure 4-2B, top panel**). Contrary to previous reports on the impenetrable anatomy of skeletal muscle to nanoparticles, we measured several significant differences using our MSNP library. Both 50 nm and 100 nm MSNPs showed strong NIR fluorescence intensity in upper and lower limb skeletal muscles including gastrocnemius, quadriceps, and triceps. 50 nm NPs were also significantly increased in diaphragm and heart muscles relative to other sizes, $p<0.05$. Conversely, mice receiving 200 and 300 nm sized NPs showed less abundance in skeletal limb muscles and

limited signal in diaphragm and heart muscles. In addition to muscles, we also harvested the major organs from the same mice including reticuloendothelial systems (RES) organs (liver and spleen), kidneys, and lungs (**Figure 4-2C, bottom panel**). We observed a contrasting trend in that 200-300 nm MSNPs were sequestered in RES organs. This was especially true of the spleen which showed a significant size-dependent accumulation, which was 20-fold and 50-fold greater than 100 nm and 50 nm MSNPs (data not shown). We concluded that 50 - 100 nm is an optimal diameter for systemic administration of LB coated MSNPs. We therefore found that our initial analysis with an intermediate MSNP size of ~70 nm to be the optimal size for growth factor delivery. We further evaluated the localization of MSNP by performing ultrastructural analysis to confirm MSNP muscle access using transmission electron microscopy (TEM). In order to provide the best resolution via TEM, we synthesized MSNPs containing a ~10 nm gold core (**Figure 4-2C**), which could be readily visualized due to the unique core/shell NP structure and the high electron density of Au element[176]. Gastrocnemius muscle containing gold core laded MSNP was harvested after 24 hours IV injection and used for TEM visualization. We were able to show gold-labeled MSNP in the gastrocnemius muscle tissue both in a blood vessel lumen and in the interstitial space.

MSNP payload extravasates from skeletal muscle vasculature and is retained for up to 48 hours

To determine whether MSNPs can deliver payload, proteins or growth factors, to the muscle, and optimal time of the payload release, we first delivered MSNP packaged NIR-labeled Cytochrome-C via intravenously injection through the tail vein, and visualized biodistibution by IVIS 1, 4, 24 and 48 hours (**Figure 4-3A**). We found that Cytochrome-C was able to biodistribute to skeletal muscle at all time points. Injection of free NIR-labeled Cytochrome-C not packaged in MSNPs was not visible in skeletal muscle by IVIS imaging. To confirm Cytochrome-C biodistribution, we sectioned and stained skeletal muscle, and identified a high abundance of Cytochrome-C in quadriceps at all time points. Cytochrome-C was primarily localized within blood vessels (CD31+) at 1 and 4 hours, and by 24 hours had exited from circulation into the interstitial space of skeletal muscles (**Figure 4-3B**). We therefore determined that the best time point of hiPSC-SMPC delivery to skeletal muscles would be 24 hours after MSNP-chemoattractant delivery.

In-vitro transwell assay identifies HGF as the best chemoattractant for skeletal muscle progenitor cells migration.

To explore hiPSC-SMPC migration to chemoattractants *in vitro* we utilized the IncuCyte™ chemotaxis imaging system. In brief we plated ERBB3 and NGFR enriched hiPSC-SMPCs into the top chamber of the IncuCyte™ ClearView 96- Well Cell Migration Plate at a density of 1000 cells/well and chemoattractant loaded MSNPs were seeded in the bottom chamber (**Figure 4-4A**). Automated image processing was utilized to image cells migrating to the bottom chamber through the pores, and the number of migrated cells were plotted in real time (**Figure 4-4B**). Fold change of cell migration to the bottom chamber from control MSNPs is shown in **Figure 4-4C.** The best migration of hiPSC-SMPCs was to MSNP-HGF (500 ng/ml) and MSNP-FGF2 (500 ng/ml). We further found that higher concentrations of MSNPs loaded with chemoattractant are not effective at enhancing the migration of hiPSC-SMPCs. Hereafter, we decided to proceed with MSNP-HGF delivery *in vivo* given its important role in cell migration in different contexts including during development[185–189].

MSNP-HGF is retained in the muscle interstitial space but does not enhance hiPSC-SMPC homing to muscle

Initial characterization of protein release from MSNPs was performed *in vivo* using intramuscular (IM) injection MSNPs containing HGF. We measured protein release and retention by western blot MSNP-HGF or free HGF and found that only MSNPs containing HGF was present in skeletal muscle after 24 hours of mdx-NSG mice (**Figure 4-5A**). We sub-fractionated HGF measurements by cytosol, membrane and myofibrillar fractions, and detected HGF in both the membrane and myofibrillar fractions at 24 hours time point, but not free injected HGF. The detected HGF was at a high MSNP-HGF dose of 450 ng. This indicates that HGF was not uptaken by the muscle fiber and retained for 24but rather present in the muscle interstitial space.

NIR labeled MSNP-HGF was then delivered systemically at expected high protein dose release to mdx-NSG mouse (~ 400 µg), and ERBB3 and NGFR hiPSC-SMPCs were intra-arterially systemically delivered at 24 hours time point after MSNP-HGF injection. About 500K cells were injected into the femoral artery of the mouse. Muscles were then collected 48 hours after the systemic delivery of the cells and gastrocnemius muscle was analyzed for cell localization. hiPSC-SMPC were detected in the blood vessels, not homing to the muscles, although MSNPs can be detected in the interstitial space. Because intramuscular hiPSC-SMPCs result in local engraftment of the cells, we wondered if MSNP-HGF would further enhance the migration of the injected cells throughout the length of the muscle. Therefore, we injected tibialis anterior muscles of mdx-NSG with MSNP-HGF and enriched hiPSC-SMPCs. We found that human cells were still found at their local injection site without migrating throughout the length of the muscle (not shown). Overall, these findings indicate that MSNP is a great tool for drug, protein or growth factor delivery, but it does not enhance the homing of hiPSC-SMPC to the muscle after their systemic delivery.

Discussion

In this communication, we developed a versatile nanoparticle platform that biodistributes to dystrophic skeletal muscle and can be engineered for therapeutic delivery to the muscle interstitial space. One key discovery was the contrasting MSNP retention in dystrophic muscles versus normal muscle, accompanied by up to 1-2 log fold reduced particle content in liver and spleen. Combined use of IVIS imaging and NIR-conjugated MSNPs enabled high photon penetration *in vivo* and this suggests MSNPs could serve as a non-invasive tool for whole-body tracking of labelled drugs to skeletal muscle, in a similar manner to nanoparticle-mediated identification of tumors in cancer diagnostics[190]. We demonstrated the best MSNPs size for skeletal muscle detection to be between 50-100 nm. In this work we showed for the first time, the use of porous MSNPs for protein delivery, including the demonstration of payload release at dystrophic muscle sites of Cytochrome C and HGF. MSNPs were shown to releasee their payload 24 hours after their delivery both systemically (Cytochrome C delivery) and intramuscularly (MSNP-HGF delivery). We have, moreover, demonstrated that MSNP-chemoattractant enhances the migration of hiSMPC-SMPCs *in vitro* similar to free chemoattractant. We found MSNP-HGF to be the best chemoattractant for *in vivo* delivery at about 500 ng dose. The *in vivo* delivery of free HGF to the quadriceps of mdx-NSG mouse was not retained after 24 hours, while HGF delivered using MSNP was detected. Overall, this provides evidence that MSNP is a promising tool for protein delivery and holds potential for delivering proteins to modulate disease progression in DMD. However, as a combination therapy with cell-based therapy it proved challenging. The systemic delivery of hiPSC-SMPCs was not shown to be enhanced after MSNP-HGF delivery and mainly cells were found in the blood vessels rather than homing to the muscle. Multiple reasons could contribute to this finding including that the release of HGF after its systemic delivery was not abundant enough to enhance the homing of hiPSC-SMPCs, or that hiPSC-SMPCs were too large to leave blood vessels to the interstitial space, or the cells are not endowed with the machinery to home to muscle. Therefore, we propose that MSNPs could particularly be used as a combination therapy for drug delivery where proteins or small molecules can be delivered or for gene therapy to enhance their delivery efficiency.

Acknowledgements

This work was supported by CIRM QUEST #DISC2-08824, CIRM Inception #DISC1-08823. Seed grant funding was supported by CDMD at UCLA. We would like to thank the Humanized Mouse Core in BSRB, the Microscopy core (BSCRC), BSCRC from providing access to IncuCyte™ imaging system, the Translational Pathology Core Laboratory (TPCL), CRUMP Preclinical Imaging Technology Center, Electron Imaging Center for Nanomachines (EICN), and the Advanced Light Microscopy Center in the California NanoSystems Institute (CNSI) at UCLA.

Figures

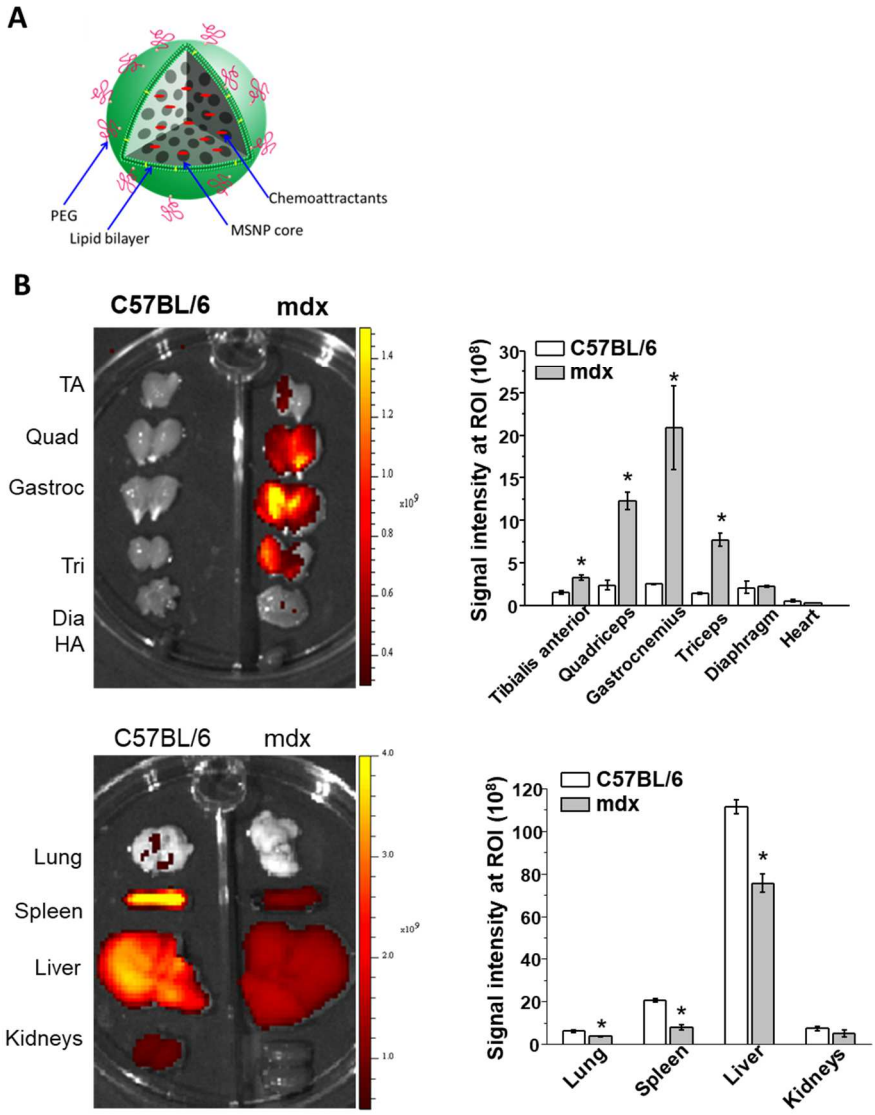

Figure 4-1: Systemic administration MSNP-based nanocarriers leads to abundant distribution in dystrophic skeletal muscles, but not the normal muscles

A) Schematic representation of the Lipid-coated mesoporous silica nanoparticles.

B) 24 h after animals received IV injection of NIR-labeled lipids coated MSNPs (50 mg/kg). NIR fluorescence intensity at region-of-interest (ROI) was used to quantify the nanoparticle content in different muscles and organs. Data represent mean ± SEM (n=3). *$P < 0.05$, 2-tailed Student's t test.

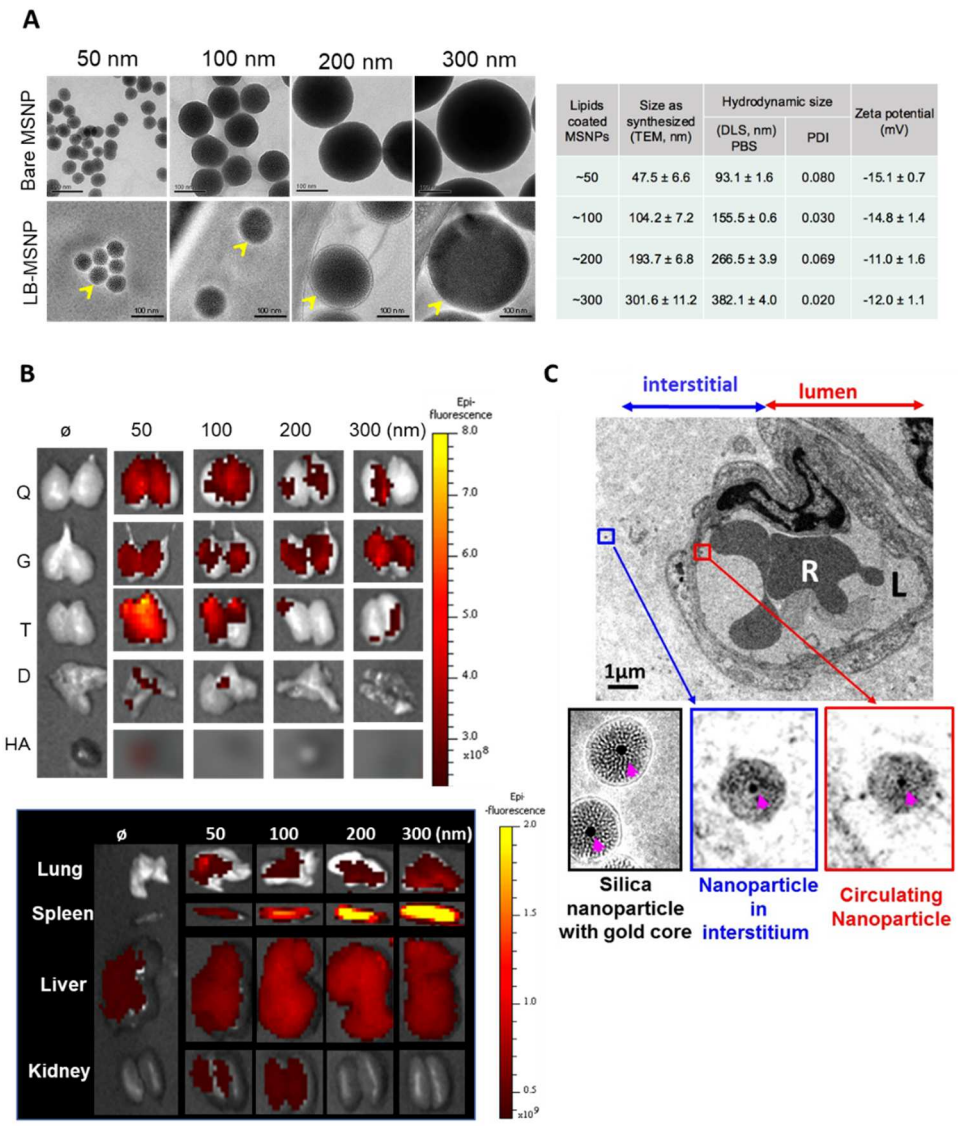

Lipids coated MSNPs	Size as synthesized (TEM, nm)	Hydrodynamic size (DLS, nm) PBS	PDI	Zeta potential (mV)
~50	47.5 ± 6.6	93.1 ± 1.6	0.080	-15.1 ± 0.7
~100	104.2 ± 7.2	155.5 ± 0.6	0.030	-14.8 ± 1.4
~200	193.7 ± 6.8	266.5 ± 3.9	0.069	-11.0 ± 1.6
~300	301.6 ± 11.2	382.1 ± 4.0	0.020	-12.0 ± 1.1

Figure 4-2: Size-controlled lipid-coated mesoporous silica nanoparticle for chemoattractant encapsulation

A) TEM visualization of bare MSNP with different sizes (upper panel). cryoEM images (lower panel) of size-controlled chemoattractant laden mesoporous nanoparticle coated with lipid bilayer (yellow arrow). Bar is 100 nm.

B) IV injection of 50 mg/kg NIR-dye labeled, size-controlled lipid-coated mesoporous silica nanoparticles in mdx NSG mice. NIR imaging of skeletal muscles, heart, lung, spleen, liver and kidney from mice 24 hrs after one IV injection. Size-dependent particle uptake was observed in mdx muscles, and correspondingly reduced in RES. Image J and ICP-OES was used to quantify the NIR intensity and silica abundance, respectively (n=3/group) (Q: Quadriceps; G, Gastrocnemius; T, Triceps; D, Diaphragm, HA: Heart).

C) Gastrocnemius muscle tissue TEM analysis after 50 nm lipid-coated with gold core delivery. Gold core serves as a "marker" due to its high electron density, stability and bioinert property. Based on the unique core/shell particle morphology (pink arrow), we confirmed the presence of particle in muscle blood vessel as well as muscle interstitial space. R: Red blood cell; L: muscle blood vessel lumen.

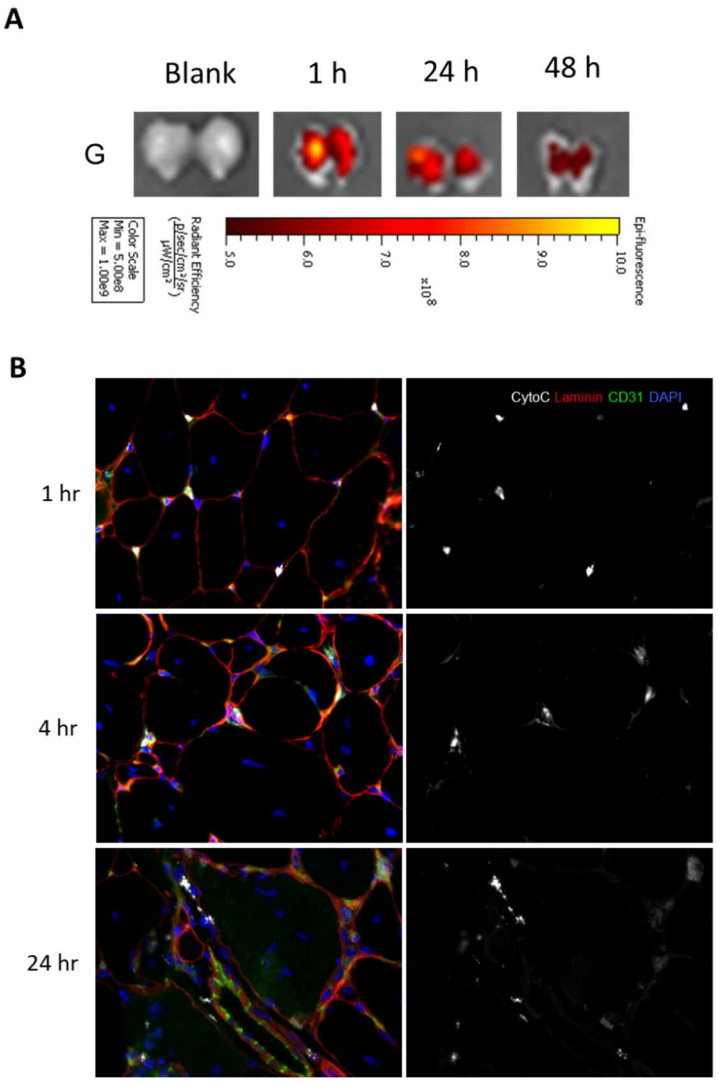

Figure 4-3: MSNP payload extravagates from skeletal muscle vasculature and is retained for up to 48 hours

A) NIR imaging of gastrocnemius (G) muscles at different time points after 2 mg lipid-coated MSNP cytochrome C delivery to mice.

B) Staining gastrocnemius muscle cross-sections with blood vessel marker (CD31, green), extracellular matrix (Laminin, red), and fluorescently labeled MSNP-Cytochrome C (CytC, white) at different time points after 2 mg MSNP, 100 ug cytrochrmoe C delivery to mice. Cytochrome C can be detected up to 24 hours in the interstitial muscle space.

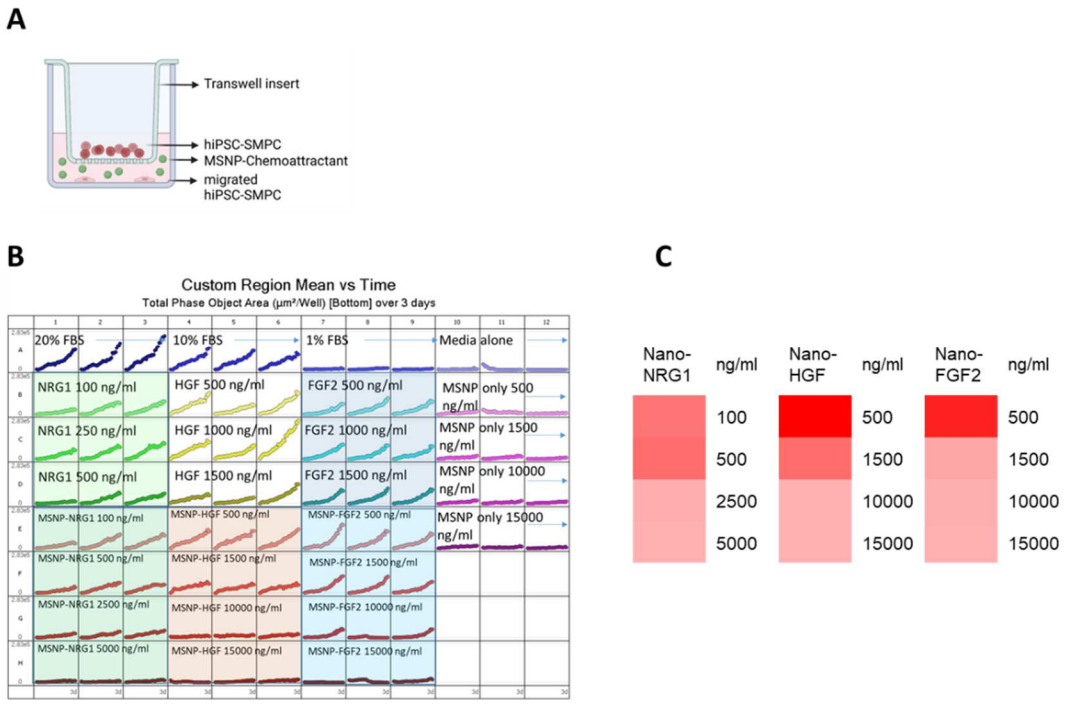

Figure 4-4: In-vitro transwell assay identifies HGF as the best chemoattractant for skeletal muscle progenitor cells migration

A) Transwell migration assay was used to study the motility of hiPSC-SMPCs from top chamber (the insert wells) to the bottom chamber (the reservoir plate). The migration of cells was followed using an incucyte live-cell analysis system over 48-hour time period. Different lipid-coated MSNPs loaded with cheomattractants were added to the reservoir plate wells.
B) Real time plot of the hiPSC-SMPC count at the bottom chamber at a 72-hour time point. Automated image processing masks the cells that have migrated to the bottom chamber and are plotted in real time.

C) Transwell migration assay used to study the migration of hiPSC-SMPCs towards lipid-coated MSNPs loaded with different chemoattractants. The migration was followed over a period of 72 hours using incucyte live-cell analysis system. Heat map shows the fold change from control nanoparticles (free) with respective concentrations.

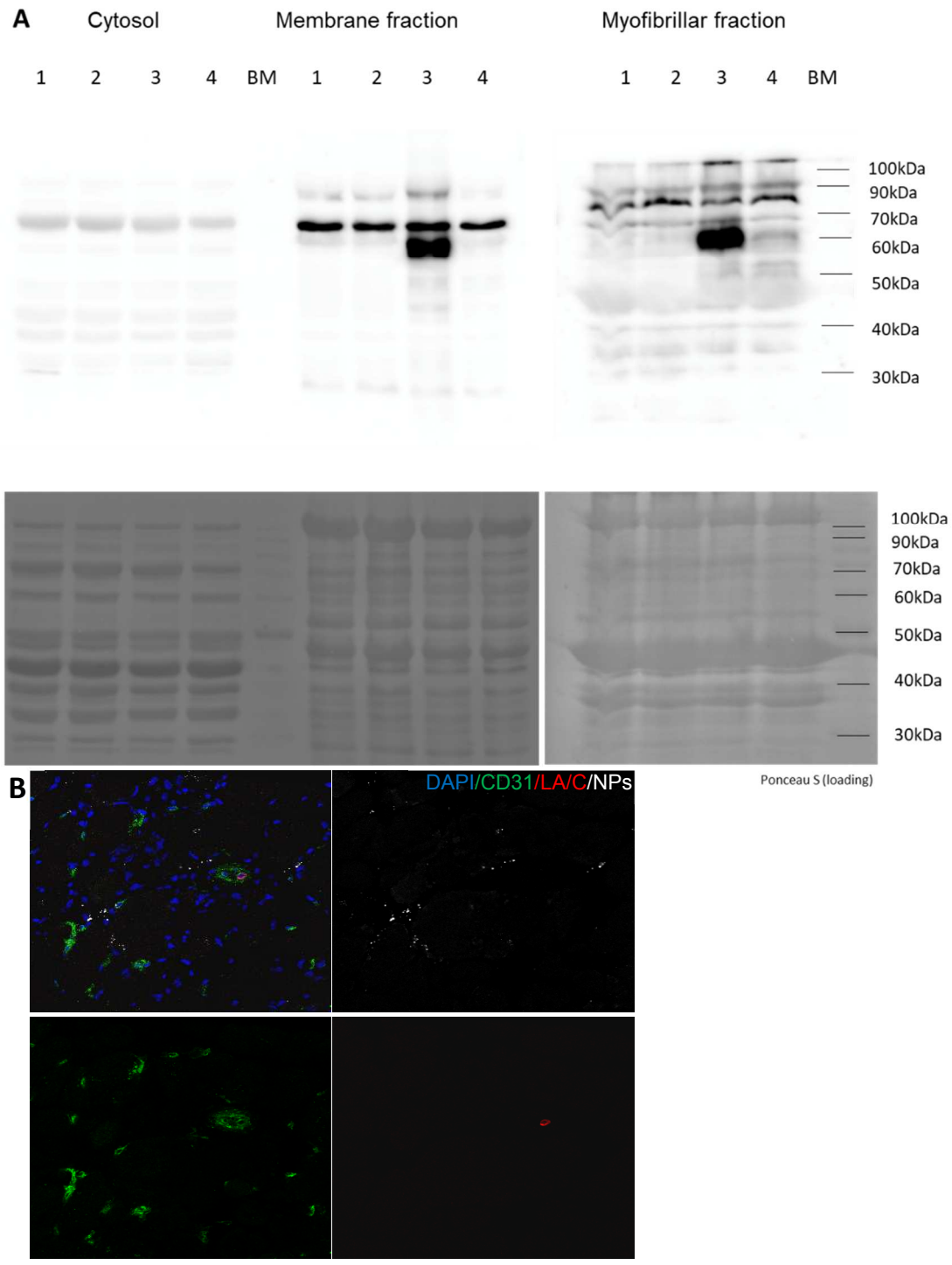

Figure 4-5: MSNP-HGF is retained in the muscle interstitium but does not enhance hiPSC-SMPC homing to muscle

A) Western blot analysis of fractionated quadriceps lysates at 24 hours after MSNP-HGF intramuscular injection; 1 – MSNP only, 2 – MSNP+Low HGF, 3 – MSNP+High HGF, 4 – free HGF, BM – BenchMark Protein Ladder.

B) hiPSC-SMPCs (LaminA/C, red) are detected inside blood vessels (CD31, green) delivered 24 hours after MSNP-HGF delivery.

CHAPTER 5: Conclusions

Stem cell based-therapeutic delivery to injured muscle offers great promise and potentially a life-long cure for degenerative diseases such as DMD, especially with work showing that a single SC is capable of self-renewal and repopulation of irradiated muscle after injury[14]. However, finding a cell able to self-renew derived from hPSCs is yet to be accomplished. Although progress has been made on directed differentiations of hPSCs to myogenic cultures, recent work has shown that hPSC derived myogenic cells give rise to SMPCs with a similar transcriptional profile of an embryonic to fetal SMPCs at developmental trajectory and is not equivalent to and adult SC[74,78]. Therefore, there are many challenges prior to moving cell-based therapies forward for muscle diseases including cellular immaturity[74], lack of ability to support self-renewal[14], lack of ability to reach multiple muscles and lack of ability to remain in the quiescence state needed for long-term repair in humans. However, this work and work from many others have shown that even when the gold-standard engraftable cell is generated and can be expanded to numbers needed to restore damaged muscle, the muscle microenvironment in degenerative diseases will still need to be taken into account[61,151,191,192].

We set out to understand two of the challenges mentioned above in greater detail in this work: the potential to reach multiple muscles after systemic delivery and the role that the diseased microenvironment might play in this context. Here we have demonstrated that SMPCs do not home efficiently to skeletal muscle upon their systemic delivery and were particularly inefficient in disease settings. We found that of the quantified systemically delivered cells, more SMPCs were detected inside in blood vessels in dystrophic and severely dystrophic gastrocnemius muscle cross-sections compared to healthy muscle. We speculate that the diseased states resulted in SMPCs adhering at higher frequency to blood vessel endothelial cells, particularly capillaries, in dystrophic and severely dystrophic muscles compared to healthy muscles. We further observed prominent clotting occurring in the severely dystrophic muscle upon systemic cell delivery that was not detectable in healthy or dystrophic muscles.

To further assess the disease states effect on SMPCs, future work would interrogate potential SMPC adhesion or interaction with the mouse ECs *in silico.*

At the single-cell level, we described differences in cellular composition between healthy, dystrophic and severely dystrophic gastrocnemius skeletal muscles. We showed that as the disease severity of DMD increases the prevalence of stromal cells and macrophages increases. These results are not surprising given the exacerbated TGF-□ activity in severely dystrophic environments[46–48,52], which prompted us to interrogate the intercellular communication between stromal cells and macrophages, and endothelial cells utilizing a computational method. ECs play a pivotal role in maintaining healthy muscle and we showed they become progressively more impaired as disease severity increases. ECs in DMD patients have been shown to be defective with EC swelling, increase in basement membrane of capillary ECs, and induction of platelet aggregation[93–95,193]. Therefore, it was imperative to investigate the differences between healthy, dystrophic and severely dystrophic ECs that may have caused systemic cell delivery differences. We have found that in a severely dystrophic environment, ECs upregulate the expression of several ECM genes including collagen I, IV and fibronectin. We further found an increased colocalization of the EC marker CD31 and the procoagulant protein PAI1, further confirming EC impairment. We found thickened collagen IV around capillaries and increased PAI1 expression on human DMD muscle cross-sections (n=1, data not shown). This is important because even if cells can be engineered to extravasate, the disease state will still need to be considered for therapeutic applications.

Collectively, our results indicate clear EC impairment in severely dystrophic muscles. Consequently, for future systemic cell-based therapeutics, EC impairment needs to be considered in the context of DMD disease severity. Perhaps overexpressing components needed to enable cells to escape ECs into the surrounding muscle as is done routinely in leukocytes will be a valuable avenue for future exploration, however, the disease severity and diseased muscle microenvironment needs to be taken into consideration to prevent cell fate change or cell death after entry into the dystrophic muscle microenvironments. Perhaps clinical trials delivering different muscle progenitor cells, such as mesoangioblasts and muscle

derived CD133+, ultimately failed because careful consideration of the muscle microenvironment and EC impairment in DMD patients were not considered [108,109]. Furthermore, future intramuscular cell engraftment studies need to be guided by the finding that stromal cells and macrophages heterogeneity increases as the severity of the DMD disease increase, which indicate that other players in the muscle will likely affect the engrafted cells. Potentially, a combination approach for cell-based therapeutics is to be considered for future investigations. For example, cells can be transplanted with pharmacological drugs proven to either reduce fibrosis, or inflammation, or TGF-□ signaling[194–196]. In summary, this body of work provides insights on cell population differences, transcriptional changes in dystrophic disease states, and increases the understanding of cross talk between endothelial cells and other muscle-resident cell populations which can be utilized for future interventions and manipulations of the muscle microenvironment for cell-based therapeutic applications for DMD.

REFERENCES

1 Joe AWB, Yi L, Natarajan A, Grand FL, So L, Wang J, *et al.* Muscle injury activates resident fibro/adipogenic progenitors that facilitate myogenesis. *Nat Cell Biol* 2010;12:153–63. https://doi.org/10.1038/ncb2015.

2 Schultz E, Gibson MC, Champion T. Satellite cells are mitotically quiescent in mature mouse muscle: An EM and radioautographic study. *J Exp Zool* 1978;206:451–6. https://doi.org/10.1002/jez.1402060314.

3 Mauro A. Satellite Cell Of Skeletal Muscle Fibers. *J Cell Biology* 1961;9:493–5. https://doi.org/10.1083/jcb.9.2.493.

4 Cheung TH, Rando TA. Molecular regulation of stem cell quiescence. *Nat Rev Mol Cell Bio* 2013;14:329–40. https://doi.org/10.1038/nrm3591.

5 Seale P, Sabourin LA, Girgis-Gabardo A, Mansouri A, Gruss P, Rudnicki MA. Pax7 Is Required for the Specification of Myogenic Satellite Cells. *Cell* 2000;102:777–86. https://doi.org/10.1016/s0092-8674(00)00066-0.

6 Tajbakhsh S. Skeletal muscle stem cells in developmental versus regenerative myogenesis. *J Intern Med* 2009;266:372–89. https://doi.org/10.1111/j.1365-2796.2009.02158.x.

7 Zammit PS, Heslop L, Hudon V, Rosenblatt JD, Tajbakhsh S, Buckingham ME, *et al.* Kinetics of Myoblast Proliferation Show That Resident Satellite Cells Are Competent to Fully Regenerate Skeletal Muscle Fibers. *Exp Cell Res* 2002;281:39–49. https://doi.org/10.1006/excr.2002.5653.

8 Kitzmann M, Carnac G, Vandromme M, Primig M, Lamb NJC, Fernandez A. The Muscle Regulatory Factors MyoD and Myf-5 Undergo Distinct Cell Cycle–specific Expression in Muscle Cells. *J Cell Biology* 1998;142:1447–59. https://doi.org/10.1083/jcb.142.6.1447.

9 Zammit PS, Relaix F, Nagata Y, Ruiz AP, Collins CA, Partridge TA, *et al.* Pax7 and myogenic progression in skeletal muscle satellite cells. *J Cell Sci* 2006;119:1824–32. https://doi.org/10.1242/jcs.02908.

10 Abou-Khalil R, Grand FL, Pallafacchina G, Valable S, Authier F-J, Rudnicki MA, *et al.* Autocrine and Paracrine Angiopoietin 1/Tie-2 Signaling Promotes Muscle Satellite Cell Self-Renewal. *Cell Stem Cell* 2009;5:298–309. https://doi.org/10.1016/j.stem.2009.06.001.

11 Shea KL, Xiang W, LaPorta VS, Licht JD, Keller C, Basson MA, *et al.* Sprouty1 Regulates Reversible Quiescence of a Self-Renewing Adult Muscle Stem Cell Pool during Regeneration. *Cell Stem Cell* 2010;6:117–29. https://doi.org/10.1016/j.stem.2009.12.015.

12 Kuang S, Kuroda K, Grand FL, Rudnicki MA. Asymmetric Self-Renewal and Commitment of Satellite Stem Cells in Muscle. *Cell* 2007;129:999–1010. https://doi.org/10.1016/j.cell.2007.03.044.

13 Moss FP, Leblond CP. Satellite cells as the source of nuclei in muscles of growing rats. *Anatomical Rec* 1971;170:421–35. https://doi.org/10.1002/ar.1091700405.

14 Sacco A, Doyonnas R, Kraft P, Vitorovic S, Blau HM. Self-renewal and expansion of single transplanted muscle stem cells. *Nature* 2008;456:502–6. https://doi.org/10.1038/nature07384.

15 Tang F, Barbacioru C, Wang Y, Nordman E, Lee C, Xu N, *et al.* mRNA-Seq whole-transcriptome analysis of a single cell. *Nat Methods* 2009;6:377–82. https://doi.org/10.1038/nmeth.1315.

16 Zheng GXY, Terry JM, Belgrader P, Ryvkin P, Bent ZW, Wilson R, *et al.* Massively parallel digital transcriptional profiling of single cells. *Nat Commun* 2017;8:14049. https://doi.org/10.1038/ncomms14049.

17 Ziegenhain C, Vieth B, Parekh S, Reinius B, Guillaumet-Adkins A, Smets M, *et al.* Comparative Analysis of Single-Cell RNA Sequencing Methods. *Mol Cell* 2017;65:631-643.e4. https://doi.org/10.1016/j.molcel.2017.01.023.

18 Picelli S, Faridani OR, Björklund ÅK, Winberg G, Sagasser S, Sandberg R. Full-length RNA-seq from single cells using Smart-seq2. *Nat Protoc* 2014;9:171–81. https://doi.org/10.1038/nprot.2014.006.

19 Sasagawa Y, Danno H, Takada H, Ebisawa M, Tanaka K, Hayashi T, *et al.* Quartz-Seq2: a high-throughput single-cell RNA-sequencing method that effectively uses limited sequence reads. *Genome Biol* 2018;19:29. https://doi.org/10.1186/s13059-018-1407-3.

20 Cho DS, Doles JD. Single cell transcriptome analysis of muscle satellite cells reveals widespread transcriptional heterogeneity. *Gene* 2017;636:54–63. https://doi.org/10.1016/j.gene.2017.09.014.

21 Schaum N, Karkanias J, Neff NF, May AP, Quake SR, Wyss-Coray T, *et al.* Single-cell transcriptomics of 20 mouse organs creates a Tabula Muris. *Nature* 2018;562:367–72. https://doi.org/10.1038/s41586-018-0590-4.

22 Giordani L, He GJ, Negroni E, Sakai H, Law JYC, Siu MM, *et al.* High-Dimensional Single-Cell Cartography Reveals Novel Skeletal Muscle-Resident Cell Populations. *Mol Cell* 2019;74:609-621.e6. https://doi.org/10.1016/j.molcel.2019.02.026.

23 Micheli AJD, Laurilliard EJ, Heinke CL, Ravichandran H, Fraczek P, Soueid-Baumgarten S, *et al.* Single-Cell Analysis of the Muscle Stem Cell Hierarchy Identifies Heterotypic Communication Signals Involved in Skeletal Muscle Regeneration. *Cell Reports* 2020;30:3583-3595.e5. https://doi.org/10.1016/j.celrep.2020.02.067.

24 Oprescu SN, Yue F, Qiu J, Brito LF, Kuang S. Temporal Dynamics and Heterogeneity of Cell Populations during Skeletal Muscle Regeneration. *Iscience* 2020;23:100993. https://doi.org/10.1016/j.isci.2020.100993.

25 Dell'Orso S, Juan AH, Ko K-D, Naz F, Perovanovic J, Gutierrez-Cruz G, *et al.* Single cell analysis of adult mouse skeletal muscle stem cells in homeostatic and regenerative conditions. *Development* 2019;146:dev174177. https://doi.org/10.1242/dev.174177.

26 Camps J, Breuls N, Sifrim A, Giarratana N, Corvelyn M, Danti L, *et al.* Interstitial Cell Remodeling Promotes Aberrant Adipogenesis in Dystrophic Muscles. *Cell Reports* 2020;31:107597. https://doi.org/10.1016/j.celrep.2020.107597.

27 Moat SJ, Bradley DM, Salmon R, Clarke A, Hartley L. Newborn bloodspot screening for Duchenne Muscular Dystrophy: 21 years experience in Wales (UK). *Eur J Hum Genet* 2013;21:1049–53. https://doi.org/10.1038/ejhg.2012.301.

28 Mendell JR, Shilling C, Leslie ND, Flanigan KM, al-Dahhak R, Gastier-Foster J, *et al.* Evidence-based path to newborn screening for duchenne muscular dystrophy. *Ann Neurol* 2012;71:304–13. https://doi.org/10.1002/ana.23528.

29 Mendell JR, Lloyd□Puryear M. Report of MDA muscle disease symposium on newborn screening for Duchenne muscular dystrophy. *Muscle Nerve* 2013;48:21–6. https://doi.org/10.1002/mus.23810.

30 Hoffman EP, Brown RH, Kunkel LM. Dystrophin: The protein product of the duchenne muscular dystrophy locus. *Cell* 1987;51:919–28. https://doi.org/10.1016/0092-8674(87)90579-4.

31 Ervasti J, Campbell K. A role for the dystrophin-glycoprotein complex as a transmembrane linker between laminin and actin. *J Cell Biology* 1993;122:809–23. https://doi.org/10.1083/jcb.122.4.809.

32 Campbell KP, Kahl SD. Association of dystrophin and an integral membrane glycoprotein. *Nature* 1989;338:259–62. https://doi.org/10.1038/338259a0.

33 Hoffman EP, Brown RH, Kunkel LM. Dystrophin: The protein product of the duchenne muscular dystrophy locus. *Cell* 1987;51:919–28. https://doi.org/10.1016/0092-8674(87)90579-4.

34 Yoshida M, Ozawa E. Glycoprotein complex anchoring dystrophin to sarcolemma. *J Biochem* 1990;108:748–52. https://doi.org/10.1093/oxfordjournals.jbchem.a123276.

35 Koenig M, Monaco AP, Kunkel LM. The complete sequence of dystrophin predicts a rod-shaped cytoskeletal protein. *Cell* 1988;53:219–28. https://doi.org/10.1016/0092-8674(88)90383-2.

36 Webster C, Blau HM. Accelerated age-related decline in replicative life-span of Duchenne muscular dystrophy myoblasts: Implications for cell and gene therapy. *Somat Cell Molec Gen* 1990;16:557–65. https://doi.org/10.1007/bf01233096.

37 Sacco A, Mourkioti F, Tran R, Choi J, Llewellyn M, Kraft P, *et al.* Short Telomeres and Stem Cell Exhaustion Model Duchenne Muscular Dystrophy in mdx/mTR Mice. *Cell* 2010;143:1059–71. https://doi.org/10.1016/j.cell.2010.11.039.

38 Dumont NA, Wang YX, Maltzahn J von, Pasut A, Bentzinger CF, Brun CE, *et al.* Dystrophin expression in muscle stem cells regulates their polarity and asymmetric division. *Nat Med* 2015;21:1455–63. https://doi.org/10.1038/nm.3990.

39 Klingler W, Jurkat-Rott K, Lehmann-Horn F, Schleip R. The role of fibrosis in Duchenne muscular dystrophy. *Acta Myologica Myopathies Cardiomyopathies Official J Mediterr Soc Myology* 2012;31:184–95.

40 Bushby K, Finkel R, Birnkrant DJ, Case LE, Clemens PR, Cripe L, *et al.* Diagnosis and management of Duchenne muscular dystrophy, part 1: diagnosis, and pharmacological and psychosocial management. *Lancet Neurology* 2010;9:77–93. https://doi.org/10.1016/s1474-4422(09)70271-6.

41 Bulfield G, Siller WG, Wight PA, Moore KJ. X chromosome-linked muscular dystrophy (mdx) in the mouse. *P Natl Acad Sci Usa* 1984;81:1189–92. https://doi.org/10.1073/pnas.81.4.1189.

42 Sicinski P, Geng Y, Ryder-Cook AS, Barnard EA, Darlison MG, Barnard PJ. The Molecular Basis of Muscular Dystrophy in the mdx Mouse: a Point Mutation. *Science* 1989;244:1578–80. https://doi.org/10.1126/science.2662404.

43 DiMario JX, Uzman A, Strohman RC. Fiber regeneration is not persistent in dystrophic (mdx) mouse skeletal muscle. *Dev Biol* 1991;148:314–21. https://doi.org/10.1016/0012-1606(91)90340-9.

44 COULTON GR, MORGAN JE, PARTRIDGE TA, SLOPER JC. THE mdx MOUSE SKELETAL MUSCLE MYOPATHY: I. A HISTOLOGICAL, MORPHOMETRIC AND BIOCHEMICAL INVESTIGATION. *Neuropath Appl Neuro* 1988;14:53–70. https://doi.org/10.1111/j.1365-2990.1988.tb00866.x.

45 Carnwath JW, Shotton DM. Muscular dystrophy in the mdx mouse: Histopathology of the soleus and extensor digitorum longus muscles. *J Neurol Sci* 1987;80:39–54. https://doi.org/10.1016/0022-510x(87)90219-x.

46 Fukada S, Morikawa D, Yamamoto Y, Yoshida T, Sumie N, Yamaguchi M, *et al.* Genetic Background Affects Properties of Satellite Cells and mdx Phenotypes. *Am J Pathology* 2010;176:2414–24. https://doi.org/10.2353/ajpath.2010.090887.

47 Heydemann A, Ceco E, Lim JE, Hadhazy M, Ryder P, Moran JL, *et al.* Latent TGF-β–binding protein 4 modifies muscular dystrophy in mice. *J Clin Invest* 2009;119:3703–12. https://doi.org/10.1172/jci39845.

48 Swaggart KA, Demonbreun AR, Vo AH, Swanson KE, Kim EY, Fahrenbach JP, *et al.* Annexin A6 modifies muscular dystrophy by mediating sarcolemmal repair. *Proc National Acad Sci* 2014;111:6004–9. https://doi.org/10.1073/pnas.1324242111.

49 Quattrocelli M, Capote J, Ohiri JC, Warner JL, Vo AH, Earley JU, *et al.* Genetic modifiers of muscular dystrophy act on sarcolemmal resealing and recovery from injury. *Plos Genet* 2017;13:e1007070. https://doi.org/10.1371/journal.pgen.1007070.

50 Capote J, Kramerova I, Martinez L, Vetrone S, Barton ER, Sweeney HL, *et al.* Osteopontin ablation ameliorates muscular dystrophy by shifting macrophages to a pro-regenerative phenotype. *J Cell Biology* 2016;213:275–88. https://doi.org/10.1083/jcb.201510086.

51 Hammers DW, Hart CC, Matheny MK, Wright LA, Armellini M, Barton ER, *et al.* The D2.mdx mouse as a preclinical model of the skeletal muscle pathology associated with Duchenne muscular dystrophy. *Sci Rep-Uk* 2020;10:14070. https://doi.org/10.1038/s41598-020-70987-y.

52 Mázala DAG, Novak JS, Hogarth MW, Nearing M, Adusumalli P, Tully CB, *et al.* TGF-β–driven muscle degeneration and failed regeneration underlie disease onset in a DMD mouse model. *Jci Insight* 2020;5:e135703. https://doi.org/10.1172/jci.insight.135703.

53 Partridge TA, Morgan JE, Coulton GR, Hoffman EP, Kunkel LM. Conversion of mdx myofibres from dystrophin-negative to -positive by injection of normal myoblasts. *Nature* 1989;337:176–9. https://doi.org/10.1038/337176a0.

54 Huard J, Bouchard JP, Roy R, Malouin F, Dansereau G, Labrecque C, *et al.* Human myoblast transplantation: Preliminary results of 4 cases. *Muscle Nerve* 1992;15:550–60. https://doi.org/10.1002/mus.880150504.

55 Gussoni E, Pavlath GK, Lanctot AM, Sharma KR, Miller RG, Steinman L, *et al.* Normal dystrophin transcripts detected in Duchenne muscular dystrophy patients after myoblast transplantation. *Nature* 1992;356:435–8. https://doi.org/10.1038/356435a0.

56 Karpati G, Ajdukovic D, Arnold D, Gledhill RB, Guttmann R, Holland P, *et al.* Myoblast transfer in duchenne muscular dystrophy. *Ann Neurol* 1993;34:8–17. https://doi.org/10.1002/ana.410340105.

57 Gussoni E, Blau HM, Kunkel LM. The fate of individual myoblasts after transplantation into muscles of DMD patients. *Nat Med* 1997;3:970–7. https://doi.org/10.1038/nm0997-970.

58 Law PK, Goodwin TG, Fang Q, Chen M, Li H, Florendo JA, *et al.* Myoblast Transfer Therapy for Duchenne Muscular Dystrophy. *Pediatr Int* 1991;33:206–15. https://doi.org/10.1111/j.1442-200x.1991.tb01545.x.

59 Miller RG, Sharma KR, Pavlath GK, Gussoni E, Mynhier M, Yu P, *et al.* Myoblast implantation in Duchenne muscular dystrophy: The San Francisco study. *Muscle Nerve* 1997;20:469–78. https://doi.org/10.1002/(sici)1097-4598(199704)20:4<469::aid-mus10>3.0.co;2-u.

60 Charville GW, Cheung TH, Yoo B, Santos PJ, Lee GK, Shrager JB, *et al.* Ex Vivo Expansion and In Vivo Self-Renewal of Human Muscle Stem Cells. *Stem Cell Rep* 2015;5:621–32. https://doi.org/10.1016/j.stemcr.2015.08.004.

61 Tierney MT, Gromova A, Sesillo FB, Sala D, Spenlé C, Orend G, *et al.* Autonomous Extracellular Matrix Remodeling Controls a Progressive Adaptation in Muscle Stem Cell Regenerative Capacity during Development. *Cell Reports* 2016;14:1940–52. https://doi.org/10.1016/j.celrep.2016.01.072.

62 Sakai H, Sato T, Sakurai H, Yamamoto T, Hanaoka K, Montarras D, *et al.* Fetal Skeletal Muscle Progenitors Have Regenerative Capacity after Intramuscular Engraftment in Dystrophin Deficient Mice. *Plos One* 2013;8:e63016. https://doi.org/10.1371/journal.pone.0063016.

63 Xu X, Wilschut KJ, Kouklis G, Tian H, Hesse R, Garland C, *et al.* Human Satellite Cell Transplantation and Regeneration from Diverse Skeletal Muscles. *Stem Cell Rep* 2015;5:419–34. https://doi.org/10.1016/j.stemcr.2015.07.016.

64 Hicks MR, Hiserodt J, Paras K, Fujiwara W, Eskin A, Jan M, *et al.* ERBB3 and NGFR mark a distinct skeletal muscle progenitor cell in human development and hPSCs. *Nat Cell Biol* 2018;20:46–57. https://doi.org/10.1038/s41556-017-0010-2.

65 Ehrhardt J, Brimah K, Adkin C, Partridge T, Morgan J. Human muscle precursor cells give rise to functional satellite cells in vivo. *Neuromuscular Disord* 2007;17:631–8. https://doi.org/10.1016/j.nmd.2007.04.009.

66 Chal J, Pourquié O. Making muscle: skeletal myogenesis in vivo and in vitro. *Development* 2017;144:2104–22. https://doi.org/10.1242/dev.151035.

67 Sambasivan R, Tajbakhsh S. Skeletal muscle stem cell birth and properties. *Semin Cell Dev Biol* 2007;18:870–82. https://doi.org/10.1016/j.semcdb.2007.09.013.

68 Sakai H, Sato T, Sakurai H, Yamamoto T, Hanaoka K, Montarras D, *et al.* Fetal Skeletal Muscle Progenitors Have Regenerative Capacity after Intramuscular Engraftment in Dystrophin Deficient Mice. *Plos One* 2013;8:e63016. https://doi.org/10.1371/journal.pone.0063016.

69 Collins CA, Olsen I, Zammit PS, Heslop L, Petrie A, Partridge TA, *et al.* Stem Cell Function, Self-Renewal, and Behavioral Heterogeneity of Cells from the Adult Muscle Satellite Cell Niche. *Cell* 2005;122:289–301. https://doi.org/10.1016/j.cell.2005.05.010.

70 Cerletti M, Jurga S, Witczak CA, Hirshman MF, Shadrach JL, Goodyear LJ, *et al.* Highly Efficient, Functional Engraftment of Skeletal Muscle Stem Cells in Dystrophic Muscles. *Cell* 2008;134:37–47. https://doi.org/10.1016/j.cell.2008.05.049.

71 Skuk D, Paradis M, Goulet M, Chapdelaine P, Rothstein DM, Tremblay JP. Intramuscular Transplantation of Human Postnatal Myoblasts Generates Functional Donor-Derived Satellite Cells. *Mol Ther* 2010;18:1689–97. https://doi.org/10.1038/mt.2010.128.

72 Alexander MS, Rozkalne A, Colletta A, Spinazzola JM, Johnson S, Rahimov F, *et al.* CD82 Is a Marker for Prospective Isolation of Human Muscle Satellite Cells and Is Linked to Muscular Dystrophies. *Cell Stem Cell* 2016;19:800–7. https://doi.org/10.1016/j.stem.2016.08.006.

73 Takahashi K, Yamanaka S. Induction of Pluripotent Stem Cells from Mouse Embryonic and Adult Fibroblast Cultures by Defined Factors. *Cell* 2006;126:663–76. https://doi.org/10.1016/j.cell.2006.07.024.

74 Xi H, Langerman J, Sabri S, Chien P, Young CS, Younesi S, *et al.* A Human Skeletal Muscle Atlas Identifies the Trajectories of Stem and Progenitor Cells across Development and from Human Pluripotent Stem Cells. *Cell Stem Cell* 2020;27:181–5. https://doi.org/10.1016/j.stem.2020.06.006.

75 Barberi T, Bradbury M, Dincer Z, Panagiotakos G, Socci ND, Studer L. Derivation of engraftable skeletal myoblasts from human embryonic stem cells. *Nat Med* 2007;13:642–8. https://doi.org/10.1038/nm1533.

76 Goudenege S, Lebel C, Huot NB, Dufour C, Fujii I, Gekas J, *et al.* Myoblasts Derived From Normal hESCs and Dystrophic hiPSCs Efficiently Fuse With Existing Muscle Fibers Following Transplantation. *Mol Ther* 2012;20:2153–67. https://doi.org/10.1038/mt.2012.188.

77 Darabi R, Arpke RW, Irion S, Dimos JT, Grskovic M, Kyba M, *et al.* Human ES- and iPS-Derived Myogenic Progenitors Restore DYSTROPHIN and Improve Contractility upon Transplantation in Dystrophic Mice. *Cell Stem Cell* 2012;10:610–9. https://doi.org/10.1016/j.stem.2012.02.015.

78 Xi H, Fujiwara W, Gonzalez K, Jan M, Liebscher S, Handel BV, *et al.* In Vivo Human Somitogenesis Guides Somite Development from hPSCs. *Cell Reports* 2017;18:1573–85. https://doi.org/10.1016/j.celrep.2017.01.040.

79 Chal J, Oginuma M, Tanoury ZA, Gobert B, Sumara O, Hick A, *et al.* Differentiation of pluripotent stem cells to muscle fiber to model Duchenne muscular dystrophy. *Nat Biotechnol* 2015;33:962–9. https://doi.org/10.1038/nbt.3297.

80 Chal J, Tanoury ZA, Hestin M, Gobert B, Aivio S, Hick A, *et al.* Generation of human muscle fibers and satellite-like cells from human pluripotent stem cells in vitro. *Nat Protoc* 2016;11:1833–50. https://doi.org/10.1038/nprot.2016.110.

81 Shelton M, Kocharyan A, Liu J, Skerjanc IS, Stanford WL. Robust generation and expansion of skeletal muscle progenitors and myocytes from human pluripotent stem cells. *Methods* 2016;101:73–84. https://doi.org/10.1016/j.ymeth.2015.09.019.

82 Borchin B, Chen J, Barberi T. Derivation and FACS-Mediated Purification of PAX3+/PAX7+ Skeletal Muscle Precursors from Human Pluripotent Stem Cells. *Stem Cell Rep* 2013;1:620–31. https://doi.org/10.1016/j.stemcr.2013.10.007.

83 Magli A, Incitti T, Kiley J, Swanson SA, Darabi R, Rinaldi F, *et al.* PAX7 Targets, CD54, Integrin α9β1, and SDC2, Allow Isolation of Human ESC/iPSC-Derived Myogenic Progenitors. *Cell Reports* 2017;19:2867–77. https://doi.org/10.1016/j.celrep.2017.06.005.

84 Wu J, Matthias N, Lo J, Ortiz-Vitali JL, Shieh AW, Wang SH, *et al.* A Myogenic Double-Reporter Human Pluripotent Stem Cell Line Allows Prospective Isolation of Skeletal Muscle Progenitors. *Cell Reports* 2018;25:1966-1981.e4. https://doi.org/10.1016/j.celrep.2018.10.067.

85 Schmalbruch H. The morphology of regeneration of skeletal muscles in the rat. *Tissue Cell* 1976;8:673–92. https://doi.org/10.1016/0040-8166(76)90039-2.

86 Christov C, Chrétien F, Abou-Khalil R, Bassez G, Vallet G, Authier F-J, *et al.* Muscle Satellite Cells and Endothelial Cells: Close Neighbors and Privileged Partners. *Mol Biol Cell* 2007;18:1397–409. https://doi.org/10.1091/mbc.e06-08-0693.

87 Verma M, Asakura Y, Murakonda BSR, Pengo T, Latroche C, Chazaud B, *et al.* Muscle Satellite Cell Cross-Talk with a Vascular Niche Maintains Quiescence via VEGF and Notch Signaling. *Cell Stem Cell* 2018;23:530-543.e9. https://doi.org/10.1016/j.stem.2018.09.007.

88 Krüger-Genge A, Blocki A, Franke R-P, Jung F. Vascular Endothelial Cell Biology: An Update. *Int J Mol Sci* 2019;20:4411. https://doi.org/10.3390/ijms20184411.

89 Abou-Khalil R, Mounier R, Chazaud B. Regulation of myogenic stem cell behavior by vessel cells: the "ménage à trois" of satellite cells, periendothelial cells and endothelial cells. *Cell Cycle Georget Tex* 2010;9:892–6. https://doi.org/10.4161/cc.9.5.10851.

90 Fan Z, Turiel G, Ardicoglu R, Ghobrial M, Masschelein E, Kocijan T, *et al.* Exercise-induced angiogenesis is dependent on metabolically primed ATF3/4+ endothelial cells. *Cell Metab* 2021;33:1793-1807.e9. https://doi.org/10.1016/j.cmet.2021.07.015.

91 Kalucka J, Rooij LPMH de, Goveia J, Rohlenova K, Dumas SJ, Meta E, *et al.* Single-Cell Transcriptome Atlas of Murine Endothelial Cells. *Cell* 2020;180:764-779.e20. https://doi.org/10.1016/j.cell.2020.01.015.

92 Tombor LS, John D, Glaser SF, Luxán G, Forte E, Furtado M, *et al.* Single cell sequencing reveals endothelial plasticity with transient mesenchymal activation after myocardial infarction. *Nat Commun* 2021;12:681. https://doi.org/10.1038/s41467-021-20905-1.

93 Miike T, Sugino S, Ohtani Y, Taku K, Yoshioka K. Vascular endothelial cell injury and platelet embolism in Duchenne muscular dystrophy at the preclinical stage. *J Neurol Sci* 1987;82:67–80. https://doi.org/10.1016/0022-510x(87)90007-4.

94 KOBAYASHI Y, SUZUKI H, IINUMA K, TADA K, YAMAMOTO TY. Endothelial Alterations of Skeletal Muscle Capillaries in Childhood Myopathies. *Tohoku J Exp Medicine* 1983;140:381–9. https://doi.org/10.1620/tjem.140.381.

95 JERUSALEM F, ENGEL AG, GOMEZ MR. DUCHENNE DYSTROPHY: I. MORPHOMETRIC STUDY OF THE MUSCLE MICROVASCULATURE. *Brain* 1974;97:115–22. https://doi.org/10.1093/brain/97.1.115.

96 Latroche C, Matot B, Martins-Bach A, Briand D, Chazaud B, Wary C, *et al.* Structural and Functional Alterations of Skeletal Muscle Microvasculature in Dystrophin-Deficient mdx Mice. *Am J Pathology* 2015;185:2482–94. https://doi.org/10.1016/j.ajpath.2015.05.009.

97 Podkalicka P, Mucha O, Kaziród K, Bronisz-Budzyńska I, Ostrowska-Paton S, Tomczyk M, *et al.* Age-Dependent Dysregulation of Muscle Vasculature and Blood Flow Recovery after Hindlimb Ischemia in the mdx Model of Duchenne Muscular Dystrophy. *Biomed* 2021;9:481. https://doi.org/10.3390/biomedicines9050481.

98 Palladino M, Gatto I, Neri V, Straino S, Smith RC, Silver M, *et al.* Angiogenic Impairment of the Vascular Endothelium. *Arteriosclerosis Thrombosis Vasc Biology* 2013;33:2867–76. https://doi.org/10.1161/atvbaha.112.301172.

99 Meng J, Chun S, Asfahani R, Lochmüller H, Muntoni F, Morgan J. Human Skeletal Muscle–derived CD133+ Cells Form Functional Satellite Cells After Intramuscular Transplantation in Immunodeficient Host Mice. *Mol Ther* 2014;22:1008–17. https://doi.org/10.1038/mt.2014.26.

100 Negroni E, Riederer I, Chaouch S, Belicchi M, Razini P, Santo JD, *et al.* In Vivo Myogenic Potential of Human CD133+ Muscle-derived Stem Cells: A Quantitative Study. *Mol Ther* 2009;17:1771–8. https://doi.org/10.1038/mt.2009.167.

101 Benchaouir R, Meregalli M, Farini A, D'Antona G, Belicchi M, Goyenvalle A, *et al.* Restoration of Human Dystrophin Following Transplantation of Exon-Skipping-Engineered DMD Patient Stem Cells into Dystrophic Mice. *Cell Stem Cell* 2007;1:646–57. https://doi.org/10.1016/j.stem.2007.09.016.

102 Angelis LD, Berghella L, Coletta M, Lattanzi L, Zanchi M, Gabriella M, *et al.* Skeletal Myogenic Progenitors Originating from Embryonic Dorsal Aorta Coexpress Endothelial and Myogenic Markers and Contribute to Postnatal Muscle Growth and Regeneration. *J Cell Biology* 1999;147:869–78. https://doi.org/10.1083/jcb.147.4.869.

103 Minasi MG, Riminucci M, Angelis LD, Borello U, Berarducci B, Innocenzi A, *et al.* The meso-angioblast: a multipotent, self-renewing cell that originates from the dorsal aorta and differentiates into most mesodermal tissues. *Dev Camb Engl* 2002;129:2773–83. https://doi.org/10.1242/dev.129.11.2773.

104 Tonlorenzi R, Dellavalle A, Schnapp E, Cossu G, Sampaolesi M. Isolation and Characterization of Mesoangioblasts from Mouse, Dog, and Human Tissues. *Curr Protoc Stem Cell Biology* 2007;3:2B.1.1-2B.1.29. https://doi.org/10.1002/9780470151808.sc02b01s3.

105 Guttinger M, Tafi E, Battaglia M, Coletta M, Cossu G. Allogeneic mesoangioblasts give rise to alpha-sarcoglycan expressing fibers when transplanted into dystrophic mice. *Exp Cell Res* 2006;312:3872–9. https://doi.org/10.1016/j.yexcr.2006.08.012.

106 Sampaolesi M, Torrente Y, Innocenzi A, Tonlorenzi R, D'Antona G, Pellegrino MA, *et al.* Cell Therapy of α-Sarcoglycan Null Dystrophic Mice Through Intra-Arterial Delivery of Mesoangioblasts. *Science* 2003;301:487–92. https://doi.org/10.1126/science.1082254.

107 Sampaolesi M, Blot S, D'Antona G, Granger N, Tonlorenzi R, Innocenzi A, *et al.* Mesoangioblast stem cells ameliorate muscle function in dystrophic dogs. *Nature* 2006;444:574–9. https://doi.org/10.1038/nature05282.

108 Torrente Y, Belicchi M, Marchesi C, D'antona G, Cogiamanian F, Pisati F, *et al.* Autologous Transplantation of Muscle-Derived CD133+ Stem Cells in Duchenne Muscle Patients. *Cell Transplant* 2007;16:563–77. https://doi.org/10.3727/000000007783465064.

109 Cossu G, Previtali SC, Napolitano S, Cicalese MP, Tedesco FS, Nicastro F, *et al.* Intra□arterial transplantation of HLA□matched donor mesoangioblasts in Duchenne muscular dystrophy. *Embo Mol Med* 2015;7:1513–28. https://doi.org/10.15252/emmm.201505636.

110 Matthias N, Hunt SD, Wu J, Darabi R. Skeletal muscle perfusion and stem cell delivery in muscle disorders using intra-femoral artery canulation in mice. *Exp Cell Res* 2015;339:103–11. https://doi.org/10.1016/j.yexcr.2015.08.018.

111 Gerli MFM, Maffioletti SM, Millet Q, Tedesco FS. Transplantation of induced pluripotent stem cell-derived mesoangioblast-like myogenic progenitors in mouse models of muscle regeneration. *J Vis Exp Jove* 2014:e50532. https://doi.org/10.3791/50532.

112 Tedesco FS, Gerli MFM, Perani L, Benedetti S, Ungaro F, Cassano M, *et al.* Transplantation of Genetically Corrected Human iPSC-Derived Progenitors in Mice with Limb-Girdle Muscular Dystrophy. *Sci Transl Med* 2012;4:140ra89. https://doi.org/10.1126/scitranslmed.3003541.

113 Abdellatif AAH, Alsowinea AF. Approved and marketed nanoparticles for disease targeting and applications in COVID-19. *Nanotechnol Rev* 2021;10:1941–77. https://doi.org/10.1515/ntrev-2021-0115.

114 Mai WX, Meng H. Mesoporous silica nanoparticles: A multifunctional nano therapeutic system. *Integr Biology Quantitative Biosci Nano Macro* 2013;5:19–28. https://doi.org/10.1039/c2ib20137b.

115 Negishi Y, Ishii Y, Shiono H, Akiyama S, Sekine S, Kojima T, *et al.* Bubble Liposomes and Ultrasound Exposure Improve Localized Morpholino Oligomer Delivery into the Skeletal Muscles of Dystrophic mdx Mice. *Mol Pharmaceut* 2014;11:1053–61. https://doi.org/10.1021/mp4004755.

116 Rimessi P, Sabatelli P, Fabris M, Braghetta P, Bassi E, Spitali P, *et al.* Cationic PMMA Nanoparticles Bind and Deliver Antisense Oligoribonucleotides Allowing Restoration of Dystrophin Expression in the mdx Mouse. *Mol Ther* 2009;17:820–7. https://doi.org/10.1038/mt.2009.8.

117 Wang M, Wu B, Lu P, Tucker JD, Milazi S, Shah SN, *et al.* Pluronic–PEI copolymers enhance exon-skipping of 2′-O-methyl phosphorothioate oligonucleotide in cell culture and dystrophic mdx mice. *Gene Ther* 2014;21:52–9. https://doi.org/10.1038/gt.2013.57.

118 Perez AL, Bachrach E, Illigens BMW, Jun SJ, Bagden E, Steffen L, *et al.* CXCR4 enhances engraftment of muscle progenitor cells. *Muscle Nerve* 2009;40:562–72. https://doi.org/10.1002/mus.21317.

119 Sambasivan R, Yao R, Kissenpfennig A, Wittenberghe LV, Paldi A, Gayraud-Morel B, *et al.* Pax7-expressing satellite cells are indispensable for adult skeletal muscle regeneration. *Development* 2011;138:3647–56. https://doi.org/10.1242/dev.067587.

120 Murphy MM, Lawson JA, Mathew SJ, Hutcheson DA, Kardon G. Satellite cells, connective tissue fibroblasts and their interactions are crucial for muscle regeneration. *Development* 2011;138:3625–37. https://doi.org/10.1242/dev.064162.

121 Lepper C, Partridge TA, Fan C-M. An absolute requirement for Pax7-positive satellite cells in acute injury-induced skeletal muscle regeneration. *Development* 2011;138:3639–46. https://doi.org/10.1242/dev.067595.

122 Sacco A, Mourkioti F, Tran R, Choi J, Llewellyn M, Kraft P, *et al.* Short Telomeres and Stem Cell Exhaustion Model Duchenne Muscular Dystrophy in mdx/mTR Mice. *Cell* 2010;143:1059–71. https://doi.org/10.1016/j.cell.2010.11.039.

123 Blau HM, Webster C, Pavlath GK. Defective myoblasts identified in Duchenne muscular dystrophy. *Proc National Acad Sci* 1983;80:4856–60. https://doi.org/10.1073/pnas.80.15.4856.

124 Kuang S, Kuroda K, Grand FL, Rudnicki MA. Asymmetric Self-Renewal and Commitment of Satellite Stem Cells in Muscle. *Cell* 2007;129:999–1010. https://doi.org/10.1016/j.cell.2007.03.044.

125 Dumont NA, Wang YX, Maltzahn J von, Pasut A, Bentzinger CF, Brun CE, *et al.* Dystrophin expression in muscle stem cells regulates their polarity and asymmetric division. *Nat Med* 2015;21:1455–63. https://doi.org/10.1038/nm.3990.

126 Guttinger M, Tafi E, Battaglia M, Coletta M, Cossu G. Allogeneic mesoangioblasts give rise to alpha-sarcoglycan expressing fibers when transplanted into dystrophic mice. *Exp Cell Res* 2006;312:3872–9. https://doi.org/10.1016/j.yexcr.2006.08.012.

127 Sitzia C, Farini A, Jardim L, Razini P, Belicchi M, Cassinelli L, *et al.* Adaptive Immune Response Impairs the Efficacy of Autologous Transplantation of Engineered Stem Cells in Dystrophic Dogs. *Mol Ther* 2016;24:1949–64. https://doi.org/10.1038/mt.2016.163.

128 Darabi R, Gehlbach K, Bachoo RM, Kamath S, Osawa M, Kamm KE, *et al.* Functional skeletal muscle regeneration from differentiating embryonic stem cells. *Nat Med* 2008;14:134–43. https://doi.org/10.1038/nm1705.

129 Ausems CRM, Engelen BGM van, Bokhoven H van, Wansink DG. Systemic cell therapy for muscular dystrophies. *Stem Cell Rev Rep* 2021;17:878–99. https://doi.org/10.1007/s12015-020-10100-y.

130 Gerli MFM, Moyle LA, Benedetti S, Ferrari G, Ucuncu E, Ragazzi M, *et al.* Combined Notch and PDGF Signaling Enhances Migration and Expression of Stem Cell Markers while Inducing Perivascular Cell Features in Muscle Satellite Cells. *Stem Cell Rep* 2019;12:461–73. https://doi.org/10.1016/j.stemcr.2019.01.007.

131 Tedesco FS, Hoshiya H, D'Antona G, Gerli MFM, Messina G, Antonini S, *et al.* Stem Cell–Mediated Transfer of a Human Artificial Chromosome Ameliorates Muscular Dystrophy. *Sci Transl Med* 2011;3:96ra78-96ra78. https://doi.org/10.1126/scitranslmed.3002342.

132 Coley WD, Bogdanik L, Vila MC, Yu Q, Meulen JHVD, Rayavarapu S, *et al.* Effect of genetic background on the dystrophic phenotype in mdx mice. *Hum Mol Genet* 2016;25:130–45. https://doi.org/10.1093/hmg/ddv460.

133 Gerli MFM, Maffioletti SM, Millet Q, Tedesco FS. Transplantation of induced pluripotent stem cell-derived mesoangioblast-like myogenic progenitors in mouse models of muscle regeneration. *J Vis Exp Jove* 2014:e50532. https://doi.org/10.3791/50532.

134 Mathur S, Vohra RS, Germain SA, Forbes S, Bryant ND, Vandenborne K, *et al.* Changes in muscle T2 and tissue damage after downhill running in mdx Mice. *Muscle Nerve* 2011;43:878–86. https://doi.org/10.1002/mus.21986.

135 Brimah K, Ehrhardt J, Mouly V, Butler-Browne GS, Partridge TA, Morgan JE. Human Muscle Precursor Cell Regeneration in the Mouse Host Is Enhanced by Growth Factors. *Hum Gene Ther* 2004;15:1109–24. https://doi.org/10.1089/hum.2004.15.1109.

136 Ehrhardt J, Brimah K, Adkin C, Partridge T, Morgan J. Human muscle precursor cells give rise to functional satellite cells in vivo. *Neuromuscular Disord* 2007;17:631–8. https://doi.org/10.1016/j.nmd.2007.04.009.

137 Matthias N, Hunt SD, Wu J, Darabi R. Skeletal muscle perfusion and stem cell delivery in muscle disorders using intra-femoral artery canulation in mice. *Exp Cell Res* 2015;339:103–11. https://doi.org/10.1016/j.yexcr.2015.08.018.

138 Paoni NF, Peale F, Wang F, Errett-Baroncini C, Steinmetz H, Toy K, *et al.* Time course of skeletal muscle repair and gene expression following acute hind limb ischemia in mice. *Physiol Genomics* 2002;11:263–72. https://doi.org/10.1152/physiolgenomics.00110.2002.

139 Tu H, Zhang D, Qian J, Barksdale AN, Pipinos II, Patel KP, *et al.* A comparison of acute mouse hindlimb injuries between tourniquet- and femoral artery ligation-induced ischemia-reperfusion. *Inj* 2021;52:3217–26. https://doi.org/10.1016/j.injury.2021.09.002.

140 Padgett ME, McCord TJ, McClung JM, Kontos CD. Methods for Acute and Subacute Murine Hindlimb Ischemia. *J Vis Exp* 2016. https://doi.org/10.3791/54166.

141 Young CS, Hicks MR, Ermolova NV, Nakano H, Jan M, Younesi S, *et al.* A Single CRISPR-Cas9 Deletion Strategy that Targets the Majority of DMD Patients Restores Dystrophin Function in hiPSC-Derived Muscle Cells. *Cell Stem Cell* 2016;18:533–40. https://doi.org/10.1016/j.stem.2016.01.021.

142 Ley K, Laudanna C, Cybulsky MI, Nourshargh S. Getting to the site of inflammation: the leukocyte adhesion cascade updated. *Nat Rev Immunol* 2007;7:678–89. https://doi.org/10.1038/nri2156.

143 Verma M, Asakura Y, Wang X, Zhou K, Ünverdi M, Kann AP, *et al.* Endothelial cell signature in muscle stem cells validated by VEGFA-FLT1-AKT1 axis promoting survival of muscle stem cell. *Biorxiv* 2021:2021.08.28.458037. https://doi.org/10.1101/2021.08.28.458037.

144 Browaeys R, Saelens W, Saeys Y. NicheNet: modeling intercellular communication by linking ligands to target genes. *Nat Methods* 2020;17:159–62. https://doi.org/10.1038/s41592-019-0667-5.

145 Handt S, Jerome W, Tietze L, Hantgan R. Plasminogen activator inhibitor-1 secretion of endothelial cells increases fibrinolytic resistance of an in vitro fibrin clot: evidence for a key role of endothelial cells in thrombolytic resistance. *Blood* 1996;87:4204–13. https://doi.org/10.1182/blood.v87.10.4204.bloodjournal87104204.

146 Butler A, Hoffman P, Smibert P, Papalexi E, Satija R. Integrating single-cell transcriptomic data across different conditions, technologies, and species. *Nat Biotechnol* 2018;36:411–20. https://doi.org/10.1038/nbt.4096.

147 Korsunsky I, Millard N, Fan J, Slowikowski K, Zhang F, Wei K, *et al.* Fast, sensitive and accurate integration of single-cell data with Harmony. *Nat Methods* 2019;16:1289–96. https://doi.org/10.1038/s41592-019-0619-0.

148 Zhou Y, Zhou B, Pache L, Chang M, Khodabakhshi AH, Tanaseichuk O, *et al.* Metascape provides a biologist-oriented resource for the analysis of systems-level datasets. *Nat Commun* 2019;10:1523. https://doi.org/10.1038/s41467-019-09234-6.

149 Bondjers C, Kalén M, Hellström M, Scheidl SJ, Abramsson A, Renner O, *et al.* Transcription Profiling of Platelet-Derived Growth Factor-B-Deficient Mouse Embryos Identifies RGS5 as a Novel Marker for Pericytes and Vascular Smooth Muscle Cells. *Am J Pathology* 2003;162:721–9. https://doi.org/10.1016/s0002-9440(10)63868-0.

150 Bondjers C, He L, Takemoto M, Norlin J, Asker N, Hellström M, *et al.* Microarray analysis of blood microvessels from PDGF□B and PDGF□Rβ mutant mice identifies novel markers for brain pericytes. *Faseb J* 2006;20:1703–5. https://doi.org/10.1096/fj.05-4944fje.

151 Malecova B, Gatto S, Etxaniz U, Passafaro M, Cortez A, Nicoletti C, *et al.* Dynamics of cellular states of fibro-adipogenic progenitors during myogenesis and muscular dystrophy. *Nat Commun* 2018;9:3670. https://doi.org/10.1038/s41467-018-06068-6.

152 Fu X, Khalil H, Kanisicak O, Boyer JG, Vagnozzi RJ, Maliken BD, *et al.* Specialized fibroblast differentiated states underlie scar formation in the infarcted mouse heart. *J Clin Investigation* 2018;128:2127–43. https://doi.org/10.1172/jci98215.

153 Tidball JG, Welc SS, Wehling□Henricks M. Comprehensive Physiology. *Compr Physiol* 2018;8:1313–56. https://doi.org/10.1002/cphy.c170052.

154 Rigamonti E, Zordan P, Sciorati C, Rovere-Querini P, Brunelli S. Macrophage Plasticity in Skeletal Muscle Repair. *Biomed Res Int* 2014;2014:560629. https://doi.org/10.1155/2014/560629.

155 Wehling M, Spencer MJ, Tidball JG. A nitric oxide synthase transgene ameliorates muscular dystrophy in mdx mice. *J Cell Biology* 2001;155:123–32. https://doi.org/10.1083/jcb.200105110.

156 Villalta SA, Nguyen HX, Deng B, Gotoh T, Tidball JG. Shifts in macrophage phenotypes and macrophage competition for arginine metabolism affect the severity of muscle pathology in muscular dystrophy. *Hum Mol Genet* 2009;18:482–96. https://doi.org/10.1093/hmg/ddn376.

157 Juban G, Saclier M, Yacoub-Youssef H, Kernou A, Arnold L, Boisson C, *et al.* AMPK Activation Regulates LTBP4-Dependent TGF-β1 Secretion by Pro-inflammatory Macrophages and Controls Fibrosis in Duchenne Muscular Dystrophy. *Cell Reports* 2018;25:2163-2176.e6. https://doi.org/10.1016/j.celrep.2018.10.077.

158 Singh P, Chazaud B. Benefits and pathologies associated with the inflammatory response. *Exp Cell Res* 2021;409:112905. https://doi.org/10.1016/j.yexcr.2021.112905.

159 Shimizu-Motohashi Y, Asakura A. Angiogenesis as a novel therapeutic strategy for Duchenne muscular dystrophy through decreased ischemia and increased satellite cells. *Front Physiol* 2014;5:50. https://doi.org/10.3389/fphys.2014.00050.

160 Verma M, Shimizu-Motohashi Y, Asakura Y, Ennen JP, Bosco J, Zhou Z, *et al.* Inhibition of FLT1 ameliorates muscular dystrophy phenotype by increased vasculature in a mouse model of Duchenne muscular dystrophy. *Plos Genet* 2019;15:e1008468. https://doi.org/10.1371/journal.pgen.1008468.

161 Forsyth KD, Chua KY, Talbot V, Thomas WR. Expression of the leukocyte common antigen CD45 by endothelium. *J Immunol Baltim Md 1950* 1993;150:3471–7.

162 Bischoff J, Casanovas G, Wylie-Sears J, Kim D-H, Bartko PE, Guerrero JL, *et al.* CD45 Expression in Mitral Valve Endothelial Cells After Myocardial Infarction. *Circ Res* 2016;119:1215–25. https://doi.org/10.1161/circresaha.116.309598.

163 Paepe BD, Bleecker JLD. Cytokines and Chemokines as Regulators of Skeletal Muscle Inflammation: Presenting the Case of Duchenne Muscular Dystrophy. *Mediat Inflamm* 2013;2013:540370. https://doi.org/10.1155/2013/540370.

164 Kramerova I, Kumagai-Cresse C, Ermolova N, Mokhonova E, Marinov M, Capote J, *et al.* Spp1 (osteopontin) promotes TGFβ processing in fibroblasts of dystrophin deficient muscles through matrix metalloproteinases. *Hum Mol Genet* 2019;28:3431–42. https://doi.org/10.1093/hmg/ddz181.

165 Camps J, Breuls N, Sifrim A, Giarratana N, Corvelyn M, Danti L, *et al.* Interstitial Cell Remodeling Promotes Aberrant Adipogenesis in Dystrophic Muscles. *Cell Reports* 2020;31:107597. https://doi.org/10.1016/j.celrep.2020.107597.

166 Galli F, Mouly V, Butler-Browne G, Cossu G. Challenges in cell transplantation for muscular dystrophy. *Exp Cell Res* 2021;409:112908. https://doi.org/10.1016/j.yexcr.2021.112908.

167 Boisgerault F, Mingozzi F. The Skeletal Muscle Environment and Its Role in Immunity and Tolerance to AAV Vector-Mediated Gene Transfer. *Curr Gene Ther* 2015;15:381–94. https://doi.org/10.2174/1566523215666150630121750.

168 Motohashi N, Asakura A. Muscle satellite cell heterogeneity and self-renewal. *Frontiers Cell Dev Biology* 2014;2:1. https://doi.org/10.3389/fcell.2014.00001.

169 Tierney MT, Sacco A. Satellite Cell Heterogeneity in Skeletal Muscle Homeostasis. *Trends Cell Biol* 2016;26:434–44. https://doi.org/10.1016/j.tcb.2016.02.004.

170 Sillen M, Declerck PJ. Targeting PAI-1 in Cardiovascular Disease: Structural Insights Into PAI-1 Functionality and Inhibition. *Frontiers Cardiovasc Medicine* 2020;7:622473. https://doi.org/10.3389/fcvm.2020.622473.

171 Liu X, Situ A, Kang Y, Villabroza KR, Liao Y, Chang CH, *et al.* Irinotecan Delivery by Lipid-Coated Mesoporous Silica Nanoparticles Shows Improved Efficacy and Safety over Liposomes for Pancreatic Cancer. *Acs Nano* 2016;10:2702–15. https://doi.org/10.1021/acsnano.5b07781.

172 Meng H, Wang M, Liu H, Liu X, Situ A, Wu B, *et al.* Use of a Lipid-Coated Mesoporous Silica Nanoparticle Platform for Synergistic Gemcitabine and Paclitaxel Delivery to Human Pancreatic Cancer in Mice. *Acs Nano* 2015;9:3540–57. https://doi.org/10.1021/acsnano.5b00510.

173 Lee JE, Lee N, Kim T, Kim J, Hyeon T. Multifunctional mesoporous silica nanocomposite nanoparticles for theranostic applications. *Accounts Chem Res* 2011;44:893–902. https://doi.org/10.1021/ar2000259.

174 Argyo C, Weiss V, Bräuchle C, Bein T. Multifunctional Mesoporous Silica Nanoparticles as a Universal Platform for Drug Delivery. *Chem Mater* 2014;26:435–51. https://doi.org/10.1021/cm402592t.

175 Cauda V, Engelke H, Sauer A, Arcizet D, Bräuchle C, Rädler J, *et al.* Colchicine-Loaded Lipid Bilayer-Coated 50 nm Mesoporous Nanoparticles Efficiently Induce Microtubule Depolymerization upon Cell Uptake. *Nano Lett* 2010;10:2484–92. https://doi.org/10.1021/nl100991w.

176 Liu X, Lin P, Perrett I, Lin J, Liao Y-P, Chang CH, *et al.* Tumor-penetrating peptide enhances transcytosis of silicasome-based chemotherapy for pancreatic cancer. *J Clin Invest* 2017;127:2007–18. https://doi.org/10.1172/jci92284.

177 Liu X, Jiang J, Chan R, Ji Y, Lu J, Liao Y-P, *et al.* Improved Efficacy and Reduced Toxicity Using a Custom-Designed Irinotecan-Delivering Silicasome for Orthotopic Colon Cancer. *Acs Nano* 2019;13:38–53. https://doi.org/10.1021/acsnano.8b06164.

178 Shen D, Yang J, Li X, Zhou L, Zhang R, Li W, *et al.* Biphase Stratification Approach to Three-Dimensional Dendritic Biodegradable Mesoporous Silica Nanospheres. *Nano Lett* 2014;14:923–32. https://doi.org/10.1021/nl404316v.

179 Yu T, Hubbard D, Ray A, Ghandehari H. In vivo biodistribution and pharmacokinetics of silica nanoparticles as a function of geometry, porosity and surface characteristics. *J Control Release* 2012;163:46–54. https://doi.org/10.1016/j.jconrel.2012.05.046.

180 Fu C, Liu T, Li L, Liu H, Chen D, Tang F. The absorption, distribution, excretion and toxicity of mesoporous silica nanoparticles in mice following different exposure routes. *Biomaterials* 2013;34:2565–75. https://doi.org/10.1016/j.biomaterials.2012.12.043.

181 Yamamoto E, Kitahara M, Tsumura T, Kuroda K. Preparation of Size-Controlled Monodisperse Colloidal Mesoporous Silica Nanoparticles and Fabrication of Colloidal Crystals. *Chem Mater* 2014;26:2927–33. https://doi.org/10.1021/cm500619p.

182 Yamada H, Urata C, Aoyama Y, Osada S, Yamauchi Y, Kuroda K. Preparation of Colloidal Mesoporous Silica Nanoparticles with Different Diameters and Their Unique Degradation Behavior in Static Aqueous Systems. *Chem Mater* 2012;24:1462–71. https://doi.org/10.1021/cm3001688.

183 Allen TM. Long-circulating (sterically stabilized) liposomes for targeted drug delivery. *Trends Pharmacol Sci* 1994;15:215–20. https://doi.org/10.1016/0165-6147(94)90314-x.

184 Gabizon A, Goren D, Horowitz AT, Tzemach D, Lossos A, Siegal T. Long-circulating liposomes for drug delivery in cancer therapy: a review of biodistribution studies in tumor-bearing animals. *Adv Drug Deliver Rev* 1997;24:337–44. https://doi.org/10.1016/s0169-409x(96)00476-0.

185 González MN, Mello W de, Butler-Browne GS, Silva-Barbosa SD, Mouly V, Savino W, *et al.* HGF potentiates extracellular matrix-driven migration of human myoblasts: involvement of matrix metalloproteinases and MAPK/ERK pathway. *Skelet Muscle* 2017;7:20. https://doi.org/10.1186/s13395-017-0138-6.

186 Tatsumi R, Anderson JE, Nevoret CJ, Halevy O, Allen RE. HGF/SF Is Present in Normal Adult Skeletal Muscle and Is Capable of Activating Satellite Cells. *Dev Biol* 1998;194:114–28. https://doi.org/10.1006/dbio.1997.8803.

187 Rodgers JT, Schroeder MD, Ma C, Rando TA. HGFA Is an Injury-Regulated Systemic Factor that Induces the Transition of Stem Cells into GAlert. *Cell Reports* 2017;19:479–86. https://doi.org/10.1016/j.celrep.2017.03.066.

188 Choi S, Ferrari G, Tedesco FS. Cellular dynamics of myogenic cell migration: molecular mechanisms and implications for skeletal muscle cell therapies. *Embo Mol Med* 2020;12:e12357. https://doi.org/10.15252/emmm.202012357.

189 Bladt F, Riethmacher D, Isenmann S, Aguzzi A, Birchmeier C. Essential role for the c-met receptor in the migration of myogenic precursor cells into the limb bud. *Nature* 1995;376:768–71. https://doi.org/10.1038/376768a0.

190 Miller MA, Gadde S, Pfirschke C, Engblom C, Sprachman MM, Kohler RH, *et al.* Predicting therapeutic nanomedicine efficacy using a companion magnetic resonance imaging nanoparticle. *Sci Transl Med* 2015;7:314ra183. https://doi.org/10.1126/scitranslmed.aac6522.

191 Loreti M, Sacco A. The jam session between muscle stem cells and the extracellular matrix in the tissue microenvironment. *Npj Regen Medicine* 2022;7:16. https://doi.org/10.1038/s41536-022-00204-z.

192 Nguyen JH, Chung JD, Lynch GS, Ryall JG. The Microenvironment Is a Critical Regulator of Muscle Stem Cell Activation and Proliferation. *Frontiers Cell Dev Biology* 2019;7:254. https://doi.org/10.3389/fcell.2019.00254.

193 Podkalicka P, Mucha O, Dulak J, Loboda A. Targeting angiogenesis in Duchenne muscular dystrophy. *Cell Mol Life Sci* 2019;76:1507–28. https://doi.org/10.1007/s00018-019-03006-7.

194 Yao S, Chen Z, Yu Y, Zhang N, Jiang H, Zhang G, *et al.* Current Pharmacological Strategies for Duchenne Muscular Dystrophy. *Frontiers Cell Dev Biology* 2021;9:689533. https://doi.org/10.3389/fcell.2021.689533.

195 Zhou L, Lu H. Targeting Fibrosis in Duchenne Muscular Dystrophy. *J Neuropathology Exp Neurology* 2010;69:771–6. https://doi.org/10.1097/nen.0b013e3181e9a34b.

196 Birnbaum F, Eguchi A, Pardon G, Chang ACY, Blau HM. Tamoxifen treatment ameliorates contractile dysfunction of Duchenne muscular dystrophy stem cell-derived cardiomyocytes on bioengineered substrates. *Npj Regen Medicine* 2022;7:19. https://doi.org/10.1038/s41536-022-00214-x.

197 Ritso M, Tung LW, Rossi FMV. Emerging skeletal muscle stromal cell diversity: Functional divergence in fibro/adipogenic progenitor and mural cell populations. *Exp Cell Res* 2021;410:112947. https://doi.org/10.1016/j.yexcr.2021.112947.

198 Kusters YHAM, Barrett EJ. Muscle microvasculature's structural and functional specializations facilitate muscle metabolism. *Am J Physiol-Endoc M* 2016;310:E379–87. https://doi.org/10.1152/ajpendo.00443.2015.